Active and Passive Transport at Interfaces

Von der Universität Bayreuth
zur Erlangung des Grades eines
Doktors der Naturwissenschaften (Dr. rer. nat.)
genehmigte Abhandlung

von

Saeedeh Aliaskarisohi

geboren am 22 Mai 1977 in Teheran/Iran

1. Gutachter: Prof. Dr. Th .M. Fischer
2. Gutachter: Prof. Dr. M. Weiss

Tag der Einreichung: 05 .07. 2011
Tag des Kolloquiums: 16. 09. 2011

This thesis is dedicated to my mother, my father and Ali.

Acknowledgement

I wish to express my sincere gratitude to my supervisor Professor Thomas Fischer regarding his kindness, motivation and unsparing helps that was the best incentive for me during my PhD. Working under Professor Fischer's supervision was a precious opportunity in my life to experience a real scientific work. It was a pleasure for me to work with him and I enjoyed the discussions we had in an interactive environment. I have learned a lot from him and I will remain forever grateful to him.

Many thanks also go out to Professor Jürgen Köhler for leting me use his laboratory and Marek Blaszczynski from whom I have learnt about electroformation of vesicles .
Special thank - you for Dr. Natalia Wilke at the Universidad Nacional de Cordoba, Argentina. Collaborating and writing the paper on collapse with her in Bayreuth and Cordoba was a grate experience for me. This became possible with her nice attempt and invitation.
I would also like to acknowledge my collaborators: Dr. Ziad Khattari at Hashemite University, Jordan, Dr. Pietro. Tierno at Universitat de Barcelona, Spain, Dr. Prajnaparmita Dhar, University of California Santa Barbara, USA and Dr. Tom Johansen at University of Oslo, Norway.
This is the right place to thank those who made this thesis possible. I would like to thank Carmen Kerling and Klaus Oetter, my technical collegues, they are not only collegues but nice friends who kindly helped me many times with all kinds of situations. I politely thank Christine Linser, who had perfectly organized all of my official works and scientific trips.

Thanks to the group members: Thomas Bohlein, Nebojsa Casic, Uli Langer, Ayan Ray and Tobias Gehring and all of my friends who helped me by their kind answers to my technical and scientific questions.
One of those last grate thanks is for my husband Ali, he lovely accompanied me. Without his encouragement and enthusiasm this PhD would not have be done. Grate thanks to my father who always mentally and financially supported me.
Since there is no words and amount of thanks is enough to thank my mother, I just consider this PhD as a small compensation for her unsparing attempt she made for all the years of sacrifice, love and moral support.

And God,
thank you for being with me all the time and help me with your best blessings.

Contents

Acknowledgment 2

1 Chapter 1 **5**
Abstract 6
Kurzdarstellung 7

2 Chapter 2 **9**
2.1 Introduction 10
2.2 The Physics of Transport 10
2.3 Motivation of the Experiments 14
2.3.1 On the diffusion of circular domains on a spherical vesicle 14
2.3.2 Dynamics of self-assembly of flower-shaped magnetic colloidal clusters 17
2.3.3 Using symmetry breaking for directed transport of paramagnetic colloids on garnet films 18
2.3.4 Collapse and yield pressure of solid Langmuir monolayers 19

3 Chapter 3 **21**
On the diffusion of circular domains on a spherical vesicle 21

4 Chapter 4 **59**
Dynamics of self-assembly of flower-shaped magnetic colloidal clusters 59

5 Chapter 5 **68**
Using symmetry breaking for directed transport of paramagnetic colloids on garnet films 68

6 Chapter 6 **76**
Collapse and yield pressure of solid Langmuir monolayers 76

7 Chapter 7 **93**
Summary 93

8 Chapter 8 **96**
Bibliography 96

Chapter 1

Abstract

In this thesis we studied different forms of transport at interfaces. Four different interfacial transport mechanisms have been investigated. In each of them one physical aspect of active and passive transport is discussed. The four systems are arranged and discussed in four separate chapters. In chapter 3 and 4 we study the effect of static or hydrodynamic interactions on the cross over from individual diffusion towards collective diffusion. In chapter 3 the diffusion of circular domains on a giant unilamellar vesicle is measured. By tracking the motion of hydrodynamic interacting domains on a curved membrane we determined whether it is possible to extract rheological properties of the bilayer membrane. A similar two dimensional system interacting via static dipole interactions is studied in chapter 4. A mixture of paramagnetic and nonmagnetic colloidal particles immersed into a diluted ferrofluid is self assembled into colloidal flowers. In this experiment the effect of static interactions on the modes of diffusion of the petals of the colloidal flower is investigated in a one dimensional system. The results are compared with the single file diffusion of a hard core interacting one dimensional system. In chapter 5, the effect of actively directing particles with fluctuating active forces in a symmetry broken environment is studied. We address the question how to competing symmetry breaking effects decide on the direction of motion. The system consists of paramagnetic colloidal particles placed into an aqueous solution above the liquid-solid interface of a magnetic garnet film. An external modulated field supplies the fluctuations and the symmetry is broken by tilting the external field with respect to the magnetic film and/or by a magnetic symmetry broken pattern of the magnetic film. The direction of motion of the paramagnetic colloids is measured and we give a theoretical explanation of why which symmetry breaking wins. The fluidization of a two dimensional solid to a two dimensional liquid via the yielding of the monolayer is studied in chapter 6. The monolayer is locally yielded with thermo capillary interactions by focusing a laser onto it. We investigate the yielding as a function of the chemical nature of the monolayer and determine the thermodynamic requirements necessary for thermo capillary yielding.

Kurzdarstellung

In dieser Arbeit behandeln wir verschiedene Transportarten an Grenzflächen. Vier verschiedene Transportmechanismen an Grenzflächen wurden untersucht. Jeder Mechanismus behandelt einen physikalischen Aspekt aktiven oder passiven Transports. Die vier Systeme werden in vier einzelnen Kapiteln angeordnet und diskutiert.

In Kapitel 3 und 4 untersuchen wir den Effekt statischer und hydrodynamischer Wechselwirkungen auf den graduellen Übergang von individueller zu kollektiver Diffusion.
In Kapitel 3 wird die Diffusion von kreisförmigen Domänen auf einem riesigen unilamellaren Vesikel gemessen. Indem wir die Bewegung von hydrodynamisch interagierenden Domänen auf einer gekrümmten Membran verfolgen, bestimmen wir, ob es möglich ist, rheologische Eigenschaften der zweischichtigen Membran zu extrahieren. Ein ähnliches zweidimensionales System das über statische Dipolwechselwirkungen interagiert, wird in Kapitel 4 untersucht. Eine Mischung von paramagnetischen und nichtmagnetischen kolloidalen Teilchen in einem verdünnten Ferrofluid formt durch Selbstorganisation kolloidale Blumen. In unseren Experimenten wird der Effekt von statischen Interaktionen auf die Diffusionsmoden der Blütenblätter der kolloidalen Blumen in einem eindimensionalen System untersucht. Die Ergebnisse werden mit der *single file* Diffusion eines eindimensionalen Systems mit *hard core* Abstoßung verglichen.
In Kapitel 5 wird der Effekt von aktiv mit fluktuierenden Kräften getriebenen Partikeln in einer Umgebung gebrochener Symmetrie auf die Bewegung der Partikel erörtert. Wir untersuchen die Frage, inwiefern die konkurrierenden Symmetriebrechungseffekte über die Bewegungsrichtung der Partikel entscheiden. Unser System besteht aus paramagnetischen kolloidalen Partikeln in einer wässrigen Lösung über der flüssig-fest Grenzfläche eines magnetischen Granatfilmes. Ein externes modulierendes Feld liefert die fluktuierenden Kräfte und die Symmetrie wird gebrochen, indem das externe Feld gegenüber dem magnetischen Film gekippt wird und/oder indem das Magnetisierungsmuster des Granatfilmes symmetriebrechend wird. Die Bewegungsrichtung der paramagnetischen kolloidalen Partikel wird gemessen und eine theoretische Erklärung hergeleitet, warum welche Symmetriebrechung unter welchen Umständen gewinnt.

Die Fließgrenze eines zweidimensionalen Festkörpers zu einer zweidimensionalen Flüssigkeit durch Anlegen einer Dilatationsspannung an eine Monolage wird in Kapitel 6 untersucht. Die Monolage wird durch thermokapillare Wechselwirkungen lokal an die Fließgrenze gebracht, in dem ein Laser auf sie fokussiert wird. Wir untersuchen die Fließgrenze als Funktion der chemischen Struktur der Moleküle der Monolage und untersuchen die thermodynamischen Voraussetzungen, die für das thermokapillare Fließen notwendig sind.

Chapter 2

2.1 Introduction

This thesis is focused on different forms of transport at interfaces. Transport of soft condensed matter near interfaces plays an important role in biology, medical technology, enhanced oil recovery and the food industry. Transport to some extent is involved in most of the processes of life. Many biological events occur in aqueous environments near hard or soft surfaces. The transport properties of solvents such as their diffusion and viscosity will change in the vicinity of interfaces and naturally biologist [1-4] are interested in transport. For example the role of transmembrane proteins in transporting material or hormonal signals across the membrane interface is a field of intensive study. Transport at interfaces plays also a crucial role in food industry. For example the taste of chocolate depends on the surface rheological properties of the chocolate [5]. In enhanced oil recovery, adding a minute amount of surfactant to the water pressing out the oil from the well will change the interfacial properties of the oil-water interface and leads to significant higher yield of oil [6, 7]. Again an understanding of the flow near the water-oil interface is crucial for this process.

Although transport at interfaces are quiet important in different aspects of various fields, in this thesis we are interested to understand some fundamental physical questions arising near interfaces.

2.2 The Physics of Transport

Transport is a nonequilibrium phenomenon. In a material in equilibrium each element is mechanically and thermally in balance with its neighboring elements. Intensive variables or parameters do not depend on time and often have the same value at all positions, such that the gradients of these parameters vanish. There is no net exchange of matter or energy between an element of the system and its surroundings. Usually if certain intensive variables of the material are not uniform, the system is out of equilibrium. Suppose some external force disturbs the system and takes it out of equilibrium. For systems involving transport processes at least one of the state variables becomes a function of position. When the disturbance is removed, there is the tendency to bring back the material to equilibrium, and to reequilibrate the nonuniform distribution of the state variable in space. This process occurs by exchanging of mechanical or thermal properties between adjoining elements. If the state variable happens to be a conserved quantity the only way for equilibration is the transport of this quantity. The amount of this quantity

associated with one element decreases and the amount associated with the other element increases. According to the quantity conserved three major kinds of exchange processes are known: the exchange of matter, energy and momentum.

In the current thesis we will focus mainly on the interplay of the exchange of matter and momentum near interfaces. Interfaces are two-dimensional manifolds between two three dimensional phases. In practice an interface has a few molecular diameters in thickness; however, in all problems considered here they can be considered as truly two dimensional. Interfacial transport can occur across i.e. normal to the interface. Lateral transport is transport parallel to the interface. We will mainly deal with lateral transport but also show an example of the combination of lateral and normal transport. From an energetically point of view transport can be generally divided into active transport and passive transport.

Active transport is every kind of transport that requires the consumption of energy. The supply of energy can be in the form of a directed force or in the form of a fluctuating force. In the first case the direction of the motion is clearly in the direction of the external force and hence understanding the direction of motion is rather trivial.

In the presence of fluctuating forces the direction is less obvious. There are some systems called ratchets [8-11] in which the external field giving a clear direction of the particle competes with fluctuating forces applied to the particles in a symmetry broken environment. In such systems the preference direction of motion is a complex result of the competition of both types of forces. By studying active transport of such systems one may seek directed motion and the proper conditions that are required to give the transported particles one or the other direction of motion. Instead of deterministic and fluctuating forces we might also have only fluctuating forces and a competition between different forms of broken symmetry of the environment trying to direct the motion along different pathways. In this thesis we will study the interplay of two ways to break the symmetry to figure out in which circumstances in an active fluctuating system one can have directed transport.

Passive transport - in contrast to active transport- , does not require energy. For this reason passive transport can occur both in equilibrium and out of equilibrium. In equilibrium passive transport differs from active transport under the influence of fluctuating forces by the requirement that the random forces must always drive the system toward equilibrium. The mathematical consequence of this constraint is expressed by the fluctuation dissipation theorem that connects the correlations of the fluctuating forces with the equilibrium mobility of the transported particle.

The fluctuation dissipation theorem hence connects the fluctuating motion of particles with the viscosity of the fluid and this allows the measurement of rheological properties.

If the particles in the fluid interact with each other either via static potentials or via hydrodynamic interactions, we need to distinguish *collective diffusion* and *individual* or *self diffusion*. In an ensemble of particles a net motion occurs when there are gradients of the chemical potential or the concentration. This motion is called *collective diffusion*. Passive collective diffusion in contrast to active transport spreads the particles in a random way from regions of higher concentration to regions of lower concentration. If there is no interaction of the particles then collective diffusion occurs only due to the *individual self diffusion* of the constituents and therefore both diffusion coefficients coincide. They are no longer the same when the particles interact.

Individual or self diffusion is the random motion of an individual particle. The fluctuation dissipation theorem does not hold only for particles of the fluid but also for tracer particles performing self diffusion inside the liquid. Since it is much easier to observe larger Brownian particles immersed into the fluid mesoscopic objects are ideal tracer particles to study the rheological properties of the surrounding fluid. Self diffusion in contrast to collective diffusion cannot be described by gradients of the chemical potential or concentration. They occur due to random and deterministic forces acting on the diffusing particle. As a result the particle achieves a fluctuating velocity. The auto correlation function of the velocity decays as a function of time due to the random forces and therefore the area under the correlation function can be used to define the self diffusion coefficient. This definition of the diffusion coefficient is very general and works even when deterministic forces are present and the usual definition of diffusion coefficients via the diffusion equation can no longer be used. Since the diffusion is mostly due to thermal fluctuations then using the fluctuation dissipation theorem which gives a relation between the diffusion coefficient and the friction coefficient allows extracting the rheological properties of the system.

The possibility of having collective diffusion differing from self diffusion is interesting because it allows separating random and deterministic effects. In the presence of random forces, particles can only have random motion. To have collective motion of particles differing from the self diffusion the particles must interact and this will happen only in the presence of deterministic forces. Random forces on the particles lead to no correlations in the motion of different particles. Interactions, however, correlate the motion of different particles and hence deter-

ministic forces between the particles can be read off the cross correlations of the velocities of different particles. Using Kubo's formula shows that in such systems cross-correlations between two particles are not zero. This means that there is some deterministic interaction between the particles that cause the motion of one particle to depend on the motion of the other. This behavior makes it possible to decompose the correlated motion of particles into uncorrelated normal modes of diffusion. Often such normal modes occur in the form of waves characterized by a wave number q. Low wave vectors correspond to the highest diffusion constant where the particles diffuse together without interaction like a rigid motion. For higher wave vectors the relative motion of particles causes the interactions to push the particles back to their original position and therefore the higher the wave vectors the smaller the diffusion constant. Interactions between particles can be divided into two groups; *hard core* and *soft core* interactions. In hard core interactions two particles only interact when they touch each other. The diffusion of particles in narrow channels, where the particles cannot pass each other and only sterically interact via hard core interactions is known as *single-file diffusion* (SFD) [12-18]. Since the particles need time to encounter each other, hard core interactions have a time delay defined by the time needed to diffuse the average separation between the particles. In soft core interactions, particles interact via long range forces and they will interact instantaneously over large distances. For this reason different modes of diffusion can tell a lot about the interactions at work between the particles. We will use such decoupling of modes to unravel hydrodynamic as well as other soft interactions in diffusing systems.

We have already mentioned that diffusion also allows the determination of rheological properties of liquids. Rheology studies the deformation and flow of material under mechanical stress. Interfacial rheology is the measurement of the elasticity and viscosity of two dimensional systems formed at interfaces. Newtonian liquids such as water are purely viscous and a Hookian solids are purely elastic materials. Most interfacial systems have both elastic and viscous properties and are called viscoelastic. There are two different interfacial viscosities, dilatational and interfacial (shear) viscosities. Each of them is the response of the system to a certain kind of stress. If a shear stress is applied a unit element of the material is distorted. Only the shape and not the size of the element changes. In contrary when a pressure acts on an element, then a dilatational stress increases or decreases the area of an element while shape remains the same. Since most of the bulk materials can be treated as incompressible in creeping flow problems this form of deformation does not appear in three dimensional liquids. We will use the diffusion described above to unravel rheological properties of two dimen-

sional fluids via the fluctuation dissipation theorem. As should be clear from the discussion of the modes of diffusion in interacting systems these modes of diffusion also play an essential role when there are hydrodynamic couplings between several particles that result from the viscous properties that we are interested in.

One fundamental requirement for transport is that the system behaves like a fluid and flows. If the system is initially solid, and one mechanically wants to enforce the transport, one needs to pass the yield-stress to turn the solid into a liquid. Only then transport occurs. It is hence an interesting question to study the threshold from a solid to a liquid in a non-equilibrium situation.

All situations which described briefly above are general physical questions that can be studied in different experiments and in each experiment may have their specific and general answers. In this thesis four different experiments have been performed that address the questions discussed in section 2.1. In all of them the main goal is studying the transport at interfaces. Each of them uses different phases, separated by specific interfaces, and attacks one of the general questions raised in section 2.1. In what follows we restate each general question within the framework of the specifics of each experiment to motivate why the experiment was performed.

2.3 Motivation of the Experiments

2.3.1 On the diffusion of circular domains on a spherical vesicle

As an example of single particle diffusion, we studied the diffusion of circular domains on a spherical giant unilamellar vesicle [chapter3]. A giant unilammellar vesicle is a bilayer membrane of lipids in water that is closed to a micron sized spherical shell surrounding an aqueous interior and residing in an aqueous solution. The giant unilamellar vesicle of our experiment is made from a mixture of dioleoylphosphatidylcholine (DOPC), dipalmytoylphosphatidylcholin (DPPC), and cholesterol (Chol). For a specific range of over all composition of the mixture phases of different composition coexist. In the vesicle the phase separation occurs in the form of DPPC rich and DPPC poor domains. These domains are visualized using fluorescence microscopy and appear as dark or bright small circles which

are diffusing on the vesicle. In our experiment these domains take over the role of a tracer particle probing the rheological properties of the surroundings. The motion of these domains is due to thermal fluctuations and they randomly diffuse like Brownian particles. Cicuta et al. [19] have studied the motion of exactly this system before us and they came to the conclusion that the vesicle interface has a large interfacial shear viscosity. However, they neglected any effect of dynamic interactions of the domains and of the confinement of the domains to a finite size curved vesicle. The motivation of our study was to reexamine the problem of diffusing hydrodynamic interacting domains on a curved confined geometry. The problem is more complex than the motion of a single domain in a flat membrane solved for the first time by Saffman and Delbrück [20]. A change in position of one domain on a vesicle can be due to translational diffusion of the domain through the vesicle membrane but will be hindered by the confinement of the vesicle an hydrodynamic interactions with other domains. The interactions correlate the motion of different domains. Under these circumstances, each domain has two degrees of freedom to move in the membrane giving rise to double the number of normal modes of diffusion than the number of domains. These normal modes must be understood to extract information on the rheological properties of the vesicle. Moreover, the vesicle can rotate like a solid within the surrounding fluid and such motion does not probe the membrane viscosity but the viscosity of the embedding bulk water. Hence there will be situations when the motion of the domain is due to interfacial or due to bulk dissipation. We took two approaches to this problem: one-domain rheology and two domain rheology.
In one-domain rheology we measure the diffusion of a single domain. This motion is a superposition of two different kinds of motion. One is the motion of domain in the membrane when the domain moves relative to the quiescent membrane and thereby shears the membrane. This motion is obviously sensitive to the surface shear viscosity. The second motion is a motion where the domain diffuses with the rest of vesicle like a solid rotational diffusion. This shears the water but not the membrane. The latter motion is obviously insensitive to the surface shear viscosity. It is easy to microscopically resolve the motion of one-domain but the solid rotation of the vesicle must be disentangled theoretically from the translational motion within the membrane.

One might try to eliminate the solid rotation experimentally by measuring the relative motion of two domains. We call this type of experiment two-domain rheology. One of the questions in this experiment was hence whether one- or two domain rheology is a more efficient technique to extract information about the viscous properties of the membrane. It is clear that due to the hydrodynamic cor-

relations between the domains the general theory of Kubo must be used here and diffusion constants need to be defined via the correlation functions of velocity fluctuations. As mentioned in section (2-1) in using Kubo's formalism we must not worry about the existence of deterministic forces a priori, but are able to extract the interactions a posteriori by the decomposition of the motion of several - in our case two - domains. We hoped that this approach would tell us whether the work of Cicuta et al.[19] is right or wrong. Once having measured the normal mode diffusion constants, using the fluctuation-dissipation theorem together with the solution of the hydrodynamic model problem (two domains of equal size and similar surface shear viscosity as the coexisting membrane phase) gives us the freedom to connect those diffusion constants to the theoretical friction coefficient and fit the rheological properties of the membrane.

The theoretical model uses the equations of creeping flow. Measuring the size of the domains as a function of time showed that dilatational stress is absent in our system and the only force which affects these domains arises from shear stress. To derive theoretically the diffusion constant for a single domain, the bulk liquid inside and outside the vesicle should fulfill the Stokes equation. The interface fulfills a similar two dimensional Stokes equation. There are two constitutive equations for the dynamic bulk and the surface stress tensor. The coupling of the bulk liquids to the membrane arises due to the traction on the membrane that is the bulk stress tensor times the normal vector to the interface. After solving these equations theoretically the dimensionless friction coefficient f is obtained. This coefficient is the response in viscous torque τ of the domain to a movement with angular frequency ω.

$$f \propto \frac{\tau}{\omega} \tag{2.1}$$

Details of theoretical calculation are available in chapter 3. The fluctuation -dissipation theorem connects the dimensionless friction coefficient to the experimentally accessible rotational diffusion constant, D_{rot} :

$$f^{-1} \propto \frac{D_{rot}}{k_B T} \tag{2.2}$$

where T is the absolute temperature and k_B is Boltzmann's constant.

Since the dimensionless friction coefficient is a function of the surface shear viscosity, using equations (2.1) and (2.2) enables the determination of the surface shear viscosity.

Whether our experiments confirmed or disproved the results of Cicuta et. al. [19] and what are the effects of confinement, hydrodynamic interactions and rotation of the entire vesicle are discussed in detail in chapter 3. The main results

obtained from those experiments are once more summarized in chapter 7.

2.3.2 Dynamics of self-assembly of flower-shaped magnetic colloidal clusters

In the previous experiment no static interactions between the domains were present. All interactions were hydrodynamic interactions. In the second experiment we were interested in the effect of static interactions on the modes of diffusion in a one dimensional system. The second experiment is devoted to the situation where a cross over from single particle diffusion to collective diffusion is triggered by static soft interactions. The system of chapter 4 is a mixture of paramagnetic and nonmagnetic colloidal particles immersed into a diluted ferrofluid. In the ferrofluid nonmagnetic particles effectively behave like a diamagnet (magnetic holes), while the paramagnetic particles are still effectively behaving like a paramagnet. The investigation of the effect of static interactions onto the particle transport is easier in magnetic system than in electrostatic systems because the magnetostatic interactions are long range. The long range of the interactions enables the observation of the particle's diffusion with a microscope.

In a static magnetic field the effective dipoles (the magnetic dipole minus the dipole of the ferrofluid background) of the two sorts of particles point into opposite directions. In a mixture of effective para and diamagnets, we are able to assemble a few diamagnets into a one-dimensional circle surrounding the equator of a large paramagnetic particle. The motion of diamagnets on this one-dimensional ring is a result of Brownian motion of the particles and dipole repulsion between the particles. Hence it is an ideal system to investigate the cross-over from an individual toward a collective diffusion caused by the soft repulsion of the diamagnets in the ring. One motivation is also to compare the diffusion with other one-dimensional single file diffusing systems [12-18]. that are interacting via short range hard core repulsions.

In single file diffusion [12-18] each single interaction is retarded. The retardation time is defined by the time to freely - without interaction - diffuse toward the next particle. The long range character of the magnetic dipole interactions in our system lacks this retardation and thus affects the motion of neighboring diamagnets instantaneously and over large distances. Although Kubo's formalism has not been used for single file diffusion, we feel that it is the appropriate way to extract information about either system. In our experiment we use the Kubo formalism to measure the autocorrelation and cross-correlation of nonmagnetic petals in the one

dimensional ring. The difference in diffusion constants of different normal modes again enables us to disentangle the random forces from the deterministic dipolar forces. Moreover we thought that the difference to a single file diffusion system should somehow show up in the time dependence of the correlation functions.

Besides the diffusion of the diamagnetic holes in the ring the attraction of the diamagnets into the ring is also comparable to thermal random forces. As a result the number of diamagnets in the ring changes as a function of time. The dynamics of absorption and desorption is a second interesting problem that we discuss in the same chapter.

The differences of our soft interacting diamagnetic holes as compared with single file diffusion systems is discussed in detail in chapter 4. There also the fluctuations of the number of diamagnets in the ring are reported and analyzed. In chapter 7 the main results are restated together with the results from other chapters.

2.3.3 Using symmetry breaking for directed transport of paramagnetic colloids on garnet films

Both experiments discussed so far were dealing with passive transport. The third experiment in chapter 5 tries to understand the direction of transport in a system involving active transport. The system is driven by the simplest form of a fluctuating force, namely a sinusoidal modulated force. The average force in such a system vanishes and if there is no symmetry breaking then there is no preferred direction of transport. A preferred direction arises when the symmetry is broken. In our experiment two ways to break the symmetry compete with each other in directing the particles. We are interested into understanding which direction is finally chosen and why.

Our experimental paramagnetic colloidal particles are placed into an aqueous solution above the liquid-solid interface of a magnetic garnet film. The particles are driven by an oscillating external magnetic field superposed to the heterogeneous magnetic field of the ferromagnetic domain structure of the garnet film. The symmetry in this system can be broken either by the local domain structure of the garnet film or by tilting the external magnetic field with respect to the film.

The simplest non symmetry broken domain structure in the magnetic garnet film are straight stripe domains of alternating magnetization normal to the film. An oscillating external field normal to the film results in periodic forces varying in space and time that will randomly push around the particles. No net direction of

transport in an external field normal to a straight stripe pattern occurs. One way to break the symmetry and transport the paramagnetic particles into a given direction is to tilt the external field. The second possibility is to look for regions on garnet film where the stripes are not straight but exhibit a wedge pattern. We studied the competition of directing particles with these two ways to break the symmetry.

In chapter 5 the hopping mechanism is described in details and the effect of a mixture of two symmetry breaking parameters on the directed transport of particles is studied experimentally and theoretically. We derive the exact form of the magnetic field produced above the specific wedge magnetic patterns that enables us to compute the driving forces as a function of time and space both for a normal and tilted external field. This enables us to compute a phase diagram of the hopping direction as a function of the wedge angle and the tilt of the field. A detailed analysis and a comparison of experiment and theory will be given in chapter 5. How symmetry breaking can direct particles in an actively driven system is explained in this chapter and main conclusions are summarized in chapter 7.

2.3.4 Collapse and yield pressure of solid Langmuir monolayers

As shown in the previous experiment active transport can be directed in subtle ways. However, one condition to achieve transport in active systems is that the particles have a finite mobility. Such is the case in liquid systems not in solids. Viscoelastic systems can be forced from a solid to a liquid by external stress. In our final experiment we studied the mechanical enforcement of transport in a two dimensional viscoelastic Langmuir monolayer at an air-liquid interface. A transition from solid to liquid is enforced in the monolayer by thermocapillary dilatational stress using a laser focused on the monolayer.

A Langmuir monolayer is a monolayer of insoluble surfactants at the air-water interface. Depending on the lateral density and temperature, liquid and solid phases of the monolayer can be prepared. Our experiments are performed in a solid phase at very high interfacial density. Further compression of the monolayer beyond the closed packed density results in the monolayer leaving the two dimensional interface and collapsing into the third dimension. The transition from 2d to 3d is called monolayer collapse [21]. When the monolayer is in the solid phase a continuous motion arising during the collapse requires the monolayer to transiently flow and hence convert into a liquid. Our interest in this experiment was to

learn how much and what kind of stress is required to convert a solid monolayer to a liquid monolayer. Hence there must be a threshold for the conversion from solid to liquid prior to collapse. We are interested in this mechanical induced solid to liquid transition. The critical pressure needed for this conversion is called yield pressure. The yield pressure can be reached either by compressing the monolayer in a Langmuir film balance or by local heating the monolayer with a laser. Chapter 6 is an example of a yielding solid system. An inward flow toward the focus of the laser is observed when the yield pressure is reached. We tried to understand which other thermodynamic conditions must be met in a specific material to yield in a laser. In chapter 6 we looked at the yielding of monolayers in a laser focus for a variety of different surfactant molecules. The yielding behavior was correlated with other thermodynamic properties of the same material to find a connection between them. Our main concern is not the collapse of the monolayer but the yielding. What is necessary for the laser induced yielding to occur is discussed in chapter 6 and summarized in chapter 7.

We have motivated the reasons, why we wanted to perform the experiments of this thesis. The results and details of the four experiments have been published in, or submitted to the literature. The published manuscripts with the results are attached to the next chapters. The answers we got to our questions are discussed therein in detail and a summary of those answers are repeated in a summary (chapter 7).

Chapter 3

On the diffusion of circular domains on a spherical vesicle

S. Aliaskarisohi, P. Tierno, P. Dhar, Z. Khattari, M. Blaszczynski, and TH. M. Fischer,

J. Fluid Mech. **654**, 417 (2010)

Copyright Cambridge University Press 2010

DOI: 10.1017/S0022112010000650

J. Fluid Mech. (2010), *vol.* 654, *pp.* 417–451. © Cambridge University Press 2010
doi:10.1017/S0022112010000650

On the diffusion of circular domains on a spherical vesicle

S. ALIASKARISOHI[1], P. TIERNO[2], P. DHAR[3], Z. KHATTARI[4], M. BLASZCZYNSKI[1] AND TH. M. FISCHER[1]†

[1]Institut für Experimentalphysik, Universität Bayreuth, 95440 Bayreuth, Germany

[2]Departament de Química Física, Universitat de Barcelona, Marti i Franqes 1, 08028 Barcelona, Spain

[3]Department of Chemical Engineering, University of California Santa Barbara, Santa Barbara, CA 93106, USA

[4]Department of Physics, Hashemite University, 13115 Zarqa, Jordan

(Received 17 August 2009; revised 2 February 2010; accepted 2 February 2010; first published online 11 May 2010)

Tracking the motion of lipid domains on a vesicle is a rheological technique allowing the measurement of surface shear viscosities of vesicular lipid phases. The ratio of surface to bulk viscosity defines a viscous length scale. Hydrodynamic interactions split the motion of the domains into different modes of diffusion. The measurability of surface shear viscosities from any mode of diffusion is limited to viscous length scales between the radius of the domains and the radius of the vesicle. The measurability of the surface shear viscosity results from the sensitivity of the diffusion to surface shear viscosities and from sufficient spatial resolution to resolve the diffusive motion. Switching between the various modes of diffusion is a trade between sensitivity gained and resolution lost by the hydrodynamic interactions leaving the measurability unchanged. Measurability drops with the number of domains making single-domain rheology the best technique to measure surface shear viscosities. Ultimately confinement of the domains to small vesicles renders measurements of surface rheological properties with domain-tracking rheology impossible. Experiments on domains in vesicles of a mixture of dioleoylphosphatidylcholine (DOPC), dipalmytoylphosphatidylcholin (DPPC) and cholesterol (Chol) exhibit diffusion that is entirely controlled by dissipation into the water. The diffusion is suppressed compared to the diffusion of isolated domains in a flat membrane due to confinement to the curved vesicle and by hydrodynamic interactions between the domains. Effects of surface shear viscosity can be neglected.

1. Introduction

Diffusion is one of the basic passive means of irreversible transport used in the cell as well as in membranes. In comparison to active forms of transport, diffusion does not cost any energy. Without interaction between components, diffusion will ultimately lead to thermal equilibrium with a complete mixture of the components. Along those lines (Singer & Nicholson 1972) originally modelled biological membranes as an ideal two-dimensional mixture of lipids and proteins that was initially described by the fluid mosaic model. Later it has been realized that despite the tendency to mix, lipids

† Email address for correspondence: thomas.fischer@uni-bayreuth.de

interact. The interaction causes demixing into membrane domains ('rafts') (Simons & Ikonen 1997; Brown & London 1998; Mukherjee & Maxfield 2000; Gaus *et al.* 2003; Engelman 2005) consisting of a phase rich in cholesterol, certain types of lipids and proteins, and a complementary phase containing the complementary composition of the lipids. The mesoscopic structure which in part is caused by the enthalpy of mixing of the components has triggered research towards understanding the interactions of two-dimensional model mixtures. Experiments on monolayer mixtures Radhakrishnan & McConnell (1999) and later on giant unilamellar vesicles (Korlach *et al.* 1999; Bagatolli & Gratton 2000; Veatch & Keller 2002) has shown that especially the mixtures of phospholipids and cholesterol can be understood as thermodynamic equilibrium mixtures. Miscibility diagrams determined from the experiments could be described with theories minimizing the Gibb's free energy of the reactive mixture. The long term stability of domains of different composition allows treating such domains as entities with their own transport properties. Cicuta, Keller & Veatch (2007) showed that such domains undergo diffusive motion. The dynamics of the domains are governed by the viscous properties of the participating two- and three-dimensional phases (Saffmann & Delbrück 1975; Hughes, Pailthorpe & White 1981) as well as by their geometrical arrangement (Dimova *et al.* 1999*a*; Dimova, Dietrich & Pouligny 1999*b*; Danov, Dimova & Pouligny 2000; Fischer, Dhar & Heinig 2006). The work of Saffmann & Delbrück (1975) originally derived for small solid and disk shaped inclusions of proteins into a flat and highly viscous membrane has been subject of both experimental tests (Peters & Cherry 1982; Klingler & McConnell 1993; Daniels & Turner 2002; Naji, Levine& Pincus 2007; Sickert, Rondelez & Stone 2007) and theoretical generalizations (Prasad, Koehler & Weeks 2006; Petrov & Schwille 2008). The knowledge of rheological properties of complex membranes or monolayers is an important experimental issue and one would like to understand how the addition of cholesterol (Veatch & Keller 2003; Beattie *et al.* 2005; Veatch, Gawrisch & Keller 2006), synthetic fluorinated compounds (Riess 2002) and the presence of electrostatic interactions (Heinig *et al.* 2002; Khattari *et al.* 2002; Fischer & Lösche 2004) alter the membrane or monolayer viscous behaviour. The purpose of this work is to generalize the theory of Saffmann & Delbrück (1975) for circular domains diffusing on a vesicle. One of the important findings of Saffmann & Delbrück (1975) was that the ratio of the membrane to the bulk viscosity defines a viscous length scale. Therefore, the motion of objects moving in a membrane depends on how the size of these objects compares to the viscous length scale. Diffusion of domains on a vesicle differs from the calculations of Saffmann & Delbrück (1975) in four important aspects. Firstly, the surface viscosity of the membrane embedding the domain in general can be either low or high. A theory taking into account the full range of possible surface shear viscosities of the embedding membrane has been first derived by Hughes *et al.* (1981). Secondly, since the domains on the vesicle, like the embedding membrane, are in general liquid not solid, the domain surface shear viscosity plays an important role. De Koker (1996) was the first to derive a hydrodynamic equation for a liquid domain diffusing in a flat membrane of the same surface shear viscosity. Thirdly, the vesicle consists of a curved membrane and therefore has a finite size. As a consequence of its finite size, the vesicle will perform rotational diffusion while the domain is diffusing on its surface. The apparent motion of a domain observed on the vesicle surface with microscopic techniques is hence a superposition of both kinds of diffusive motions. When being interested in extracting rheological properties of the vesicle membrane from the domain diffusion the rotational diffusion of the vesicle in the water is disturbing. One might eliminate solid rotations of the vesicle

by tracking the relative motion between several domains on the same vesicle, which is independent of the rotation of the vesicle as a whole. However, such two-domain rheology introduces the separation of the domains as a new length scale to the problem, and our mathematical results presented in this manuscript results show cross-over from uncorrelated to strongly correlated relative motion when this new length scale becomes smaller than the viscous length scale. As a fourth complication, the hydrodynamic correlations between the domains are different for different modes of motion. Here we derive the hydrodynamic equations that govern such diffusion for a single-liquid bilayer domain diffusing on a vesicle and for the combined and the relative diffusion of two liquid bilayer domains. For the single-domain diffusion we will show that there is a cross-over from surface viscous dominated diffusion to a solid rotational diffusion of the entire vesicle when the size of the vesicle is smaller than viscous length scale. For the two-domain rheology the same cross-over manifests itself by a change from uncorrelated diffusion of the two domains towards a correlated diffusion. This behaviour also occurs for two domains in a flat membrane and the theory of two particle microrheology (Prasad *et al.* 2006) differs from single-domain rheology for the case of a flat membrane. Our results provide a theoretical tool to analyse recent (Cicuta *et al.* 2007) measurements of surface shear viscosity of domains diffusing on curved membranes. We additionally apply the theory to new measurements of the same system. The paper is organized as follows. In § 2 we describe some general aspects of measuring diffusion on curved vesicles. In § 3 we describe how to perform a single-domain rheology experiment. Section 4 describes the decomposition of the motion of two domains into four normal modes of motion and the experimental extraction of the dimensionless diffusion coefficient. Section 5 outlines the theory for the computation of the dimensionless diffusion coefficient as a function of the geometrical details and as a function of the various rheological properties of the participating fluids. Sections 6 and 7 present experimental and numerical results for the single-domain and two-domain diffusion coefficients, respectively. We compared both techniques and comment on their limitations. Section 8 discusses our model in the context of our and others experimental findings and § 9 gives a summary.

2. Experimental

We consider a set of $i = 1 \ldots n$ diffusing domains as liquid circular segments of radii a_i on a spherical vesicle of radius R (figure 1). A fluorescence microscope image of such a vesicle is depicted in figure 1. It shows a vesicle of radius $R = 12\,\mu\text{m}$ of a mixture of dioleoylphosphatidylcholine (DOPC), dipalmytoylphosphatidylcholin (DPPC) and cholesterol (Chol) of composition (DOPC/DPPC/Chol = 16/64/20) at a temperature of $T = 23^{\circ}\text{C}$. The mixture decomposes into an L_α phase visible as bright domains of average size $a = 1$–$3\,\mu\text{m}$ and into a L_0 and a S_0 phase (Veatch & Keller 2003) that both appear dark and are not distinguishable in the fluorescence image. DOPC, DPPC and Cholestrol were purchased from Avanti Polar Lipids. Mixtures were fluorescently labelled with 1 %–3 % of 1,2-dihexadecanoyl-sn-glycero-3-phosphoethanolamine, triethylammonium salt (Texas Red DHPE) which was purchased from Molecular Probes (Eugene, Oregon USA). Giant unilamellar vesicles were prepared using the electroformation method as described by Angelova *et al.* (1992) and Veatch & Keller (2002). Lipids were dissolved in chloroform/methanol 9:1 at a concentration of 2 mg ml^{-1}. A drop of 10 µl was deposited onto the conductive side of an indium tin oxide (ITO) coated glass slide and dried using a nitrogen stream.

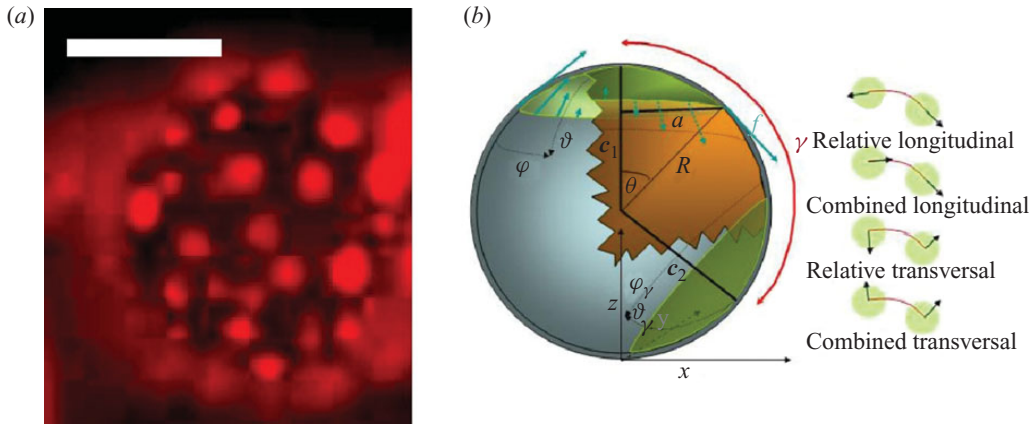

FIGURE 1. (*a*) Fluorescence microscopy image of a vesicle of radius $R = 12\,\mu\text{m}$, consisting of a mixture of DOPC/DPPC/Chol of composition 16/64/20 that decomposes into an L_α phase (bright domains), and into a L_0 and a S_0 phase that cannot be distinguished (continuous dark region). The scale bar corresponds to a distance of 10 μm. The scope of this paper is to describe the origin of diffusion of the domains in the vesicle. (*b*) Scheme of two lipid domains (green) of radius a centred at position $\boldsymbol{c}_1$ and $\boldsymbol{c}_2$ and diffusing on a vesicle of radius R. The domains have a conical domain angle of θ and γ is the separation angle. The force profile normal to the edges (cyan arrows) of the domains arising from thermal fluctuations or external forcing causes the domains diffusion. Shown are also the coordinates (ϑ, φ) defined with respect to the z-axis and the second coordinate system $(\vartheta_\gamma, \varphi_\gamma)$ defined with respect to the $\boldsymbol{c}_2$-axis. The four possible modes of diffusion of the domains are depicted on the right. The red line is the interconnecting geodesic between the domains and the black arrows indicate the velocities of the domains. Longitudinal modes correspond to motion in direction of the geodesic. Transversal modes correspond to motion perpendicular to the geodesic. Combined motion is into the same direction while relative motion is into antiparallel directions. The terms 'parallel' and 'direction' are used in the sense of the curved metric on the surface of the vesicle not in the sense of three-dimensional Euclidian metric.

The sample was then put in vacuum for 1–3 h at 60°C. A silicone spacer was deposited around the dried lipids and 0.2 M sucrose solution in pure water (Millipore milli-Q water) was added. By sealing the slide with another ITO Plate a capacitor was formed and an AC field was applied for 2 h and 10 min at 60 ± 3°C. For applying the AC field two different schemes were used and both of them gave us nice vesicles. In the first scheme, the voltage was increased from 0.2 to 2 V in 10 min and the swelling time under the AC field was 100 min. Finally, the voltage is decreased from 2 to 0.2 V at a frequency of 1 Hz within 20 min to lay down the vesicles. In the second scheme, the voltage was increased from 0.2 to 2 V at 10 Hz within 10 min then the frequency was decreased to 1 Hz and kept there for 100 min. The lay down frequency was 0.5 Hz instead of 1 Hz. The grown vesicles were stored at room temperature (24°C) in the dark until use. The best time for observation was between 1 and 12 h after electroformation. Vesicles were sucked out from the chambers and put on the microscope glass slide, 20 μl glucose solution was added. A coverslip (0.17 mm) was used with tape spacers (0.1 mm) to observe the samples and a fluorescence microscope (LEICA DM 4000B) with a $\times 63$ air objective was used for visualization. The working distance of the objective was 0.31 mm which allowed to observe vesicles floating at a distance of 140 μm from the cover slide. In order to avoid hydrodynamic interactions with the upper cover slide and the lower glass slide we always worked with vesicles spaced at least 2 diameters from both slides. The vesicles were investigated at room temperature 23 ± 1°C. Frames were captured with a camera (BASLER A311fc) having 640×480 pixels at a resolution of 6 pixels μm^{-1} and a frame rate of

27 frames s^{-1}. The optical resolution was of the order of a micron. Typical recording times of one particular vesicle were of the order of 15 s. The time limitation for the recording was mainly caused by bleaching of the fluorecence dye and did not reach the physical limit set by the rotational and translational diffusion of the entire vesicle.

The central position of each domain on the vesicle as a function of time can be characterized by the vector $\boldsymbol{c}_i = R(\sin\vartheta_i\cos\varphi_i, \sin\vartheta_i\sin\varphi_i, \cos\vartheta_i)$, where $\vartheta_i(t)$ and $\varphi_i(t)$ are the polar and azimuth angle. In a domain diffusion experiment the raw data are the time dependent vectors $\boldsymbol{c}_i(t)$ pointing to the centres of the domains. The vertical position z of the domain can be constructed from the lateral position assuming a spherical shape of the vesicle.

A change in position of a domain on a vesicle is not necessarily due to translational diffusion through the membrane. This can be easily seen by considering a vesicle with very high viscosity of the bilayer. In a flat membrane an infinite membrane viscosity would simply impede any translational diffusion. A vesicle however can perform rotational diffusion in the same way a solid sphere reorients in a liquid. In the generic case both types of motion are coupled. A decoupling of both types of motion can be either performed experimentally by measuring the motion of a domain 'relative' to some reference domains. We will discuss the simplest form of measuring such 'relative' motion in § 4 dedicated to two-domain rheology. The other possibility is to measure the absolute motion of a domain and derive a theoretical expression for the total diffusion of the domain. In § 3 we follow the second approach.

There are two ways to look at the diffusion of a domain on the vesicle. One is to watch the domain from three-dimensional space, the other is to consider the domain moving in a two-dimensional curved space. If we consider the first point of view, we would say that the domain is confined to the vesicle surface and the domain moves in an erratic way on the surface around the centre of the vesicle. Thus the motion of the domain is a rotational diffusion of the domain around the vesicle centre. According to the second point of view the diffusion of the domain is an erratic 'translational' motion through a curved membrane. Both points of view have their advantages. The advantage of the three-dimensional approach is that the three-dimensional space is Euclidian, while the membrane surface is non-Euclidian. We will distinguish motions described by the 'non-Euclidian' point of view from the Euclidian point of view by marking it in quotes throughout the text. Euclidian rotational motion of the domain is mathematically easier to describe than non Euclidian 'translational' motion. Let us consider the Euclidian point of view: an infinitesimal change in domain position during the time $\mathrm{d}t$ occurs due to an infinitesimal rotation $\mathrm{d}\boldsymbol{c}_i = \boldsymbol{\omega}_i \times \boldsymbol{c}_i \, \mathrm{d}t$ of the position, where $\boldsymbol{\omega}_i$ denotes the momentary angular frequency of rotation of the ith domain around the vesicle centre. Hence the diffusion of the domain is characterized by the rotational diffusion of the orientation of the vector $\boldsymbol{c}_i$ on the vesicle surface in the same sense as a director of a nematic liquid crystal performs rotational diffusion. The three-dimensional rotational diffusion should not be confused with the two-dimensional 'rotational' diffusion of the domain in the membrane which corresponds to 'rotations' of a domain around the domain centre not to rotations of a domain around the vesicle centre. In this work the term rotational diffusion will always correspond to the rotation of the domain around the vesicle centre.

In general, the diffusion of the domains will depend on their geometrical arrangement on the vesicle, described by the domain sizes and their polar and azimuthal angles. Two arrangements of the domains will have the same diffusion constants if the two arrangements can be mapped on top of each other by a solid rotation. Instead of using individual coordinates of the domains, we might use three

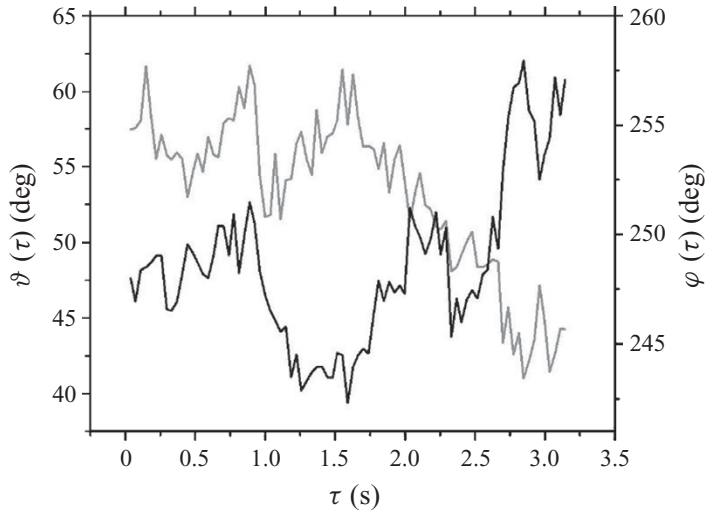

FIGURE 2. Time evolution of the polar and azimuthal angle of a domain of size $a = 0.7\,\mu\text{m}$ in a vesicle of size $R = 7.4\,\mu\text{m}$ of composition (DOPC/DPPC/Chol = 40/40/20) at temperature $T = 23^{\circ}\text{C}$.

Euler angles to describe the solid rotation of all domains on the vesicle and a set $\mathscr{C}$ of conformational coordinates describing the relative conformation of the domains. Using these conformational coordinates we may define the diffusion constant $D_{ij}(\mathscr{C})$ of a specific conformation via the correlation function of the angular velocity fluctuations of the domains following the general theory of Kubo (1957):

$$D_{ij}(\mathscr{C}) = \int_0^\infty \mathrm{d}\tau \langle \boldsymbol{\omega}_i(t)\boldsymbol{\omega}_j(t+\tau)\rangle_{\mathscr{C}}, \tag{2.1}$$

where

$$\langle X\rangle_{\mathscr{C}} = \int \mathrm{d}\mathscr{C}' \int \mathrm{d}t\, X(\mathscr{C}', t)\delta(\mathscr{C} - \mathscr{C}') \tag{2.2}$$

denotes the ensemble and time average over all arrangements having the conformation $\mathscr{C}$. If there are more than one domain, the diffusion constant becomes a symmetric tensor and a diagonalization yields the eigenvalues $D_\lambda(\mathscr{C})$ of the different normal modes of diffusion for the conformation $\mathscr{C}$.

3. One-domain rheology: experiment

For the case of one single domain diffusing in a vesicle the only conformational variable is the conserved size $a = R\cos\theta$ of the domain. Here θ denotes the conical opening angle of the domain on the vesicle (figure 1). Since all conformational coordinates are invariants of the diffusive motion, there exists a description of rotational diffusion that is analogous to the description of diffusion in flat systems in terms of a mean square displacement. Using spherical coordinates the position of the domain can be described by the polar and azimuthal angles (ϑ, φ) of the centre of the domain. Figure 2 shows the time evolution of the domain position as a function of time for a domain of size $a = 0.7\,\mu\text{m}$ in a vesicle of size $R = 7.5\,\mu\text{m}$ of composition (DOPC/DPPC/Chol = 40/40/20) at temperature $T = 23^{\circ}\text{C}$. The diffusion of the domain results in fluctuations of the polar and azimuthal angles.

The role of displacement is taken by the angular separation between the domain at different times. The angular separation between the position on the sphere at time t_i

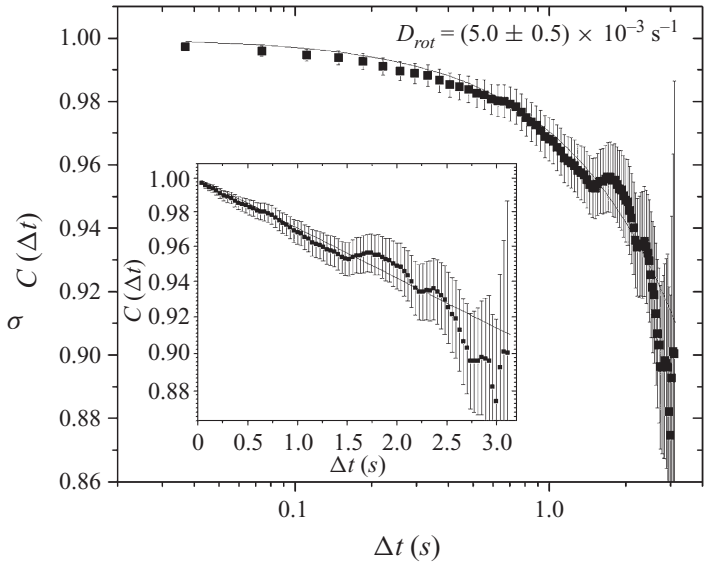

FIGURE 3. Plot of the experimental rotational correlation function $C(\Delta t)$ as computed from the domain trajectory of figure 2 via (3.1) (symbols) together with a fit to a random walk diffusion according to (3.2) (line graph). The inset shows the same data on a linear time scale. The exponential decay is indistinguishable from a linear decay since the correlation time was much shorter than the rotational diffusion constant.

and time t_j is then given by the angle $\cos(\gamma(t_i, t_j)) = \mathbf{c}(t_i) \cdot \boldsymbol{c}(t_j) = \cos\vartheta(t_i)\cos\vartheta(t_j) + \sin\vartheta(t_i)\sin\vartheta(t_j)\cos(\varphi(t_i) - \varphi(t_j))$. We define the angular correlation function following Berne & Precora (2000):

$$C(\Delta t) = \frac{\sum_{i,j} \delta_{\Delta t, t_j - t_i} P_2(\cos(\gamma(t_i, t_j)))}{\sum_{i,j} \delta_{\Delta t, t_j - t_i}}, \tag{3.1}$$

where $\delta_{\Delta t, t_j - t_i}$ denotes the Kronecker delta and Δt is the time separation between t_i and t_j and the sum is taken over all pairs of data taken at different times having the same time separation. $P_2(\cos\gamma) = 3/2\cos^2\gamma - 1/2$ is the Legendre polynomial of degree 2. The definition of the angular correlation function in (3.1) is the same as used for the director orientation in liquid crystals (Berne & Precora 2000). For a random walk of the domain on a spherical surface, the rotational correlation function exponentially decreases with the time lag Δt as (Berne & Precora 2000)

$$C(\Delta t) = \mathrm{e}^{-6D_{rot}\Delta t}, \tag{3.2}$$

where D_{rot} denotes the rotational diffusion constant of the domain. Hence a fit of the angular correlation function equations (3.1) to (3.2) will yield the rotational diffusion constant.

Figure 3 shows the angular correlation function $C(\Delta t)$ as computed from the domain trajectory of figure 2 via (3.1) together with a fit to a random walk diffusion according to (3.2). The fit describes the data well for smaller correlation times. At large times the experimental data starts deviating since there is insufficient statistics. Such decrease in statistics with the correlation time is inherent to all experimental correlation functions. The fit corresponds to a rotational diffusion constant of $D_{rot} = 5.0 \times 10^{-3}\ \mathrm{s}^{-1}$.

On short time scales the probability to diffuse away far from the original position is low such that the domain will not sense the confinement imposed by the curved surface of the vesicle. Hence in the limit $\Delta t \to 0$ also the angle γ vanishes ($\gamma \to 0$)

and we might expand (3.1) and (3.2) to obtain the connection of the three-dimensional rotation diffusion constant with the apparent two-dimensional 'translational' diffusion of the domain. We find

$$\lim_{\Delta t\to 0} P_2(\cos\gamma) = 3/2\cos^2\gamma - 1/2 \to 1 - 3/2\gamma^2 \tag{3.3}$$

and

$$\lim_{\Delta t\to 0} \mathrm{e}^{-6D_{rot}\Delta t} \to 1 - 6D_{rot}\Delta t. \tag{3.4}$$

From (3.3) and (3.4) we conclude that in the tangent space (The tangent space is the locally flat neighbourhood of the momentary domain position, where effects of curvature can be still neglected.) to the vesicle the mean square displacement r^2 grows linearly with the time lag Δt as

$$r^2 = R^2\gamma^2 = 4R^2 D_{rot}\Delta t = 4D_{trans}\Delta t \qquad \text{for } \Delta t \to 0. \tag{3.5}$$

Equation (3.5) is the standard two-dimensional 'translational' diffusion law with the apparent 'translational' diffusion constant $D_{trans} = R^2 D_{rot}$. The apparent 'translational' diffusion defined in this way contains both the 'diffusion' of the domain in the membrane as well as the rigid rotational diffusion of the entire vesicle. For the rotational correlation function fitted in figure 3 we obtain the corresponding apparent 'translational' diffusion constant as $D_{trans} = 2.7\times 10^{-13}\,\mathrm{m^2\,s^{-1}}$. The conical angle θ is given by $\sin\theta = a/R$ (see figure 1). It measures the size of the domain in units of the size of the vesicle. Since the diffusion is due to thermal fluctuations then the rotational diffusion constant D_{rot} is related to the dimensionless friction coefficient f via the fluctuation dissipation theorem (Reichl 1980):

$$\frac{\eta_o R^3 \sin\theta}{k_B T} D_{rot} = \frac{1}{f}. \tag{3.6}$$

For the rotational diffusion constant fitted in figure 3 we obtain $f^{-1} = 4.2\times 10^{-2}$. The dimensionless friction coefficient

$$f = \frac{1}{\eta_o R^3 \sin\theta}\frac{\tau}{\omega} \tag{3.7}$$

is defined as the response in viscous torque τ of the domain when it is rotated with angular frequency ω. The dimensionless friction coefficient $f(\theta, \mathscr{H}, \mathscr{B}, \mathscr{H}_s)$ is a function of four dimensionless parameters: the conic angle θ of the domain, the relative bulk viscosity contrast $\mathscr{H} = (\eta_i - \eta_o)/\eta_o$ between the interior viscosity η_i and the exterior bulk fluid viscosity η_o of the vesicle, the Boussinesq number

$$\mathscr{B} = \eta_s^b/2\eta_o a \tag{3.8}$$

and the contrast $\mathscr{H}_s = (\eta_s^a - \eta_s^b)/\eta_s^b$ between the domain shear viscosity η_s^a and the surface shear viscosity η_s^b of the membrane embedding the domain. The dimensionless friction coefficient can be computed by solving the Stokes equation of the coupled bulk and membrane fluids. We will show in § 4 that a relatively simple analytic result exists for the special case $\mathscr{H}_s = 0$, where both bilayer phases have the same surface shear viscosity η_s. Once the analytic expression for the dimensionless friction coefficient is known, we can compare the dimensionless diffusion coefficient f^{-1} obtained from the experiment via (3.6) with the theoretical expression and extract the Boussinesq number $\mathscr{B}$ (and hence the surface shear viscosity η_s). As will be described in § 4 for

$\mathscr{H}_s = 0$ we obtain

$$\frac{1}{f} = \sum_{n=1}^{\infty} \frac{P_n^1(\cos\theta)^2}{2\pi \sin\theta n^2(n+1)^2[1 + \dfrac{n-1}{2n+1}(\mathscr{H} + 2(n+2)\mathscr{B}\sin\theta)]}, \tag{3.9}$$

where $P_n^1(\cos\theta)$ denotes the associated Legendre polynomial of the first kind of degree n and order 1. The sum in (3.9) quickly converges if the conic angle of the domain is large, and truncation of the sum at $n = 100$ gives results with errors less than 5 % for $\theta > \pi/20$. We may read off the value of the Boussinesq number from a plot of (3.9) versus $\mathscr{B}$ by looking at which Boussinesq number $\mathscr{B}$ the theoretical diffusion coefficient equation (3.9) coincides with the experimental diffusion coefficient equation (3.6) $f_{theory}^{-1}(\mathscr{B}) = f_{experiment}^{-1}$. The surface shear viscosity is then obtained via (3.8).

We define the sensitivity of the rheological method as

$$S = \frac{\mathrm{d}\ln f}{\mathrm{d}\ln \mathscr{B}}. \tag{3.10}$$

The sensitivity S expresses how much a relative change in viscosity $\Delta\eta_s/\eta_s$ will be reflected in a relative change in diffusion constant $\Delta D/D$. If the diffusion constant does not change significantly with the surface shear viscosity, then one cannot measure the surface shear viscosity to a high accuracy. This is indeed the case in single-domain rheology at both low and high Boussinesq numbers. At low Boussinesq number the diffusion of a single domain is dominated by the dissipation to the water and hence fairly independent of the surface shear viscosity. The same is true for high surface shear viscosity, where the vesicle performs rotational diffusion almost like a solid sphere. Only in the cross-over regime $1 < \mathscr{B} < 1/\sin\theta$ does one achieve significant sensitivity to allow a precise measurement of the surface shear viscosity.

We define the resolution limit of the method as $D_{res} = \Delta x_{min}^2/R^2\Delta t_{max}$ where Δx_{min} is the spatial resolution of the microscope and Δt_{max} is the maximum time of the measurement. The time limit for the measurement in one- and two-domain rheology is set by the time the domain will stay in the focus of the microscope which is given by $\Delta t_{max} = D_{rot}^{-1}$. We find that $D_{res} = \Delta x_{min}^2/R^2 D_{rot}$. Since the spatial resolution is smaller than the vesicle size, $\Delta x_{min} < R$ also the rotational diffusion constant is above the resolution limit $D_{res} < D_{rot}$. We then define the resolution of a diffusion constant as

$$Res = \frac{D}{D_{res}} = \frac{R^2}{\Delta x_{min}^2}\frac{D}{D_{rot}}. \tag{3.11}$$

A high resolution corresponds to $Res > 1$. A diffusion constant cannot be resolved when $Res < 1$. The resolution of single-domain rheology is $Res = R^2/\Delta x_{min}^2 \approx (20\,\mu\mathrm{m}/0.5\,\mu\mathrm{m})^2 \approx 10^3$. In order to detect the surface shear viscosity one needs both sensitivity and resolution. We define the measurability by

$$M = Res \times S. \tag{3.12}$$

The higher the measurability the easier it is to obtain a value for the surface shear viscosity.

4. Two-domain rheology: experiment

One-domain rheology has the disadvantage to be sensitive to the surface shear viscosity of the vesicle membrane only in the cross-over region $1 < \mathscr{B} < 1/\sin\theta$ since

at higher Boussinesq numbers the apparent diffusion of the domain is mainly due to rotations of the entire vesicle. These rotations dissipate the vesicle energy by shearing the surrounding bulk liquid not the membrane. One might eliminate the solid rotation by measuring the relative motion of two or more domains on the vesicle. Such measurements are indeed possible and two-particle microrheology has been used successfully with colloidal particles. The mathematics of two-particle rheology (Prasad *et al.* 2006), however, significantly differs from the results for one particle even when the system is flat rather than curved. Hydrodynamic interactions between two domains lead to correlated motion of the domains. Their relative motion is generally not the result of an independent motion of the single domains. Differences in the motion arising from hydrodynamic correlations (Levine & MacKintosh 2002; Fischer 2003) compared to an uncorrelated motion are especially large at large Boussinesq numbers $\mathscr{B} > \gamma/2\theta$ where γ denotes the angular separation of the two domains. Under these circumstances, hydrodynamic correlations are mediated by long range interfacial hydrodynamic interactions. Each domain has two degrees of freedom to move in the membrane giving rise to four normal modes of diffusion. For equally sized domains $a_1 = a_2$ symmetry considerations let us recognize those normal modes as the combined and relative motion of both domains along and perpendicular to the geodesics connecting both domains (figure 1). In § 4 we will derive equations connecting the Brownian angular velocity of all four modes with the corresponding Brownian torques at the domain edges. Numerical solution of the equations yields the combined and relative diffusion coefficients $f^{-1}_{comb,\parallel}$, $f^{-1}_{rel,\parallel}$, $f^{-1}_{comb,\perp}$ and $f^{-1}_{rel,\perp}$ parallel and perpendicular to the geodesic connecting the domain centres of the two domains. Diffusion of both domains will result in a change in separation γ. Since all four diffusion coefficients depend on the separation γ, a linear relation between the mean square displacement and time ($\gamma^2 \propto \Delta t$) will no longer hold over times allowing for significant change in γ. In a two-domain rheology experiment, the experimental data will be the vectors $\boldsymbol{c}_1(t)$ and $\boldsymbol{c}_2(t)$ describing the position of the two domains on the vesicle. We define the vector $\boldsymbol{c}_3(t)$ as $\boldsymbol{c}_3(t) = R\boldsymbol{c}_1 \times \boldsymbol{c}_2/|\boldsymbol{c}_1 \times \boldsymbol{c}_2|$. The vectors $\boldsymbol{c}_1(t)$, $\boldsymbol{c}_2(t)$ and $\boldsymbol{c}_3(t)$ define a basis for the three-dimensional space. The momentary angular velocities of both domains are

$$\boldsymbol{\omega}_1 = \frac{1}{R^2}\boldsymbol{c}_1 \times \frac{\mathrm{d}\boldsymbol{c}_1}{\mathrm{d}t} \qquad \text{and} \qquad \boldsymbol{\omega}_2 = \frac{1}{R^2}\boldsymbol{c}_2 \times \frac{\mathrm{d}\boldsymbol{c}_2}{\mathrm{d}t}. \tag{4.1}$$

We introduce a reciprocal basis as

$$\boldsymbol{q}_i = \frac{1}{2}\epsilon_{ijk}\frac{\boldsymbol{c}_j \times \boldsymbol{c}_k}{|(\boldsymbol{c}_1 \times \boldsymbol{c}_2)\cdot \boldsymbol{c}_3|}, \tag{4.2}$$

where ϵ_{ijk} denotes the Levi-Civita symbol. The vectors $\boldsymbol{c}_1$, $\boldsymbol{q}_2$ and $\boldsymbol{q}_3$ are orthogonal to each other and the vectors $\boldsymbol{q}_2$ and $\boldsymbol{q}_3$ span the tangent space to the domain located at the position $\boldsymbol{c}_1$. The same is true for the vectors $\boldsymbol{c}_2$, $\boldsymbol{q}_3$ and $\boldsymbol{q}_1$. The reciprocal vectors $\boldsymbol{q}_3$ and $\boldsymbol{q}_1$ span the tangent space to the domain located at the position $\boldsymbol{c}_2$. We decompose the angular velocities of both domains into combined and relative angular velocities parallel and perpendicular to the interconnecting geodesics between both domains via

$$\left.\begin{aligned} \boldsymbol{\omega}_1 &= \frac{\omega_{comb,\parallel} + \omega_{rel,\parallel}}{\sqrt{2}}\frac{\boldsymbol{q}_3}{|q_3|} + \frac{\omega_{comb,\perp} + \omega_{rel,\perp}}{\sqrt{2}}\frac{\boldsymbol{q}_2}{|q_2|}, \\ \boldsymbol{\omega}_2 &= \frac{\omega_{comb,\parallel} - \omega_{rel,\parallel}}{\sqrt{2}}\frac{\boldsymbol{q}_3}{|q_3|} - \frac{\omega_{comb,\perp} - \omega_{rel,\perp}}{\sqrt{2}}\frac{\boldsymbol{q}_1}{|q_1|}. \end{aligned}\right\} \tag{4.3}$$

Note that there is no component of $\boldsymbol{\omega}_1$ along $\boldsymbol{c}_1$ and no component of $\boldsymbol{\omega}_2$ along $\boldsymbol{c}_2$. This is because a 'rotation' of domain 1 around $\boldsymbol{c}_1$ leaves both the position and the shape of the domain unchanged and cannot be detected by the microscope. Note also that the rotations perpendicular to the connecting geodesic are around different axes ($\boldsymbol{q}_2$ and $\boldsymbol{q}_1$) for domains 1 and 2. It is straightforward to resolve (4.3) for the combined and relative angular velocities $\omega_{comb,\parallel}$, $\omega_{rel,\parallel}$, $\omega_{comb,\perp}$ and $\omega_{rel,\perp}$ as

$$\left.\begin{aligned}
\omega_{comb,\parallel} &= \frac{|q_3|}{\sqrt{2}}(\boldsymbol{\omega}_1+\boldsymbol{\omega}_2)\cdot\boldsymbol{c}_3,\\
\omega_{rel,\parallel} &= \frac{|q_3|}{\sqrt{2}}(\boldsymbol{\omega}_1-\boldsymbol{\omega}_2)\cdot\boldsymbol{c}_3,\\
\omega_{comb,\perp} &= \frac{\boldsymbol{\omega}_1\cdot\boldsymbol{c}_2|q_2|-\boldsymbol{\omega}_2\cdot\boldsymbol{c}_1|q_1|}{\sqrt{2}},\\
\omega_{rel,\perp} &= \frac{\boldsymbol{\omega}_1\cdot\boldsymbol{c}_2|q_2|+\boldsymbol{\omega}_2\cdot\boldsymbol{c}_1|q_1|}{\sqrt{2}}.
\end{aligned}\right\} \tag{4.4}$$

From (4.3) and (4.4) we obtain the relative velocity $\boldsymbol{u}_{1,rel}$ and $\boldsymbol{u}_{2,rel}$ between both domains at the position of domains 1 and 2:

$$\left.\begin{aligned}
\boldsymbol{u}_{1,rel} &= \sqrt{2}\omega_{rel,\parallel}\frac{\boldsymbol{c}_1\times\boldsymbol{q}_3}{|q_3|}+\sqrt{2}\omega_{rel,\perp}\frac{\boldsymbol{c}_1\times\boldsymbol{q}_2}{|q_2|},\\
\boldsymbol{u}_{2,rel} &= -\sqrt{2}\omega_{rel,\parallel}\frac{\boldsymbol{c}_2\times\boldsymbol{q}_3}{|q_3|}-\sqrt{2}\omega_{rel,\perp}\frac{\boldsymbol{c}_2\times\boldsymbol{q}_1}{|q_1|},
\end{aligned}\right\} \tag{4.5}$$

where $\boldsymbol{u}_{1,rel}$ and $\boldsymbol{u}_{2,rel}$ are 'relative' velocities in the sense of a two-dimensional non-Euclidian geometry on the vesicle surface. They are different from the Euclidian three-dimensional relative velocity $\mathrm{d}\boldsymbol{c}_1/\mathrm{d}t-\mathrm{d}\boldsymbol{c}_2/\mathrm{d}t$ that usually will not be tangential to the sphere. The 'relative' velocity $\boldsymbol{u}_{1,rel}$ is obtained in the following way. First, 'parallel' transport (Misner, Thorne & Wheeler 1973) of the velocity $\mathrm{d}\boldsymbol{c}_2/\mathrm{d}t$ from the position of domain 2 towards the domain 1 along the interconnecting geodesic will result in a velocity $\tilde{\boldsymbol{u}}_2$. This allows mapping of the velocity $\mathrm{d}\boldsymbol{c}_2/\mathrm{d}t$ of domain 2 defined in the tangent space of domain 2 into the tangent space of domain 1. In curved space such 'parallel' transport is necessary since vectors can be compared only when residing in the same tangent space. Only after this 'parallel' transport is achieved can the velocity $\tilde{\boldsymbol{u}}_2$ be subtracted from the velocity $\mathrm{d}\boldsymbol{c}_1/\mathrm{d}t$ of domain 1 to yield the 'relative' velocity $\mathrm{d}\boldsymbol{c}_1/\mathrm{d}t-\tilde{\boldsymbol{u}}_2$ evaluated in the tangent space of domain 1. Measurements of 'relative' velocities in curved space are usually quite difficult. We have taken advantage of the fact that the curved surface of the vesicle is embedded into a Euclidian three-dimensional space which made the computation of the 'relative' velocities in (4.5) much simpler than when performing the same operation in an arbitrarily curved space. 'Parallel' transport is just a rotation around the vector $\boldsymbol{c}_3$ by the angle γ. The difference between relative velocity in three-dimensional space and 'relative' velocity on a curved surface can be most easily understood when considering two domains, one sitting at the north pole and the other sitting at the south pole. Assume that both domains start moving 'towards' each other along the same longitude with the same velocities ($\mathrm{d}\boldsymbol{c}_1/\mathrm{d}t=\mathrm{d}\boldsymbol{c}_2/\mathrm{d}t$). The difference in velocities in three-dimensional space is zero. It makes sense in a two-dimensional curved space to speak of a 'relative' motion 'towards' each other and to measure a 'relative' velocity that will be just ($\mathrm{d}\boldsymbol{c}_1/\mathrm{d}t+\mathrm{d}\boldsymbol{c}_2/\mathrm{d}t$) not ($\mathrm{d}\boldsymbol{c}_1/\mathrm{d}t-\mathrm{d}\boldsymbol{c}_2/\mathrm{d}t$) . The plus sign instead of the minus sign arises because 'parallel' transport (a three-dimensional rotation of π in the three-dimensional

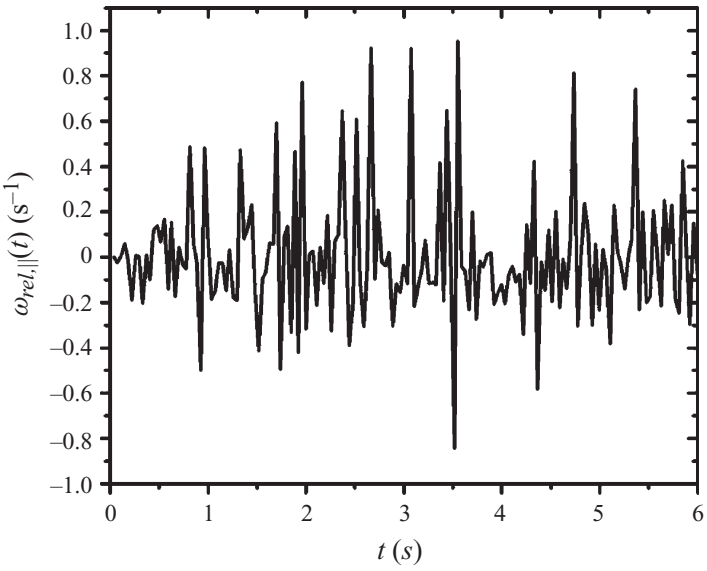

FIGURE 4. Plot of the relative longitudinal angular frequency $\omega_{rel,\parallel}(t)$ versus time of two domains with sizes $a_1 = 1.3\,\mu\text{m} \approx a_2 = 1.0\,\mu\text{m}$ separated by an angle of $\gamma = 30^\circ$ and residing in a vesicle of size $R = 12.5\,\mu\text{m}$ and composition (DOPC/DPPC/Chol = 16/64/20) at temperature $T = 23^\circ\text{C}$.

Euclidian sense) of the velocity of the domain at the south pole 'towards' the north pole just reverses the sign of the velocity.

Experimental measurements using two-domain rheology must average the angular velocity correlations

$$D_\lambda = \int_0^\infty \mathrm{d}\Delta t \langle \omega_\lambda(\gamma, t)\omega_\lambda(\gamma, t + \Delta t)\rangle \tag{4.6}$$

for each separation γ and each mode $\lambda = (comb, \parallel)$, $(rel, \parallel)$, $(comb, \perp)$ and $(rel, \perp)$ individually. Since the diffusion of each mode is due to thermal fluctuations the diffusion constants D_λ are related to the corresponding friction coefficients via the fluctuation dissipation theorem:

$$\frac{\eta_o R^3 \sin\theta}{k_B T} D_\lambda = \frac{1}{f_\lambda}, \tag{4.7}$$

where the friction coefficients describe the response in the viscous torque τ_λ,

$$f_\lambda = \frac{1}{\eta_o R^3 \sin\theta} \frac{\tau_\lambda}{\omega_\lambda}, \tag{4.8}$$

arising due to a rotation of both domains with frequency $\boldsymbol{\omega}_1(\lambda)$ and $\boldsymbol{\omega}_2(\lambda)$ and where the viscous torque has been decomposed into normal modes in a way analogous to the decomposition of frequencies equation (4.3). The normalization factors in (4.3) ensures that the power dissipated by the relative motion of both domains is

$$\langle \tau_\lambda(\gamma, t)\omega_\lambda(\gamma, t')\rangle = k_B T \delta(t - t'). \tag{4.9}$$

In figure 4 we depict the behaviour of the relative longitudinal angular frequency $\omega_{rel,\parallel}(t)$ of two domains with sizes $a_1 = 1.3\,\mu\text{m} \approx a_2 = 1.0\,\mu\text{m}$ separated by an angle of $\gamma = 30^\circ$ and residing in a vesicle of size $R = 12.5\,\mu\text{m}$ consisting of composition

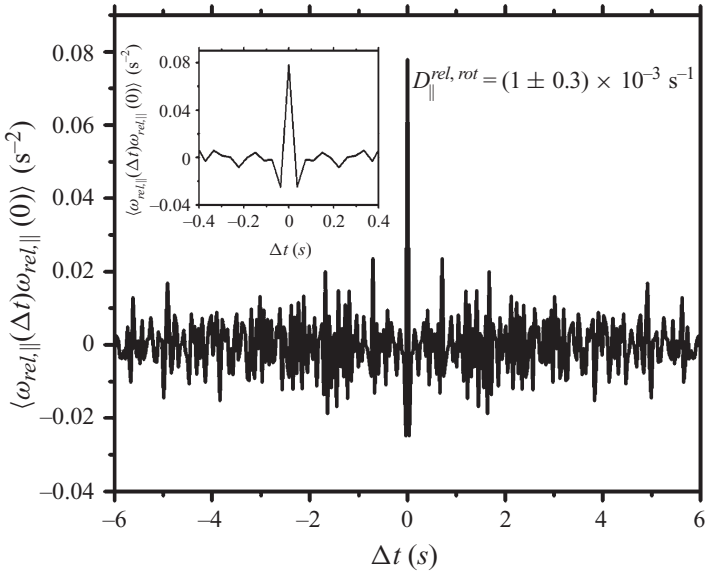

FIGURE 5. Plot of the auto correlation function $\langle \omega_{rel,\parallel}(\gamma, t)\omega_{rel,\parallel}(\gamma, t + \Delta t)\rangle$ computed from the data in figure 4. The diffusion constant $D_{rel,\parallel} = 1 \times 10^{-3}$ s^{-1} corresponds to half the area under the auto correlation function. The region of the peak of the autocorrelation function at $\Delta t \approx 0$ that contributes to the diffusion is depicted with higher resolution in the inset.

(DOPC/DPPC/Chol = 16/64/20) at temperature $T = 23°$C. The relative longitudinal angular frequency fluctuates around zero and does not change the separation γ by a significant amount during the time of measurement. The autocorrelation function $\langle \omega_{rel,\parallel}(\gamma, t)\omega_{rel,\parallel}(\gamma, t + \Delta t)\rangle$ is depicted in figure 5. The diffusion constant $D_{rel,\parallel}$ corresponds to half the area under the correlation function. Like the angular frequency, torque correlation in (4.9), also the angular frequency autocorrelation function, is delta correlated. The fluctuations persisting in figure 5 are due to the limited time of measurement and the integration in (4.6) is therefore taken over a time span of three frames, e.g. larger than the correlation time but smaller than the time of measurement.

Only the relative longitudinal motion of the domains results in a motion where the vesicle as a whole is at rest. Transversal relative motion results in a net rotation of the vesicle around the midpoint between both domains. Separation of relative and global motion of the vesicle therefore remains incomplete also for two-domain rheology. On a curved surface, combined motion into one direction means that the direction of the first domain is the same as the second after that the second direction is parallel transported (Misner *et al.* 1973) along the interconnecting geodesics to the first domain. The combined motion of both domains is the analogue of one domain rheology with two domains. The analysis of the two-domain rheology consists of the decomposition of the motion into the four modes and a measurement of the autocorrelation function of the angular velocity fluctuations of a particular mode, (4.6) at a fixed separation of domains. The diffusion constant of the particular mode is obtained from the ensemble and time average over these fluctuations. Again a comparison between the theoretical diffusion coefficients $f_{\lambda}^{-1}(\theta, \gamma, \mathscr{B})$ and the four different experimental diffusion constants determined from (4.7) allows extraction of the Boussinesq number and using (3.8), the surface shear viscosity. As described in §4 for $\mathscr{H}_s = 0$ and $\gamma = \pi$ two of the four modes become degenerate and we

obtain:

$$\left.\begin{aligned}\frac{1}{f_{rel,\parallel}} = \frac{1}{f_{comb,\perp}} &= 2\sum_{n=2,4,6\ldots}^{\infty} \frac{P_n^1(\cos\theta)^2}{2\pi\sin\theta n^2(n+1)^2[1+\dfrac{n-1}{2n+1}(\mathscr{H}+2(n+2)\mathscr{B}\sin\theta)]},\\ \frac{1}{f_{rel,\perp}} = \frac{1}{f_{comb,\parallel}} &= 2\sum_{n=1,3,5\ldots}^{\infty} \frac{P_n^1(\cos\theta)^2}{2\pi\sin\theta n^2(n+1)^2[1+\dfrac{n-1}{2n+1}(\mathscr{H}+2(n+2)\mathscr{B}\sin\theta)]}.\end{aligned}\right\} \tag{4.10}$$

The sum for the two domains in (4.10) differs from the corresponding equation (3.9) of a single domain in several aspects. The summation in (4.10) is only over odd (even) values of n. The summation quickly converges if the conic angle of both domains and the separation angle $2(\pi/2-\theta)$ are large. Moreover truncation of the sum at $n=100$ gives results with errors less than 5 % for $\theta > \pi/20$ and $2(\pi/2-\theta) > \pi/20$. We may estimate the value of the Boussinesq number from a plot of (4.10) versus $\mathscr{B}$ by looking where the theoretical diffusion coefficient of (4.10) equals the experimental diffusion coefficient determined from (4.7). The surface shear viscosity is then obtained via (3.8). The advantage of two-domain rheology with respect to one-domain rheology is that in some of the modes one gains sensitivity for the surface shear viscosity. One disadvantage is that such technique requires to statistically average the angular velocity correlations for a subset of events, where the domains have similar separation. Moreover, at high surface shear viscosity the rotational diffusion of the vesicle in the water is much faster than the relative diffusion of two domains. The time to observe these domains with high spatial resolution is limited by $\Delta t_{max} \approx D_{rot}^{-1}$ since for longer times both domains, which are originally located on the northern hemisphere of the vesicle, will diffuse to the southern hemisphere via the rotational diffusion of the entire vesicle and therefore be out of the focal plane of the objective. For large Boussinesq numbers, relative diffusion D_{rel} will eventually drop below the diffusion resolution limit $D_{rel} < D_{res}$. In two-domain rheology one will gain the missing sensitivity at high Boussinesq numbers using the relative longitudinal mode but will lose resolution in the measurement of the relative diffusion constants as compared to the high resolution of measuring rotational diffusion constants with single-domain rheology.

5. Theoretical

In this section we outline the derivation of the single-domain diffusion constant equation (3.9) and the two-domain diffusion constants equation (4.10). The bulk liquid inside and outside the vesicle fulfills the Stokes equation:

$$\left.\begin{aligned}-\nabla p + \eta\Delta\boldsymbol{u} &= 0,\\ \nabla\cdot\boldsymbol{u} &= 0.\end{aligned}\right\} \tag{5.1}$$

Here $\boldsymbol{u}$ is the bulk fluid velocity. The dynamic bulk ($\boldsymbol{P}$) and surface ($\boldsymbol{P}_s$) stress tensors are given by

$$\left.\begin{aligned}\boldsymbol{P} &= -p\mathbf{1} + \eta\left(\nabla\boldsymbol{u} + [\nabla\boldsymbol{u}]^t\right),\\ \boldsymbol{P}_s &= \sigma_s\boldsymbol{I}_s + \eta_s\left(\nabla_s\boldsymbol{u}_s\cdot\boldsymbol{I}_s + \boldsymbol{I}_s\cdot[\nabla_s\boldsymbol{u}_s]^t\right),\end{aligned}\right\} \tag{5.2}$$

where p is the bulk pressure, η is the bulk viscosity, σ_s is the surface tension and η_s is the surface shear viscosity. The index s is used for quantities defined at the vesicle

surface. They are obtained from the corresponding bulk quantities by projection onto the tangent space of the vesicle using the surface idem factor $\boldsymbol{I}_s = \mathbf{1} - \boldsymbol{nn}$, where $\boldsymbol{n}$ is the normal vector to the vesicle surface (i.e. $\boldsymbol{u}_s = \boldsymbol{I}_s \cdot \boldsymbol{u}$, $\nabla_s = \boldsymbol{I}_s \cdot \nabla$). To compute the resistance of the domain to the action of an external force we assume an external surface force density $\boldsymbol{f}_s$ distributed around the edge of the domain (figure 1). The vesicle surface is assumed incompressible and the divergence of the dynamic surface tension tensor is balanced by the traction $\boldsymbol{n} \cdot \|\boldsymbol{P}\| \cdot \boldsymbol{I}_s$ from the two bulk liquids and by the surface force density:

$$\left.\begin{aligned} \boldsymbol{n} \cdot \|\boldsymbol{P}\| \cdot \boldsymbol{I}_s = \boldsymbol{f}_s + \nabla_s \cdot \boldsymbol{P}_s, \\ \nabla_s \cdot \boldsymbol{u}_s = 0. \end{aligned}\right\} \tag{5.3}$$

Here $\|\boldsymbol{P}\|$ denotes the discontinuity of the bulk stress tensor across the vesicle interface. In general, the vesicle interior might have different properties than the exterior and we denote the velocities inside and outside the vesicle by $\boldsymbol{u}_i$ and $\boldsymbol{u}_o$. η_i and η_o are the bulk viscosities inside and outside the vesicle. In general, we also will have two surface viscosities, one for the domain η_s^a and one η_s^b for the rest of the membrane. We have so far discussed the rheological properties of the bulk fluid and the membrane. Of course there are also the rheological properties of the one-dimensional boundary between the portion of the membrane within the domain and the rest of the membrane. A one-dimensional line cannot be sheared and there is no analogue to the shear viscosities of the membrane and the bulk on the domain edge. However, the presence or absence of linactants (Trabelsi *et al.* 2006) (molecules that preferentially adsorb to the domain edge) will have a pronounced effect on the line compressibility and the line dilatational viscosity of the edge. The general line stress tensor would hence read

$$\boldsymbol{P}_l = (\sigma_l + \eta_l^{dil} \nabla_l \cdot \boldsymbol{u}_l) \boldsymbol{I}_l \tag{5.4}$$

with σ_l the line tension, η_l^{dil} the line dilatational viscosity, $\boldsymbol{I}_l$ the line idem factor, ∇_l the line gradient and $\boldsymbol{u}_l$ the line velocity. The Stokes equation for the line edge then reads

$$\boldsymbol{n}_l \cdot \|\boldsymbol{P}_s\| \cdot \boldsymbol{I}_l = \nabla_l \cdot \boldsymbol{P}_l, \tag{5.5}$$

where $\|\boldsymbol{P}_s\|$ denotes the discontinuity of the surface stress tensor across the edge of the domain. The equation of continuity reads

$$\nabla_l \cdot (\rho_l \boldsymbol{u}_l) = 0 \tag{5.6}$$

with ρ_l the linactant line density at the domain edge. A closure of the equations requires a constitutive equation for the line tension $\sigma_l(\rho_l)$. Little is known about the presence or absence of linactants, and even less is known about their compressibility and dilatational viscosity. Fluorescently labelled molecules sometimes act as linactants. Here we will assume a free domain edge without linactants $\rho_l = 0$ and $\eta_l^{dil} = 0$ such that $\nabla_l \sigma_l = 0$. For a free domain edge all rheological properties of the domain edge vanish and we find that all domain edge forces parallel to the domain edge vanish. We will hence assume that the surface force $\boldsymbol{f}_s$ in (5.3) is concentrated at the domain edge and pointing normal to the domain edge.

We will solve the problem in several steps. Firstly, we reduce the vector equations to scalar equations. In the second step, the relations between the torque and the velocities are reduced to equations solely involving velocities and torques on the vesicle surface. The third step reduces the relations to the velocity and torque fields on the domain edges. The equations on the domain edge are one-dimensional and can therefore be solved in a straightforward way.

We impose spherical coordinates r, ϑ and φ centred in the vesicle with the corresponding unit vectors $\boldsymbol{e}_r$, $\boldsymbol{e}_\vartheta$ and $\boldsymbol{e}_\varphi$. R is the radius of the vesicle.

The general solution of the bulk Stokes equation (5.1) can be written as

$$\boldsymbol{u} = \eta \int \mathrm{d}^3\boldsymbol{r}' \frac{\nabla p(\boldsymbol{r}')}{\boldsymbol{r}-\boldsymbol{r}'} + \nabla \Xi + (\nabla \times \boldsymbol{r})\Psi, \tag{5.7}$$

where p, Ξ and Ψ are scalar functions satisfying the Laplace equation $\nabla^2 p = \nabla^2 \Xi = \nabla^2 \Psi = 0$. Due to the incompressibility of the bulk velocity and the surface velocity on the vesicle, the flow can be described by the function Ψ only and $p = \Xi = 0$. It has been shown in the work of Saffmann & Delbrück (1975) that the incompressibility of the bulk and interfacial liquids causes all streamlines to be parallel to the interface and leads to a flow that is free of pressure gradients. This fact also holds when the interface is spherical and we therefore neglect the pressure gradients from the very beginning Fischer *et al.* (2006). The tangential stress-boundary condition (5.3) takes the form Edwards, Brenner & Wasan (1991):

$$-r\eta_o \frac{\partial \boldsymbol{u}_o/r}{\partial r} + r\eta_i \frac{\partial \boldsymbol{u}_i/r}{\partial r}\Bigg)_s = \boldsymbol{f}_s + \nabla_s \sigma_s + \eta_s \left\{ \boldsymbol{e}_r \times \nabla_s \left[(\nabla_s \times \boldsymbol{u}_s) \cdot \boldsymbol{e}_r \right] - \frac{2}{R^2} \boldsymbol{u}_s \right\}. \tag{5.8}$$

Using (5.7) and scalar multiplying (5.8) with $\boldsymbol{r} \times \nabla$ results in

$$-\nabla \cdot \boldsymbol{\tau}_s = \hat{\Lambda}_s \Psi, \tag{5.9}$$

where

$$\boldsymbol{\tau}_s = \boldsymbol{r} \times \boldsymbol{f}_s \tag{5.10}$$

denotes the surface torque density acting on the surface of the vesicle and $\hat{\Lambda}_s$ is the surface rheological operator:

$$\hat{\Lambda}_s \Psi = \left\| r \frac{\partial}{\partial r} r \nabla_s^2 \eta \Psi \right\|_{r=R} + \eta_s(\vartheta, \varphi) R^2 \nabla_s^2 \left(\nabla_s^2 + \frac{2}{R^2} \right) \Psi. \tag{5.11}$$

If we set the surface shear viscosity to be constant $\bar{\eta}_s = (\eta_s^a + \eta_s^b)/2$ over the entire vesicle membrane, the surface rheological operator $\bar{\hat{\Lambda}}_s = \hat{\Lambda}_s(\eta = \bar{\eta})$ commutes with the operator $\nabla \times \boldsymbol{r}$ and with the surface Laplace operator $\nabla_s^2 = (1/r^2)(\nabla \times \boldsymbol{r})^2$. It therefore follows that the functions

$$\left.\begin{aligned} \Psi_{nm}^e &= \begin{cases} \omega R \left(\dfrac{r}{R}\right)^n \cos(m\varphi) P_n^m(\cos\vartheta) & \text{for } r < R, \\ \omega R \left(\dfrac{R}{r}\right)^{n+1} \cos(m\varphi) P_n^m(\cos\vartheta) & \text{for } r > R, \end{cases} \\ \Psi_{nm}^o &= \begin{cases} \omega R \left(\dfrac{r}{R}\right)^n \sin(m\varphi) P_n^m(\cos\vartheta) & \text{for } r < R, \\ \omega R \left(\dfrac{R}{r}\right)^{n+1} \sin(m\varphi) P_n^m(\cos\vartheta) & \text{for } r > R, \end{cases} \end{aligned}\right\} \tag{5.12}$$

are simultaneous eigenfunctions of the three operators $\bar{\hat{\Lambda}}_s$, $\nabla \times \boldsymbol{r}$ and ∇_s^2. We will only solve problems that are mirror symmetric with respect to the operation $\varphi \to -\varphi$ and hence the solution will involve only the even functions Ψ_{nm}^e or only the odd functions Ψ_{nm}^o. We describe the solution for the even functions and will omit the index e in Ψ_{nm}^e, wherever the equation holds in the same way for the odd solutions. The

functions $P_n^m(\cos\vartheta)$ are associated Legendre polynomials. The eigenvalue equation for the operator $\bar{\hat{\Lambda}}_s$ on the vesicle surface reads

$$\bar{\hat{\Lambda}}_s \Psi_{nm} = \lambda_n \Psi_{nm} \tag{5.13}$$

with

$$\lambda_n = \eta_o R^{-1} n(n+1)\left[2n+1+(n-1)\left\{\mathscr{H}+2(n+2)(1+\mathscr{H}_s/2)\mathscr{B}\sin\theta\right\}\right]. \tag{5.14}$$

In the case that the membrane surface shear viscosity differs inside and outside the domain we write the surface shear viscosity as

$$\eta_s = 2\eta_o R\mathscr{B}\sin\theta\,[1+\mathscr{H}_s/2(1+\chi(\vartheta,\varphi))], \tag{5.15}$$

where the function $\chi(\vartheta,\varphi)$ is equal to ± 1 depending on whether (ϑ,φ) is a point inside or outside the domains:

$$\chi = \begin{cases} +1 & \text{for } \vartheta,\varphi \in \text{ domains,} \\ -1 & \text{for } \vartheta,\varphi \notin \text{ domains.} \end{cases} \tag{5.16}$$

We write the surface rheological operator as $\hat{\Lambda}_s = \bar{\hat{\Lambda}}_s + \chi(\vartheta,\varphi)\delta\hat{\Lambda}_s$. While the operators $\bar{\hat{\Lambda}}_s$ and $\delta\hat{\Lambda}_s$ commute with $\nabla\times\boldsymbol{r}$ and ∇_s^2, the operator $\hat{\Lambda}_s$ does not commute with $\nabla\times\boldsymbol{r}$ and ∇_s^2. We define the scalar product

$$\langle f, g\rangle = \int R^2 \sin\vartheta\,\mathrm{d}\vartheta\,\mathrm{d}\varphi f^*(\vartheta,\varphi) g(\vartheta,\varphi). \tag{5.17}$$

With the scalar product equation (5.17) the functions Ψ_{nm} are orthogonal and one has

$$\langle \Psi_{\tilde{n}\tilde{m}}, \Psi_{nm}\rangle = N_{\tilde{n}\tilde{m}}\delta_{\tilde{n}n}\delta_{\tilde{m}m} \tag{5.18}$$

with normalization constant

$$N_{\tilde{n}\tilde{m}} = \omega^2 R^4 \frac{2\pi}{2\tilde{n}+1}\frac{\tilde{n}+\tilde{m}!}{\tilde{n}-\tilde{m}!} \quad \text{for} \quad \tilde{m}\neq 0. \tag{5.19}$$

Taking the scalar product of $\Psi_{\tilde{n}\tilde{m}}$ with (5.9) results in

$$\begin{aligned} -\langle \Psi_{\tilde{n}\tilde{m}}, \nabla_s\cdot\boldsymbol{\tau}_s\rangle = \langle \Psi_{\tilde{n}\tilde{m}}, \hat{\Lambda}_s\Psi\rangle &= \sum_{nm}\langle \Psi_{\tilde{n}\tilde{m}}, [\bar{\hat{\Lambda}}_s + \chi\delta\hat{\Lambda}_s]\Psi_{nm}\rangle \frac{1}{N_{nm}}\langle \Psi_{nm}, \Psi\rangle \\ &= \sum_{nm}\lambda_{\tilde{n}}\Delta_{\tilde{n}\tilde{m},nm}\langle \Psi_{nm}, \Psi\rangle, \end{aligned} \tag{5.20}$$

where

$$\Delta_{\tilde{n}\tilde{m},nm} = \left\{\delta_{\tilde{n}n}\delta_{\tilde{m}m} + \langle \Psi_{\tilde{n}\tilde{m}}, \frac{\chi\delta\hat{\Lambda}_s}{\lambda_{\tilde{n}}N_{\tilde{n}\tilde{m}}}\Psi_{nm}\rangle\right\} = \left\{\delta_{\tilde{n}n}\delta_{\tilde{m}m} + \frac{\delta\lambda_n}{\lambda_{\tilde{n}}}\frac{\langle \Psi_{\tilde{n}\tilde{m}}, \chi(\vartheta,\varphi)\Psi_{nm}\rangle}{N_{\tilde{n}\tilde{m}}}\right\} \tag{5.21}$$

and

$$\delta\lambda_n = \eta_o R^{-1}(n-1)n(n+1)(n+2)\mathscr{H}_s\mathscr{B}\sin\theta. \tag{5.22}$$

Inverting (5.20) results in

$$\langle \Psi_{nm}, \Psi\rangle = -\sum_{\tilde{n}\tilde{m}}(\Delta^{-1})_{nm,\tilde{n}\tilde{m}}\frac{\langle \Psi_{\tilde{n}\tilde{m}}, \nabla_s\cdot\boldsymbol{\tau}_s\rangle}{\lambda_{\tilde{n}}}. \tag{5.23}$$

For a given torque density $\boldsymbol{\tau}_s$ on the vesicle we find the corresponding velocity profile as

$$\boldsymbol{u} = \sum_{nm} (\nabla \times \boldsymbol{r}) \Psi_{nm} \frac{\langle \Psi_{nm}, \Psi \rangle}{N_{\tilde{n}\tilde{m}}} = - \sum_{nm,\tilde{n}\tilde{m}} (\nabla \times \boldsymbol{r}) \Psi_{nm} (\Delta^{-1})_{nm,\tilde{n}\tilde{m}} \frac{\langle \Psi_{\tilde{n}\tilde{m}}, \nabla_s \cdot \boldsymbol{\tau}_s \rangle}{\lambda_{\tilde{n}} N_{\tilde{n}\tilde{m}}}. \tag{5.24}$$

We retain our freedom to place our domains of conical angle θ at an arbitrary latitude γ. It is therefore convenient to use an alternative system of spherical coordinates $(\vartheta_\gamma, \varphi_\gamma)$ with its pole centred in the domain at latitude γ. The transformation from coordinates (ϑ, φ) to $(\vartheta_\gamma, \varphi_\gamma)$ is then achieved via

$$\left.\begin{aligned} \vartheta &= \arccos(\cos\gamma \cos\vartheta_\gamma - \sin\gamma \sin\vartheta_\gamma \cos\varphi_\gamma), \\ \varphi &= \arctan \frac{\sin\varphi_\gamma}{\cos\gamma \cos\varphi_\gamma + \sin\gamma \cot\vartheta_\gamma}. \end{aligned}\right\} \tag{5.25}$$

The edge of the domain at latitude γ is then given by the equation $\vartheta_\gamma = \theta$. It is useful to define a second scalar product on the edge of the domain via

$$\{f, g\}_{\gamma,\theta} = \int_{-\pi}^{\pi} \frac{\mathrm{d}\varphi_\gamma}{\pi} f^*(\vartheta(\vartheta_\gamma = \theta, \varphi_\gamma), \varphi(\vartheta_\gamma = \theta, \varphi_\gamma)) g(\vartheta(\vartheta_\gamma = \theta, \varphi_\gamma), \varphi(\vartheta_\gamma = \theta, \varphi_\gamma)), \tag{5.26}$$

where the integral

$$\{\cos(\nu\phi_\gamma), \Psi^e_{nm}\}_{\gamma,\theta} = \int_{-\pi}^{\pi} \frac{\mathrm{d}\varphi_\gamma}{\pi} \cos(\nu\phi_\gamma) \Psi^e_{nm}(\vartheta(\vartheta_\gamma = \theta, \varphi_\gamma), \varphi(\vartheta_\gamma = \theta, \varphi_\gamma)) \tag{5.27}$$

denotes the Fourier cosine transform of the even eigenfunction Ψ^e_{nm} on the edge of the domain at latitude γ. Similarly, we find the Fourier coefficients of the normal velocity to the domain edge at latitude γ as

$$\left.\begin{aligned} \check{u}_{\vartheta_\gamma,\nu}[\gamma,\theta] &= \{\sin(\nu\varphi_\gamma), \boldsymbol{e}_{\vartheta_\gamma} \cdot (\nabla \times \boldsymbol{r}) \Psi\}_{\gamma,\theta} = -\{\boldsymbol{e}_{\vartheta_\gamma} \cdot (\nabla \times \boldsymbol{r}) \sin(\nu\varphi_\gamma), \Psi\}_{\gamma,\theta} \\ &= \frac{-\nu}{sin\theta} \{\cos(\nu\varphi_\gamma), \Psi\}_{\gamma,\theta} = - \sum_{nm} \nu \{\cos(\nu\varphi_\gamma), \Psi^e_{nm}\}_{\gamma,\theta} \frac{\langle \Psi^e_{nm} \Psi \rangle}{N_{nm} \sin\theta}, \\ &= \sum_{nm} \nu \{\cos(\nu\varphi_\gamma), \Psi^e_{nm}\}_{\gamma,\theta} (\Delta^{-1})_{nm,\tilde{n}\tilde{m}} \frac{\langle \Psi^e_{\tilde{n}\tilde{m}} \nabla_s \cdot \boldsymbol{\tau}_s \rangle}{\lambda_{\tilde{n}} N_{nm} \sin\theta}. \end{aligned}\right\} \tag{5.28}$$

We anticipate a surface torque density parallel to the edge of a second domain at the same longitude but different latitude $\tilde{\gamma}$ as

$$\boldsymbol{\tau}^e_s[\tilde{\gamma}, \theta] = \frac{\delta(\vartheta_{\tilde{\gamma}} - \theta) \boldsymbol{e}_{\varphi_{\tilde{\gamma}}}}{\pi R^2 \sin\theta} \sum_{\mu=1}^{\infty} \check{\tau}_\mu[\tilde{\gamma}, \theta] \sin(\mu\varphi_{\tilde{\gamma}}), \tag{5.29}$$

where the pre-factor is chosen such that the total torque on the second domain

$$|\boldsymbol{\tau}_{tot}| = \left| \int R^2 sin\vartheta_{\tilde{\gamma}} \, d\vartheta_{\tilde{\gamma}} \, \mathrm{d}\varphi_{\tilde{\gamma}} \boldsymbol{\tau}^e_s[\tilde{\gamma}, \theta] \right| = |\check{\tau}_1[\tilde{\gamma}, \theta]| \tag{5.30}$$

is given by the first Fourier coefficient $\check{\tau}_1[\tilde{\gamma}, \theta]$ of the second domain. We obtain

$$\left.\begin{aligned} \langle \Psi^e_{\tilde{n}\tilde{m}}, \nabla_s \cdot \boldsymbol{\tau}^e_s[\tilde{\gamma}, \theta] \rangle &= \int R^2 \sin\vartheta_{\tilde{\gamma}} \, \mathrm{d}\vartheta_{\tilde{\gamma}} \, \mathrm{d}\varphi_{\tilde{\gamma}} \Psi^{e*}_{\tilde{n}\tilde{m}} \frac{\boldsymbol{e}_{\varphi_{\tilde{\gamma}}}}{R \sin\theta} \cdot \frac{\partial \boldsymbol{\tau}^e_s[\tilde{\gamma}, \theta]}{\partial \varphi_{\tilde{\gamma}}} \\ &= \int \mathrm{d}\varphi_{\tilde{\gamma}} \Psi^{e*}_{\tilde{n}\tilde{m}} \sum_{\mu=1}^{\infty} \frac{\mu}{\pi R \sin\theta} \check{\tau}_\mu[\tilde{\gamma}, \theta] \cos(\mu\varphi_{\tilde{\gamma}}), \\ &= \frac{1}{R \sin\theta} \sum_{\mu=1}^{\infty} \mu \check{\tau}_\mu[\tilde{\gamma}, \theta] \{\Psi^e_{\tilde{n}\tilde{m}}, \cos(\mu\varphi_{\tilde{\gamma}})\}_{\tilde{\gamma},\theta}. \end{aligned}\right\} \tag{5.31}$$

Inserting (5.31) in (5.28) we find

$$\breve{u}_{\vartheta_\gamma,\nu}[\gamma,\theta] = \sum_{\mu} O_{\nu\mu}[\gamma,\theta;\tilde{\gamma},\theta]\breve{\tau}_{\mu}[\tilde{\gamma},\theta], \tag{5.32}$$

where

$$O_{\nu\mu}[\gamma,\theta;\tilde{\gamma},\theta] = \sum_{nm,\tilde{n}\tilde{m}} \frac{\nu\mu\{\cos(\nu\varphi_\gamma), \Psi^e_{nm}\}_{\gamma,\theta}(\Delta^{-1})_{nm,\tilde{n}\tilde{m}}\{\Psi^e_{\tilde{n}\tilde{m}}, \cos(\mu\varphi_{\tilde{\gamma}})\}_{\tilde{\gamma},\theta}}{R\sin^2\theta\lambda_{\tilde{n}}N_{nm}}. \tag{5.33}$$

The domain edge Oseen tensor $O_{\nu\mu}[\gamma,\theta;\tilde{\gamma},\theta]$ measures the response in the Fourier component of the normal velocity $\breve{u}_{\vartheta_\gamma,\nu}[\gamma,\theta]$ on the edge of the domain centred at latitude γ to the Fourier component of the torque $\breve{\tau}_{\mu}[\tilde{\gamma},\theta]$ on a different domain centred at latitude $\tilde{\gamma}$. Note that (5.32) requires the knowledge of the normal velocity field and torque density only at the edges of the domains. The normal velocities however are fixed via the specific mode of motion of the domains.

The computation of the single- and two-domain friction coefficients is now straightforward. We proceed with the computation of the single-domain friction first. Without loss of generality we may place the single domain at the north pole $\gamma = 0$. For this case the coordinates systems (ϑ,φ) and $(\vartheta_\gamma,\varphi_\gamma)$ coincide. We find

$$\{\cos(\nu\varphi_\gamma), \Psi_{nm}\}_{\gamma=0,\theta} = \omega R\delta_{nm}P^m_n(\cos\theta) \tag{5.34}$$

and

$$(\Delta)_{\tilde{n}\tilde{m},nm} = \delta_{\tilde{m}m}\Delta_{m,\tilde{n}n} \tag{5.35}$$

with

$$\Delta_{m,\tilde{n}n} = \left\{\delta_{\tilde{n}n} - \frac{\delta\lambda_n}{\lambda_{\tilde{n}}}\frac{\pi\omega^2R^4\int_{-1}^{1}\mathrm{d}x\ \mathrm{sign}(x-\cos\theta)P^m_{\tilde{n}}(x)P^m_n(x)}{N_{nm}}\right\}. \tag{5.36}$$

The Oseen tensor becomes diagonal in ν and μ. We require the domain to rotate with velocity $\boldsymbol{u} = \omega\boldsymbol{e}_y \times \boldsymbol{r}$ such that $\breve{u}_{\vartheta,1} = \omega R$ and $\breve{u}_{\vartheta,\nu} = 0$ for $\nu = 2, 3, \ldots$. This requires a torque $\breve{\tau}_1 = \omega R/O_{11}$, and $\breve{\tau}_\nu = 0$ for $\nu = 2, 3, \ldots$, with

$$O_{11}[0,\theta;0,\theta] = \sum_{n,\tilde{n}} \frac{\omega^2 R P^1_n(\cos\theta)(\Delta_1{}^{-1})_{n,\tilde{n}}P^1_{\tilde{n}}(\cos\theta)}{\sin^2\theta\lambda_{\tilde{n}}N_{n1}}. \tag{5.37}$$

For the case $\mathscr{H}_s = 0$ the inversion of Δ is trivial and we regain (3.9) by noting that

$$\frac{1}{f} = \eta_o R^3\sin\theta\frac{\omega}{|\breve{\tau}_1|} = \eta_o R^2\sin\theta O_{11}[0,\theta;0,\theta], \tag{5.38}$$

$$\mathscr{B} = \frac{\eta_s}{2\eta_o R\sin\theta} = \frac{\eta_s}{2\eta_o a} \tag{5.39}$$

is the Boussinesq number defined with the domain radius a. In the limit $\mathscr{B} \to \infty$ all terms except for $n = 1$ vanish in (5.37) and using (5.38) we find

$$\frac{1}{f}(\mathscr{B} \to \infty) = \sin\theta/8\pi, \tag{5.40}$$

which is the result for a rigid rotating sphere (Russel, Saville & Schowalter 1989) on the other hand small angles θ the sum in (5.37) converges only after summing over large numbers n. We may convert the sum into an integral and we might use the relation

$$\lim_{n\to\infty} n^{-m}P^m_n(\cos\vartheta) = \mathrm{J}_m(n\vartheta), \tag{5.41}$$

where $J_m(n\vartheta)$ is a Bessel function of order m. With these manipulations we rediscover the equation of De Koker (1996) for a flat membrane:

$$\frac{1}{f}(\mathscr{B}, \theta \to 0) = \frac{1}{2\pi}\int_0^\infty \mathrm{d}x \frac{J_1(x)^2}{x^2(1+\mathscr{B}x)} \overset{\mathscr{B}\to 0}{=} \frac{1}{2}\frac{4}{3\pi^2}. \tag{5.42}$$

Noting that the drag force is $F_{drag} = \check{\tau}_1/R$ and the domain velocity is $U_{Domain} = R\omega$ in a flat surface equation (5.42) predicts half of the result of De Koker (1996) for a flat monolayer domain having the same surface shear viscosity as the rest of the membrane. The factor 1/2 arises because we have a bilayer with water on both sides of the membrane. The theory of Hughes *et al.* (1981) for a rigid domain would be obtained for the case where one first performs the limit $\theta \to 0$ and afterwards the limit towards a solid domain $\mathscr{H}_s \to \infty$. The numerical inversion of the matrix Δ in (5.37) involves matrix elements with higher indices n and m that makes the evaluation more difficult the smaller the conical angle θ of the domain.

For the computation of the relative two-domain diffusion coefficient we consider the first domain to sit at the north pole and the second to sit at latitude γ . The latitude γ of the second domain must be larger than twice the conical angle of the domains $2\theta < \gamma < \pi$ for the domains not to overlap. For a relative motion of the domains we require the torques on one domain to be the inversion at the midpoint between both domains of the torque on the other domain: $\tau_{\varphi_0}[0,\theta](\varphi_0) = \tau_{\varphi_\gamma}[\gamma,\theta](\varphi_\gamma = \varphi_0 + \pi)$ which translates into

$$\check{\tau}_\mu[0,\theta] = (-1)^\mu \check{\tau}_\mu[\gamma,\theta]. \tag{5.43}$$

For a combined motion one finds $\check{\tau}_\mu[0,\theta] = (-1)^{\mu+1}\check{\tau}_\mu[\gamma,\theta]$. Here, we will derive the Oseen tensor for the relative motion. The velocity of the domain on the north pole occurs due to the torques from both domains and we find

$$\check{u}_{\vartheta,\nu}[0,\theta] = \sum_\mu \left(O_{\nu\mu}[0,\theta;0,\theta] + (-1)^\mu O_{\nu\mu}[0,\theta;\gamma,\theta]\right)\check{\tau}_\mu[0,\theta] = \sum_\mu O^{tot}_{\nu\mu}\check{\tau}_\mu[0,\theta], \tag{5.44}$$

where

$$O^{e,tot}_{\nu\mu} = \sum_{n,\tilde{n}\tilde{m}} \frac{\nu\mu\omega P_n^\nu(\cos\theta)(\Delta^{-1})_{n\nu,\tilde{n}\tilde{m}}[\omega R P^\mu_{\tilde{n}}(\cos\theta)\delta_{\tilde{m}\mu} + (-1)^\mu\{\Psi^e_{\tilde{n}\tilde{m}}, \cos(\mu\varphi_\gamma)\}]}{\sin^2\theta\lambda_{\tilde{n}}N_{n\nu}}. \tag{5.45}$$

The Oseen tensor for the odd solution is obtained by replacing $\{\Psi^e_{\tilde{n}\tilde{m}}, \cos(\mu\varphi_\gamma)\}$ with $\{\Psi^o_{\tilde{n}\tilde{m}}, \sin(\mu\varphi_\gamma)\}$ in (5.45):

$$O^{o,tot}_{\nu\mu} = \sum_{n,\tilde{n}\tilde{m}} \frac{\nu\mu\omega P_n^\nu(\cos\theta)(\Delta^{-1})_{n\nu,\tilde{n}\tilde{m}}[\omega R P^\mu_{\tilde{n}}(\cos\theta)\delta_{\tilde{m}\mu} + (-1)^\mu\{\Psi^o_{\tilde{n}\tilde{m}}, \sin(\mu\varphi_\gamma)\}]}{\sin^2\theta\lambda_{\tilde{n}}N_{n\nu}}. \tag{5.46}$$

The Oseen tensor for the combined motion of two domains is obtained by replacing the factor $(-1)^\mu$ by $(-1)^{\mu+1}$ in (5.45) and (5.46). If the contrast between the domain and embedding membrane surface shear viscosity vanishes equation simplifies to

$$O^{e,tot}_{\nu\mu} = \sum_n \frac{\nu\mu\omega P_n^\nu(\cos\theta)[\omega R P^\mu_n(\cos\theta)\delta_{\nu\mu} + (-1)^\mu\{\Psi^e_{n\nu}, \cos(\mu\varphi_\gamma)\}]}{\sin^2\theta\lambda_n N_{n\nu}}. \tag{5.47}$$

For the special case that the second domain sits at the south pole $\gamma=\pi$ we find $\vartheta=\pi-\vartheta_\pi$ and $\varphi=\pi-\varphi_\pi$. Therefore

$$\left.\begin{aligned}\{\cos(\mu\varphi_\pi),\Psi^e_{n\mu}\}_{\gamma=\pi,\theta}&=(-1)^\mu\omega R P^\mu_n(-\cos\theta)=(-1)^n\omega R P^\mu_n(\cos\theta),\\ \{\sin(\mu\varphi_\pi),\Psi^o_{n\mu}\}_{\gamma=\pi,\theta}&=-(-1)^\mu\omega R P^\mu_n(-\cos\theta)=-(-1)^n\omega R P^\mu_n(\cos\theta)\end{aligned}\right\} \tag{5.48}$$

and

$$\left.\begin{aligned}O^{e,tot}_{\nu\mu}[0,\theta;\pi,\theta]&=\sum_{n,\tilde n}\frac{(1+(-1)^{\tilde n-\mu})\omega^2 R\nu\mu P^\nu_n(\cos\theta)(\Delta^{-1}_\nu)_{n,\tilde n}P^\nu_{\tilde n}(\cos\theta)}{\sin^2\theta\lambda_{\tilde n}N_{n\nu}}\delta_{\nu\mu},\\ O^{o,tot}_{\nu\mu}[0,\theta;\pi,\theta]&=\sum_{n,\tilde n}\frac{(1-(-1)^{\tilde n-\mu})\omega^2 R\nu\mu P^\nu_n(\cos\theta)(\Delta^{-1}_\nu)_{n,\tilde n}P^\nu_{\tilde n}(\cos\theta)}{\sin^2\theta\lambda_{\tilde n}N_{n\nu}}\delta_{\nu\mu}\end{aligned}\right\} \tag{5.49}$$

with

$$\Delta_{\nu,\tilde n n}=\left\{\delta_{\tilde n n}-\frac{\delta\lambda_n}{\lambda_{\tilde n}}\frac{\pi\int_{-1}^1 \mathrm{d}x\,\mathrm{sign}(x^2-\cos^2\theta)P^\nu_{\tilde n}(x)P^\nu_n(x)}{N_{n\nu}}\right\}, \tag{5.50}$$

which in the case $\mathscr{H}_s=0$ simplifies to

$$\left.\begin{aligned}O^{e,tot}_{\nu\mu}[0,\theta;\pi,\theta](\mathscr{H}_s=0)&=\sum_n\frac{(1+(-1)^{n-\mu})\omega^2 R\nu\mu P^\nu_n(\cos\theta)^2}{\sin^2\theta\lambda_n N_{n\nu}}\delta_{\nu\mu},\\ O^{o,tot}_{\nu\mu}[0,\theta;\pi,\theta](\mathscr{H}_s=0)&=\sum_n\frac{(1-(-1)^{n-\mu})\omega^2 R\nu\mu P^\nu_n(\cos\theta)^2}{\sin^2\theta\lambda_n N_{n\nu}}\delta_{\nu\mu}.\end{aligned}\right\} \tag{5.51}$$

If both domains move relative to each other but perpendicular to their connecting geodesics then the domain at the north pole will rotate around the vesicle centre with velocity $\boldsymbol{u}_\perp=(\omega_{rel,\perp}/\sqrt{2})\boldsymbol{e}_x\times\boldsymbol{r}$ such that $\check u^e_{\perp,\theta,1}=(\omega_{rel,\perp}/\sqrt{2})R$ and $\check u^e_{\perp,\theta,\nu}=0$ for $\nu=\pm2,\pm3,\ldots$. Hence

$$\check\tau_{rel,\perp,1}=\sqrt{2}\check\tau_{\perp,1}[0,\theta]=\omega_{rel,\perp}(\boldsymbol{O}^{-1}_{e,tot})_{11}. \tag{5.52}$$

Similarly, for a relative motion parallel to the interconnecting geodesics the domain at the north pole will rotate around the vesicle centre with velocity $\boldsymbol{u}_\parallel=(\omega_{rel,\parallel}/\sqrt{2})\boldsymbol{e}_y\times\boldsymbol{r}$ such that $\check u^o_{\parallel,\theta,1}=(\omega_{rel,\parallel}/\sqrt{2})R$ and $\check u^o_{\parallel,\theta,\nu}=0$ for $\nu=\pm2,\pm3,\ldots$. Hence

$$\check\tau_{rel,\parallel,1}=\sqrt{2}\check\tau_{\parallel,1}[0,\theta]=\omega_{rel,\parallel}(\boldsymbol{O}^{-1}_{o,tot})_{11}. \tag{5.53}$$

The diffusion coefficient perpendicular to the geodesic connecting the domains is different than along the geodesic and we find

$$\left.\begin{aligned}\frac{1}{f_\parallel}&=\eta_o R^3\sin\theta\frac{\omega_{rel,\parallel}}{|\check\tau_{rel,\parallel,1}|}=\frac{\eta_o R^2\sin\theta}{\left|(\boldsymbol{O}^{-1}_{o,tot})_{11}\right|},\\ \frac{1}{f_\perp}&=\eta_o R^3\sin\theta\frac{\omega_{rel,\perp}}{|\check\tau_{rel,\perp,1}|}=\frac{\eta_o R^2\sin\theta}{\left|(\boldsymbol{O}^{-1}_{e,tot})_{11}\right|}.\end{aligned}\right\} \tag{5.54}$$

For $\mathscr{H}_s=0$ and $\gamma=\pi$, (5.54) simplifies, and using (5.51) we regain (4.10). In general several tasks outlined in the derivation in this section can only be performed numerically. When there is contrast in surface shear viscosities the integrals $\langle\Psi_{\tilde n\tilde m}\chi(\vartheta,\varphi)\Psi_{nm}\rangle$ must be computed. And the matrix Δ must be inverted numerically. In case of two-domain rheology and $\gamma\neq\pi$ one additionally has to numerically compute the integrals $\{\cos(\nu\varphi_\gamma),\Psi^e_{nm}\}_{\gamma,\theta}$ and $\{\sin(\nu\varphi_\gamma),\Psi^o_{nm}\}_{\gamma,\theta}$ and numerically must invert the Oseen tensor $\boldsymbol{O}_{tot}$. We will compute the effect of viscosity contrast for only

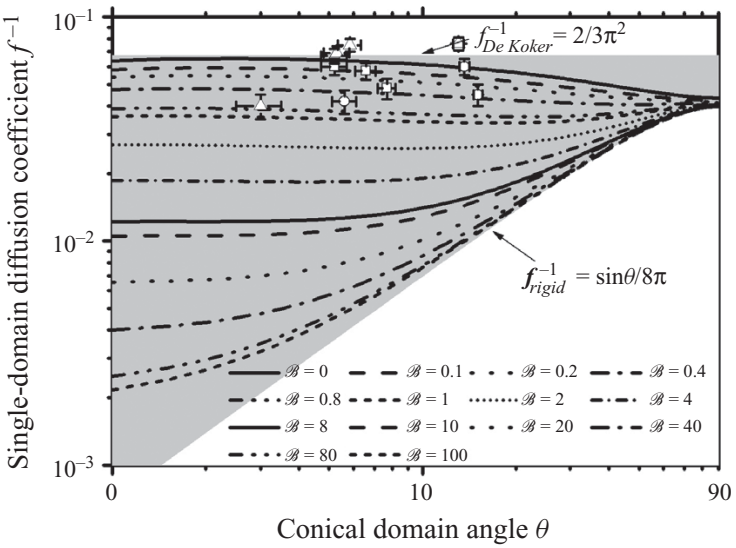

FIGURE 6. Dimensionless single-domain diffusion coefficient f^{-1} versus the conical domain angle θ for $\mathscr{H}_s = 0$ and different Boussinesq numbers $\mathscr{B} = 0$–100. The grey area extends over the region of possible single-domain diffusion coefficients where lower and upper boundary represent, respectively, the diffusion coefficient of a rigid sphere and a non viscous liquid disk in a non viscous flat membrane first derived by DeKoker equation (5.42). Experimental single-domain diffusion coefficients are incorporated in the figure for the compositions DOPC/DPPC/Chol = 16/64/20 (□), DOPC/DPPC/Chol = 40/40/20 (○), and DOPC/DPPC/Chol = 35/35/30 (△). All data falls into the regime of negligible surface shear viscosity ($\mathscr{B} < 1$).

one domain rheology. For the two-domain rheology the computation time would become quite long when considering arbitrary separations of the domains and a contrast in viscosity.

6. Single-domain rheology: results

In figure 6 we plot f^{-1}, i.e. the dimensionless single-domain diffusion coefficient versus the conical angle θ of the domain edge at different Boussinesq numbers for the case $\eta_o = \eta_i$ and $\eta_s^a = \eta_s^b$. The diffusion coefficient is very sensitive to the Boussinesq number for domains with small size. For large domains of size comparable to the radius of the vesicle, however, the variation of the diffusion coefficient with Boussinesq number is rather weak. Ultimately for large domains we rediscover (5.40) and the domain diffuses together with the entire vesicle, and the motion of the domain on the vesicle is locked to the rotation of the entire vesicle. The diffusion coefficient is bounded by the relation $2/3\pi^2 > f^{-1} > \sin\theta/8\pi$ within the grey region in figure 6 where the boundaries are given by the diffusion coefficient of De Koker (1996) corresponding to (5.42) and the rigid diffusion coefficient corresponding to (5.40). Experimental single-domain diffusion coefficients are incorporated in the figure for the compositions DOPC/DPPC/Chol = 16/64/20 (□), DOPC/DPPC/Chol = 40/40/20(○), and DOPC/DPPC/Chol = 35/35/30 (△) at a temperature of $T = 23°\mathrm{C}$. All data falls into the regime of negligible surface shear viscosity ($\mathscr{B} < 1$).

In figure 7 we plot the single-domain diffusion coefficient versus the Boussinesq number for the case $\eta_o = \eta_i$ and $\eta_s^a = \eta_s^b$. The diffusion first decreases with the Boussinesq number but levels off when $\mathscr{B} > R/a$, where the surface is so viscous that

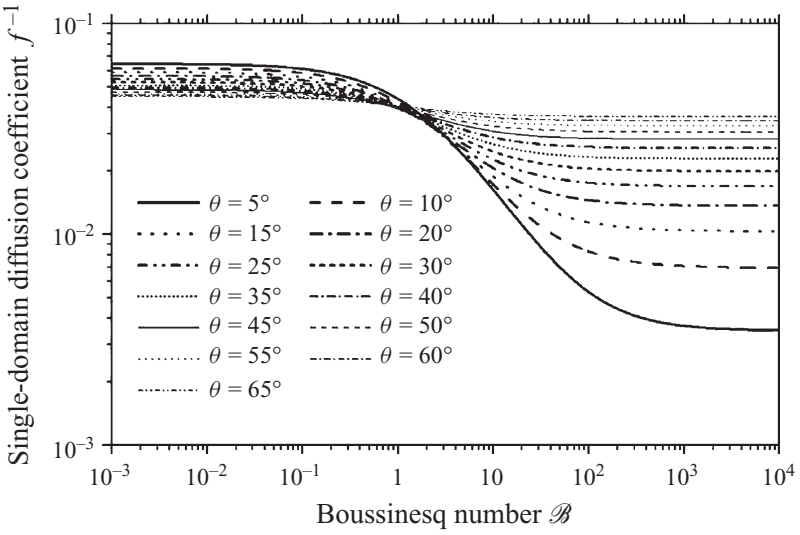

FIGURE 7. Dimensionless single-domain diffusion coefficient f^{-1} versus the Boussinesq number for $\mathscr{H}_s = 0$ and for different values of the conical domain angle θ.

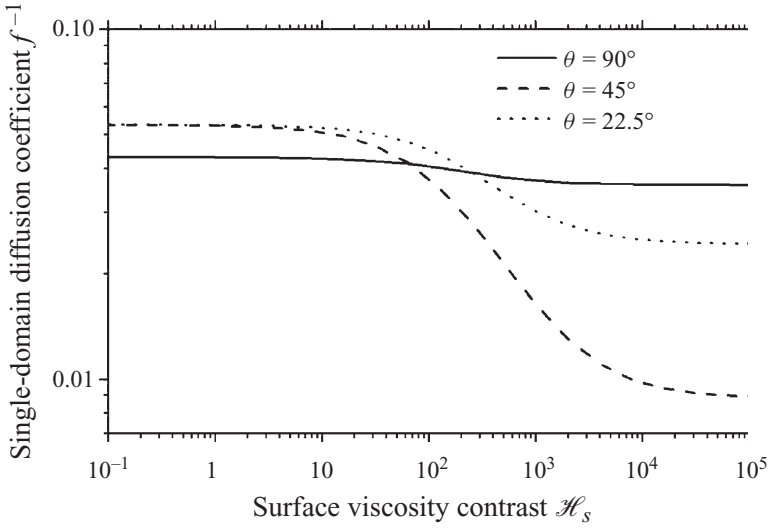

FIGURE 8. Dimensionless single-domain diffusion coefficient f^{-1} versus the surface shear viscosity contrast $\mathscr{H}_s$ for Boussinesq number $\mathscr{B} = 0.01$ (corresponding to fixed embedding membrane surface shear viscosity) and different conical domain angles θ.

it behaves like a rigid sphere with a diffusion coefficient given by (5.40) independent of the Boussinesq number. An increase of domain surface shear viscosity η_s^a at constant embedding membrane viscosity η_s^b results in higher friction and thus lowers the values of the diffusion constant. This can be seen in figure 8, where we plot the dimensionless single-domain diffusion coefficient at a fixed surface shear viscosity η_s^b of the embedding membrane against the surface shear viscosity contrast $\mathscr{H}_s$. When $\mathscr{B}\mathscr{H}_s \sin\theta \approx 1$ the diffusion coefficient decreases until it reaches a value $f^{-1}_{solid\ domain} \approx \sin\theta/8\pi$ that is lower than the diffusion coefficient of a liquid domain but higher than that of a rigid surface. The cross-over from a liquid interface to a partially rigid interface occurs when $\mathrm{Max}(\eta_s^a, \eta_s^b) \approx R\eta_o$. The change in diffusion constant is most pronounced for domains with intermediate size. Large domains diffuse mainly via rigid rotation of the vesicle already at very small surface shear

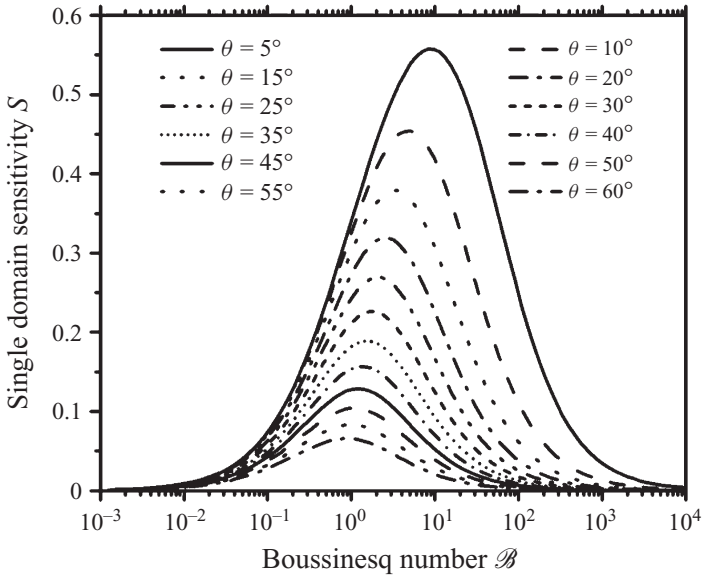

FIGURE 9. Sensitivity S of single-domain rheology versus Boussinesq number for different conical domain angles θ.

viscosity. An increase in surface shear viscosity in the domain therefore will not affect significantly the diffusion since it was already slow before the increase. For small domains, most of the vesicle remains at a low viscosity and their diffusion would not be affected by the high viscosity inside the small region of the domain. It is only for the domains of intermediate size that substantial reduction in diffusion is achieved by making the domain more viscous than the rest of the membrane. Intermediate size domains diffuse faster than a rigid vesicle at low viscosity and zero contrast. Increasing the surface shear viscosity of these domains makes a substantial fraction of the vesicle very viscous such that substantial decreasing of the diffusion occurs. Even a small domain when reaching a viscosity of $\eta_s^a \approx R\eta_o$ will start to feel the friction from the opposite site of the vesicle and will result in a decrease of diffusion coefficient substantially smaller than what is expected from a solid domain in a flat membrane. This shows that the order of the limits $\eta_s^a \to \infty$ and $R \to \infty$ may not be changed without obtaining different results. The basic result hence is that there is a cross-over from surface viscosity dominated friction towards finite size friction at roughly $\mathrm{Max}(\eta_s^a, \eta_s^b) \approx R\eta_o$. The cross-over from surface viscosity dominated friction towards finite size friction emerges in figure 9 as a peak in the sensitivity S versus $\mathscr{B}$ for the single-domain rheology. This peak is located in the regime $1 < \mathscr{B} < 1/\sin\theta$, while at low Boussinesq number ($\mathscr{B} < 1$) and at high Boussinesq number $\mathscr{B} > 1/\sin\theta$ the sensitivity is negligible. Moreover, the peak in sensitivity increases as the conical domain angle θ decreases. Since, at a fixed domain radius a and decreasing vesicle radius R the conical domain angle θ increases, we conclude that a confinement of domains to a small vesicle decreases the sensitivity and makes the measurement of the surface shear viscosity more difficult. In figure 6 the scattering of the experimental data that falls into the insensitive regime ($\mathscr{B} < 1$) is much larger than systematic variations of the surface shear viscosity with the structure of the phases.

7. Two-domain rheology: results

In § 4 we have shown that the relative diffusion of a domain measured with respect to a reference domain on the same vesicle depends on the separation between the

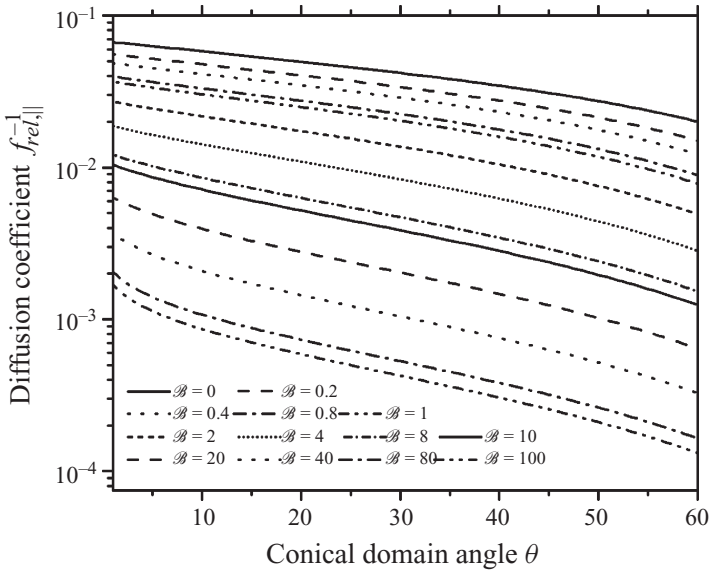

FIGURE 10. Dimensionless two-domain relative longitudinal diffusion coefficient $f_{rel,\|}^{-1}$ versus the conical domain angle θ for $\gamma = \pi$ and different Boussinesq numbers $\mathscr{B} = 0$–100.

domains and on the direction of the combined or relative motion. If one measures the relative motion between two domains then one must use a theory which describes the measured motion of one domain relative to the other domain. Choosing as reference domain one which is not infinitely separated from the domain of measurement has the draw back that the motions of the two domains are no longer uncorrelated. One disadvantage is that hydrodynamic interactions between the domains could give rise to a decrease of the relative diffusion of the domains as compared to the diffusion of single domains. The relative motion of both domains comes to a complete stop when both domains touch each other. To minimize the correlation between the two domains, one has to increase their separation, and the best situation will be when the two domains are located at opposite sides on the vesicle ($\gamma = \pi$), which significantly simplifies the mathematics of the relative diffusion. We therefore consider these hydrodynamic interactions for the case where one domain is located at exactly the opposite side of the vesicle than the reference domain. Figure 10 shows the relative longitudinal diffusion coefficient $f_{rel,\|}^{-1}$ as a function of the conical domain angle θ of the two domains for $\gamma = \pi$ and for different values of the Boussinesq number $\mathscr{B}$. Keeping the Boussinesq number fixed and changing the conical angle corresponds to decreasing the size of the vesicle at a fixed domain size and fixed rheological properties. While for a single domain the variation of the friction with the conical angle is weak, there is a pronounced dependence of the relative longitudinal domain diffusion coefficient on the conical angle. The larger the conical angle θ or the smaller the vesicle the more pronounced and the more correlated is the motion of the two domains. Relative motion of the domains becomes increasingly difficult and ultimately ceases when the vesicle is so small that both domains cover an entire hemisphere. At $\gamma = \pi$, a domain with conical angle of 30° exhibits the same relative diffusion coefficient than a small domain at a Boussinesq number that is one order of magnitude larger than that of the large domain.

Figure 11 shows the diffusion coefficient $f_{rel,\|}^{-1}$ as a function of the Boussinesq number $\mathscr{B}$. For $\mathscr{B} < 1$ the diffusion coefficient $f_{rel,\|}^{-1}$ is rather independent of the Boussinesq number and hence at $\mathscr{B} < 1$ the two-domain rheology is insusceptible to

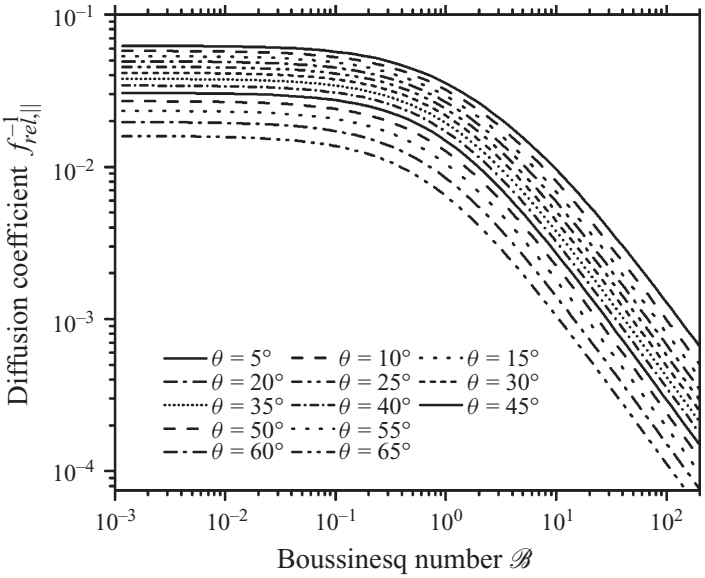

FIGURE 11. Dimensionless relative longitudinal diffusion coefficient $f_{rel,\parallel}^{-1}$ of two domains sitting at opposite sides of the vesicle versus the Boussinesq number for different conical domain angles θ. The diffusion coefficient shows a strong dependence on the Boussinesq number $\mathscr{B}$ for values $\mathscr{B} > 1$ making the relative longitudinal diffusion mode sensitive to $\mathscr{B}$.

the surface shear viscosity just as in the case of one domain rheology. At larger Boussinesq numbers the diffusion coefficient $f_{rel,\parallel}^{-1}$ of the longitudinal relative motion rapidly decreases with increasing Boussinesq number $\mathscr{B}$ and two-domain rheology becomes a sensitive rheological technique. Two-domain rheology is quite complex when considering domains separated by an arbitrary angle γ. We distinguish four modes of motion: 'combined' motion, where both domains move in the 'same direction along or perpendicular' to their interconnecting geodesic and 'relative' motion where both domains move in 'opposite directions'. It is important to note that 'relative' and 'combined' motion is a term that makes sense with respect to the interconnecting geodesic. If we consider the four modes and slowly separate the domains until they reach opposite sides of the vesicle, 'relative transversal' motion and 'combined longitudinal' motion become indistinguishable. The same is true for 'relative longitudinal' motion and 'combined transversal' motion. This can be seen in figure 12, where we plot the diffusion coefficient f^{-1} versus the domain separation γ for all four modes for a conical domain angle of $\theta = 30$ deg and for vanishing contrasts $\mathscr{H} = 0$ of the bulk and $\mathscr{H}_s = 0$ surface shear viscosities. All four modes have different diffusion coefficients. For all Boussinesq numbers $\mathscr{B}$ and all separations γ relative longitudinal diffusion has the lowest diffusion coefficient and combined longitudinal motion has the highest. The diffusion coefficient of relative motion decreases with decreasing separation angle γ. The diffusion coefficient of combined motion increases with decreasing separation angle.

Combined transversal motion and combined longitudinal motion are fairly similar at small separations. The reason for this becomes evident when considering a single domain of twice the area of the two domains. If both domains would fuse to one domain, combined transversal and combined longitudinal motion would merge to the single-domain diffusion constant of a domain with conical angle $\theta = 42.9°$. The values of those single-domain diffusion constants are shown at the left side of figure 12.

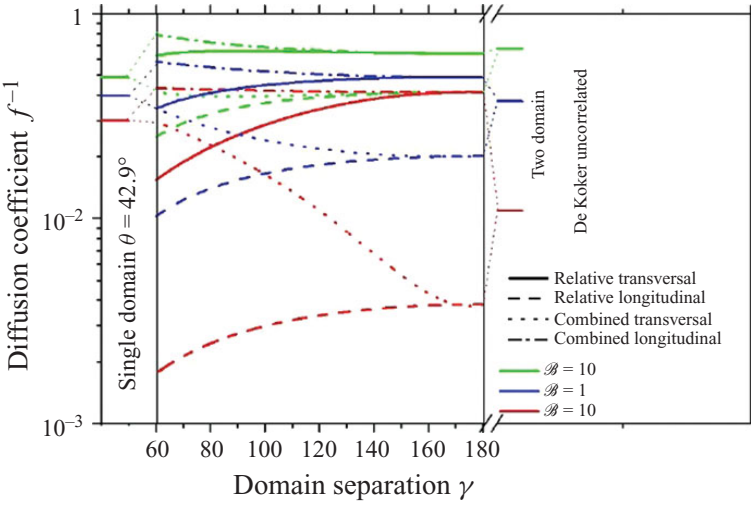

FIGURE 12. Dimensionless two-domain diffusion constants of all four modes of diffusion versus domain separation γ at three different Boussinesq numbers ($\mathscr{B} = 0, 1, 10$) and for a conical domain angle of both domains of $\theta = 30°$. To the left we show the corresponding single-domain diffusion constants of a single domain having the same area as the two domains. To the right we show the uncorrelated single-domain diffusion constant expected in a flat membrane. The splitting of the combined modes at low separation is a result of shape anisotropy. The splitting at maximum separation is a result of hydrodynamic correlations.

The splitting occurring between the combined modes at low separation is a result of the shape anisotropy of the two domains as compared to a single domain of similar area. Combined transversal and relative longitudinal motion become the same when both domains are separated by the maximal separation of $\gamma = \pi$. The mode reacting most sensitive to changes in the Boussinesq number $\mathscr{B}$ is the longitudinal relative diffusion. Combined transversal motion shows the strongest sensitivity to geometrical issues: While being rather insensitive to changes in Boussinesq number at small separations combined transversal motion becomes more and more sensitive to the Boussinesq number as the separation between both domains increases. Relative transversal motion just shows the opposite behaviour. At large separations relative transversal motion is slightly sensitive to changes in the Boussinesq number but its sensitivity become more accentuated when the domain separations become small. Both tendencies can be easily understood by considering that the transversal motions take on the character of longitudinal motions when the separation angle approaches $\gamma = \pi$. The difference in diffusion coefficients $f^{-1}_{rel,\parallel} = f^{-1}_{comb,\perp}$ and $f^{-1}_{rel,\perp} = f^{-1}_{comb,\parallel}$ at $\gamma = \pi$ shows that both domains are still correlated when being separated at maximum distance. For a comparison we show the diffusion coefficient $f^{-1}_{De\ Koker}$ corresponding to (5.42) that is expected in a flat membrane for infinite separation of the domains. The splitting of the two pairs of modes is therefore *a* measure of the hydrodynamic correlations persisting in a vesicle. The splitting between both diffusion coefficients is minimal for small domains and low Boussinesq number. The splitting increases when having larger domains or higher Boussinesq numbers. In the range $\mathscr{B} > 1/\sin\theta$, i.e. the range where single-domain rheology is insensitive to the Boussinesq number, the longitudinal relative diffusion is sensitive to the Boussinesq number. However the longitudinal relative diffusion is strongly correlated in this regime. Separation of the motion of two domains into the proper modes in a two-domain rheology is important due to the different behaviour of these modes.

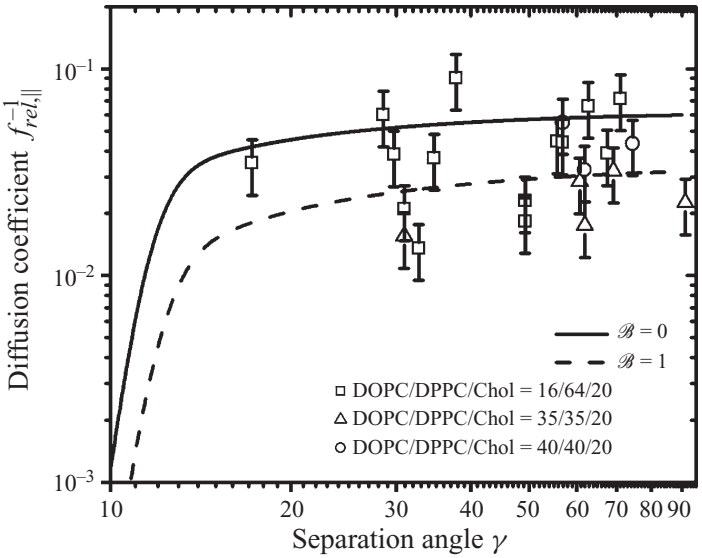

FIGURE 13. Experimental relative longitudinal diffusion coefficient of domains $f_{rel,||}^{-1}$ versus the domain separation γ for a conical domain angle of $\theta \approx 5 \pm 1$ deg for the compositions DOPC/DPPC/Chol = 16/64/20 (□), DOPC/DPPC/Chol = 40/40/20 (○), and DOPC/DPPC/Chol = 35/35/30 (△). Two theoretical curves with $\mathscr{B} = 0$ and $\mathscr{B} = 1$ are incorporated for vanishing contrast $\mathscr{H} = 0$ of the bulk and $\mathscr{H}_s = 0$ surface shear viscosities. The average experimental two-domain data suggest that the single-domain data are correct and that surface viscous effects are negligible ($\mathscr{B} < 1$).

Experimental two-domain diffusion data will usually be collected at varying separations γ. In figure 13 we depict the experimental relative longitudinal diffusion coefficient of domains $f_{rel,||}^{-1}$ versus the domain separation γ for a conical domain angle of $\theta \approx 5^\circ \pm 1^\circ$ for the compositions DOPC/DPPC/Chol = 16/64/20 (□), DOPC/DPPC/Chol = 40/40/20(○), and DOPC/DPPC/Chol = 35/35/30 (△). Two theoretical curves with $\mathscr{B} = 0$ and $\mathscr{B} = 1$ are incorporated for vanishing contrast $\mathscr{H} = 0$ of the bulk and $\mathscr{H}_s = 0$ surface shear viscosities. Although the scatter of the data is large the average experimental two-domain data suggest that the single-domain data are correct and supports the idea that $\mathscr{B} < \infty$. Surface viscous effects are negligible ($\mathscr{B} < 1$) for the mixtures and surface shear viscosities in all phases are lower than $\eta_s < 10^{-9}\,\mathrm{Ns\,m^{-1}}$. The scatter of the experimental data is more pronounced as in single-domain rheology.

In contrast to single-domain rheology, two-domain rheology, specifically the longitudinal relative diffusion becomes increasingly sensitive to the Boussinesq number at high Boussinesq numbers. One might think that this would enable measurement of high surface shear viscosities of the vesicle membrane using two-domain rheology. However, in practice a vesicle of high viscosity will have a solid rotational diffusion constant that is larger than the relative diffusion time by a factor given by the Boussinesq number $\mathscr{B}$. The two domains in the field of view of the microscope will leave the field of view of the microscope with a rate defined by the solid rotational diffusion constant. The typical change in separation of the two domains during that limited time is of the order $R\sqrt{\Delta\gamma^2} = \mathscr{B}^{-1/2}R$. Two domains of size 5 μm on opposite sides on a vesicle of typical size $R = 20\,\mu\mathrm{m}$, and surface shear viscosity $\eta_s = 10^{-6}\,\mathrm{Ns\ m^{-1}}$ will change their separation by 1 μm during the time available for the observation. Similar domains separated by less than the maximal separation will diffuse apart by less than 1 μm. Optical microscopy of resolution 1 micron

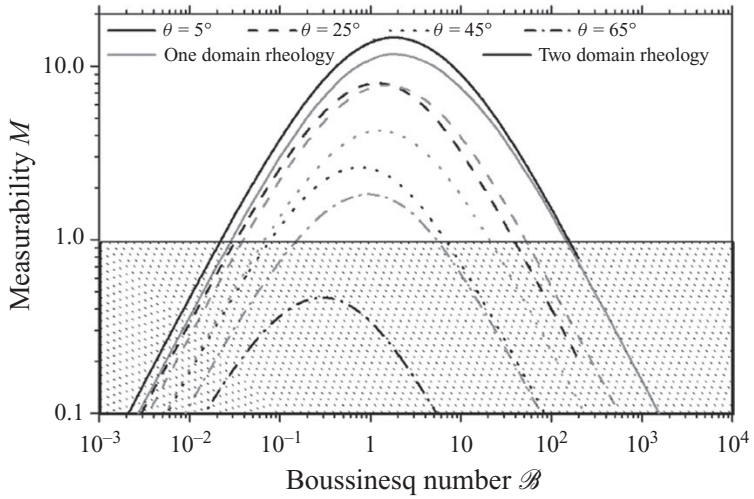

FIGURE 14. Measurability M of one domain rheology (grey) and of the relative longitudinal diffusion mode for two domains sitting at opposite sides of the vesicle (black) versus Boussinesq number $\mathscr{B}$ for different conical domain angles θ. The shaded region indicates the region non accessible by the experiments.

will therefore be useful for measurements of shear surface viscosities that are less than $\eta_s < 10^{-6}\,\mathrm{Ns\,m^{-1}}$. In single-domain rheology, one does not have these resolution requirements. A rheological technique capable of measuring the surface shear viscosity must have both high resolution and high sensitivity. In figure 14 we therefore plot the measurability M, (3.12) versus the Boussinesq number $\mathscr{B}$ for both one domain and two-domain rheology. In the plot we assume a value of $R^2/\Delta x_{min}^2 = 10^3$. At similar conical domain angles θ, the measurability of one domain rheology is about a factor of 1–10 larger than for two-domain rheology. If one wishes to measure the surface shear viscosity, the one-domain rheology is superior to two-domain rheology. Two-domain rheology on the other hand has the advantage of producing a more local measurement of the surface shear viscosity, at the price of lower measurability. The variation of the measurability with the Boussinesq number $\mathscr{B}$ and the conical domain angle θ is rather similar for both techniques. Both techniques allow the measurement of surface shear viscosities in a regime $1 < \mathscr{B} < 1/\sin\theta$. Outside this regime measurements of the surface shear viscosity should not be trusted. All diffusion data aquired for the different mixtures in this paper fall into a range where only upper bounds for the surface shear viscosity can be given.

It is obvious what to expect when using multi-domain rheology. Most likely the measurability will suffer further decrease as the number of domains used for the measurement is increased. Multi-domain rheology might however give a more local measure of the surface shear viscosity and will be also mathematically more complex. Tracking the motion of more domains on a vesicle hence will not improve the problems occurring in the measurement of high surface shear viscosities. One way to overcome the low measurability at high surface shear viscosities might be to look at the coarsening kinetics of the domains. The vesicle can lower its domain line tension energy via the coalescence of domains. At high surface shear viscosities the coalescence of domains most likely will become diffusion limited. Observing the statistics of coarsening as a function of time will not require following the positions of individual domains such that the time of observation is no longer limited by the rotational relaxation time $\Delta t_{max} < D_{rot}^{-1}$. Hence the high sensitivity of

relative longitudinal diffusion together with a higher resolution achieved via long time measurements will lead to a high measurability.

8. Discussion

Diffusion of domains within cell membranes is a difficult hydrodynamic problem. Solutions to this problem must take into account the geometric constraints and the mechanical and rheological properties of the constituents. Let us discuss the effects of geometry first. We approximated the geometric shape of a vesicle by a sphere and the domain as a circular segment which adheres to the sphere. Such approximation holds if the viscous stresses at the vesicle membrane and at the domain edge are small compared to the vesicle tension and the domain edge line tension. Fluorescence microscopy images of vesicles containing ternary mixtures of lipids and cholesterol (Veatch & Keller 2003; Cicuta *et al.* 2007) show that the shapes of vesicles and domain edges can be spherical and circular, respectively. Based on this experimental evidence, we neglect fluctuations of the shapes due to finite interfacial and line tension. Our analysis of course does not apply close to the miscibility critical point, where domain shapes undergo significant fluctuations and where the line tension between the phases approaches to zero (Baumgart, Hess & Webb 2003). It also does not apply when the bending rigidities of the domains are different from the bending rigidities of the rest of the membrane such that domains bulge into the exterior liquid (Honerkamp-Smith *et al.* 2008). We have shown that the single-domain rotational diffusion experimentally observed in video microscopy of a domain on a vesicle is due to the diffusion of the domain within the vesicle if the surface shear viscosity is small $\eta_s \ll \eta R$. In vesicles of typical size of 20 μm residing in an aqueous environment ($\eta \approx 10^{-3}\,\mathrm{Ns\,m^{-2}}$) this means that only if $\eta_s \ll 2\times10^{-8}\,\mathrm{Ns\,m^{-1}}$ the domain can diffuse within the vesicle. Our upper limit for the apparent single-domain translational diffusion constant is given by De Koker's result $D_{trans} < D_{trans}^{DeKoker} = 2k_BT/3\pi^2\eta_o a$. For large surface shear viscosities $\eta_s >> 2\times10^{-8}\,\mathrm{Ns\,m^{-1}}$ the diffusion of the domain will no longer be dominated by diffusion within the membrane but by the solid rotational diffusion of the rigid vesicle as a whole. The apparent translational diffusion coefficient associated with such rigid rotational diffusion is $D_{trans}^{rigid} = k_BT/8\pi\eta_o R$. For a vesicle with radius 20 μm in water the apparent single-domain translational diffusion coefficient of a domain in a rigid vesicle is $D_{trans}^{rigid} = 10^{-2}\,\mu\mathrm{m^2\,s^{-1}}$. We have shown that the most reliable way of measuring surface shear viscosities on vesicles with domain tracking is to use single-domain rheology. In recent experiments of Cicuta *et al.* (2007) measurements of the surface shear viscosity of vesicular membranes are reported using multi-domain rheology. Cicuta *et al.* (2007) try to avoid the loss of sensitivity of single-domain rheology at high Boussinesq numbers by subtracting average diffusion to yield unbiased domain motion. No details are given how such average motion is subtracted. On a curved surface, velocities of different domains are lying in different tangent spaces to the different domains and therefore cannot be subtracted directly since such relative velocities would have components moving the domain out of the interface. Measurements of relative velocities in curved space are far from trivial. The proper way to obtain relative velocities has been outlined in (4.1)–(4.5) and corresponds to subtracting velocities of the reference domain only after parallel transport (Misner *et al.* 1973) along the geodesic connecting the reference domain to the domain of measurement. An analysis where one subtracts velocities from several reference domains, of course is a form of multi-domain rheology that cannot be interpreted correctly using single-domain rheological equations such as those of

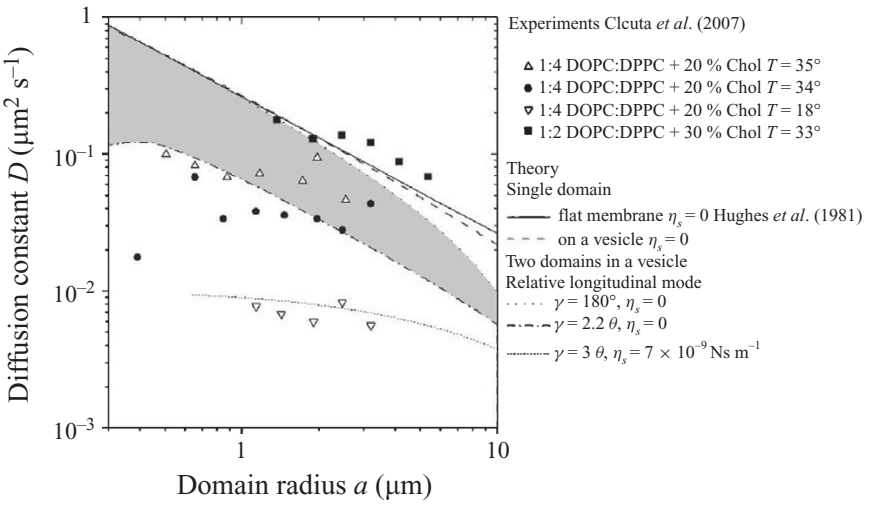

FIGURE 15. Comparison of single-domain and relative longitudinal translational diffusion with experimental data from Cicuta *et al.* (2007) for a vesicle of radius $R = 20\,\mu m$, bulk viscosity of $\eta = 10^{-3}\,Ns\,m^{-2}$, temperature $T = 300\,K$, and vanishing bulk and surface viscosity contrasts $\mathscr{H} = \mathscr{H}_s = 0$. The grey region indicates the regime where relative longitudinal diffusion can be explained by different separations γ of the domains without the need of a surface shear viscosity. Below the grey area the surface shear viscosity becomes measurable and we show a fit (short dotted line) with $\gamma = 3\theta$ and $\eta_s = 7 \times 10^{-9}\,Ns\,m^{-1}$ to the 1:4 DOPC:DPPC + 20 % cholesterol data at $T = 18°C$. Experimental data above the grey area most likely contain contributions from the other three two-domain diffusion modes. The solid and dashed line shows the theoretical predictions for a single domain in a flat membrane and on a vesicle.

Saffmann & Delbrück (1975) or such as those of Hughes *et al.* (1981). No distinction of modes has been made by Cicuta *et al.* (2007) when analysing their data. However, we might expect that subtracting average velocities will largely eliminate contributions from the three modes that contain solid rotations of the entire vesicle. One might hope that their measurements will catch the motion of the relative longitudinal mode to the neighbouring domain lying along the direction of momentary motion. Fluorescence images of the vesicles investigated by Cicuta *et al.* (2007) suggest that the density of domains is quite high such that there are always neighbouring domains in the way of motion. In figure 15 we plot the single-domain and relative longitudinal two-domain translational diffusion constants versus domain size a for a vesicle of radius $R = 20\,\mu m$ under several different geometrical situations. The single-domain translational diffusion constant $D_{Hughes} = k_B T/16\,\eta a$ for non viscous flat membrane and the single-domain translational diffusion constant on a vesicle $D_{single}^{vesicle}$ have the largest diffusion constant. The relative longitudinal two-domain translational diffusion constant in a non-viscous vesicle at maximum separation of both domains is almost a factor of two smaller than the single-domain diffusion. All experimental two-domain rheology data having properly subtracted relative motion between the two domains should lie below this line. We incorporate experimental data from Cicuta *et al.* (2007) into our graph and some of these data (the 1:2 DOPC:DPPC + 30 % cholesterol mixture at $T = 33°C$) lie above this line indicating that subtracting the motion of more than one reference domain might not properly project onto the relative longitudinal mode of two domains. Relative longitudinal diffusion depends on the separation of the two domains. In figure 15 we have plotted the largest possible value of relative longitudinal translational diffusion occurring for a separation of $\gamma = \pi$ and vanishing surface shear viscosity $\eta_s = 0$. Additionally, we plot the lowest relative longitudinal

translational diffusion constant possible for zero surface shear viscosity $\eta_s = 0$ if one discards domains that are too close $\gamma < 2.2\theta$. The grey region between this two lines hence is a region where experimentally observed diffusion constants may be explained by pure geometry without any surface shear viscosity $\eta_s = 0$. Most of the data of Cicuta *et al.* (2007) falls into this regime. The translational diffusion constants of the 1:4 DOPC:DPPC + 20 % cholesterol mixture at $T = 35°C$ can be explained equally well with $\eta_s = 0$ and $\gamma = 5\theta$ as with $\eta_s = 3 \times 10^{-9}\,\mathrm{Ns\,m^{-1}}$ and $\gamma = \pi$. Experimental data falling below the grey region cannot be explained with vanishing surface shear viscosity. Cicuta *et al.* (2007) data for the 1:4 DOPC/DPPC mixture with 20 % cholesterol at 18°C and 34°C falls below the grey region. In our measurements the slowest mode of diffusion is the longitudinal relative diffusion. We could not confirm the experimental values measured by Cicuta *et al.* (2007). In order to get a figure of merit about the surface shear viscosity their data would imply we fitted the data of Cicuta *et al.* (2007) assuming a separation between the domains of $\gamma \approx 3\theta$ that approximately corresponds to the fluorescence images presented with their data.

We found that their data for the 1:4 DOPC/DPPC mixture with 20 % cholesterol at 18°C is well fitted with the relative longitudinal mode when using a viscosity of $\eta_s = 7 \times 10^{-9}\,\mathrm{Ns\,m^{-1}}$. This viscosity is almost three orders of magnitude smaller than when fitting the same data with Saffmann & Delbrück (1975) ($\eta_s = 4 \times 10^{-6}\,\mathrm{Ns\,m^{-1}}$) showing that hydrodynamic interactions between domains cannot be neglected. Translational diffusion constants of lipids in mixtures of phospholipids and cholesterol measured with fluorescence correlation spectroscopy (Kahya & Schwille 2006) and diffusion nuclear magnetic resonance (NMR) (Filippov, Orädd & Lindblom 2004) report values of $0.1 \times 10^{-8}\,\mathrm{cm^2\,s^{-1}} < D_{lipid} < 20 \times 10^{-8}\,\mathrm{cm^2\,s^{-1}}$. If we assume that those lipids diffuse as individuals without forming larger complexes, neglect the non-continuous structure of the membrane on the molecular scale, we may fit those single-lipid translational diffusion constants using Saffmann & Delbrück (1975). We assume a hydrodynamic membrane radius of the lipid is of the order of 5 Å. Under these circumstances the lipid diffusion constants correspond to surface viscosities of $3 \times 10^{-8}\,\mathrm{Ns\,m^{-1}} > \eta_s > 1 \times 10^{-10}\,\mathrm{Ns\,m^{-1}}$, which is consistent with our experimental data and with our interpretation of the domain diffusion but inconsistent with using Saffmann & Delbrück (1975) for the domain diffusion and inconsistent with the experimental data of Cicuta *et al.* (2007). If the lipids do not diffuse as individuals but in the form of larger complexes, the surface shear viscosity extracted from the lipid diffusion data will be somewhat lower than when assuming individual diffusion. Moreover our value of the surface shear viscosity corresponds to a Boussinesq number slightly smaller than unity $\mathscr{B} \approx 1$, which is just below the regime of good measurability of the technique. The lever rule states that properties like the surface shear viscosity of the coexisting phases should not vary with the area fraction each phase occupies. The data of Cicuta *et al.* (2007) varies with the area fraction and violates the lever rule. In our measurements surface shear viscosities are negligible and there is no violation of the lever rule.

Our experimental data, our analysis of the data and our interpretation of the experiments therefore differ from Cicuta *et al.* (2007). Diffusion constants of the slowest mode are larger than diffusion constants of Cicuta *et al.* (2007). Most of the reduction in diffusion constant on the vesicle is an effect of a decreasing separation γ of the domains. The diffusion is mainly affected by the hydrodynamic interactions mediated primarily via the bulk fluid, and surface shear viscosity of the membranous phases are at least three orders of magnitude smaller than anticipated by Cicuta *et al.* (2007).

So far, we have neglected the contrast in surface shear viscosity in our discussion. In the limit of vanishing surface shear viscosity the diffusion constant of a liquid domain is larger by a factor of $32/3\pi^2 = 1.08$ than that of a solid domain. Deviations of the result of De Koker (1996) from the results of Hughes *et al.* (1981) are limited to 15 % over the entire range of surface shear viscosities. The curvature of the vesicle does not change these effects if one discards the domains of intermediate size. Hence the approximation to use the same surface shear viscosity for the domain and the majority phase of the membrane for vesicular phases of small surface shear viscosity is believed to lead to errors not exceeding 15 %. Given the uncertainties in conditions in the experimental data these deviations from (3.9) appear to be of minor impact to the numerical values extracted from the data. The theory derived here is for one and two domains diffusing in a homogeneous membrane. In experiments there usually are several domains on a vesicle. We might consider the suspension of domains in the vesicle as an effective medium with an effective surface shear viscosity. However, once one of the surface shear viscosities results in a viscous length scale of the order of the typical geometric extensions of the system, the diffusing domain will sense and react in its diffusion to all geometrical details within that range. Our measurements (not shown) indicate that the presence of other domains suppresses relative transversal diffusion in a way, such that relative transversal diffusion becomes comparably slow to relative longitudinal diffusion. This in turn might be used to detect length scales of the S_0 phase domains in the three phase coexistence region S_0, L_α, L_0. Great care needs to be taken if one wants to extract rheological properties of one of the constituents of such a system.

9. Conclusions

Single-domain rheology and two-domain rheology on a vesicle are two ways to measure the surface shear viscosity of membranes in a vesicle. The ratio of surface to bulk viscosities defines a viscous length scale. Only when the viscous length scale falls between the size of the domain and the size of the vesicles, can a surface shear viscosity be measured easily. To achieve a high measurability of the surface shear viscosity the diffusion must be sensitive to the surface viscosity and must be resolved. We demonstrate that the best domain-tracking method to resolve the surface shear viscosity is the single-domain rheology. Different modes of diffusion in two- or multi-domain rheology have different sensitivity and resolution. A domain rheology measurement should decompose the motion of the domains into normal modes of diffusion. The decomposition is important because hydrodynamic interactions between domains confined to the same vesicle reduce the relative longitudinal diffusion constant stronger than the other modes of diffusion. This makes the relative longitudinal mode more sensitive to the surface shear viscosity than other modes of diffusion. The gain in sensitivity is achieved by a loss of resolution and does not increase the range where surface shear viscosities can be measured. Our experiments on vesicle do not confirm the diffusion constants measured in experiments of Cicuta *et al.* (2007). Our interpretation suggests that the observed reduction in diffusion constants is mainly due to hydrodynamic interactions mediated by the water and only a minor contribution is due to the viscous membrane. Our experimental diffusion constants correspond to surface shear viscosities that differ by at least three orders of magnitude from those extracted by Cicuta *et al.* (2007). The diffusion of domains in vesicles depends on all geometrical details in the surrounding of the domain that are within the range of the viscous length scale. Thus our work will help and inspire experiments on the diffusion of domains on spherical surfaces.

We thank H. Brand for useful discussion, W. Reichstein and J. Köhler for help with the vesicle preparation. P. T. was supported by the program 'Juan de la Cierva' (JCI-2009-04192). P. D. and T. M. F. acknowledge support by the National Science Foundation under CHE-0649427. T. M. F. and Z. K. acknowledge support by the German Science Foundation under Fi548/10-1/11-1 and the Jordanian Higher Council for Science and Technology.

REFERENCES

Angelova, M. I., Soléau, S., Méléard, Ph., Faucon, J. F. & Bothorel, P. 1992 Preparation of giant vesicles by external AC electric-fields – kinetics and applications. *Program. Colloid Polym. Sci.* **89**, 127–131.

Bagatolli, L. A. & Gratton, E. 2000 Two photon fluorescence microscopy of coexisting lipid domains in giant unilamellar vesicles of binary phospholipid mixtures. *Biophys. J.* **78**, 290–305.

Baumgart, T., Hess, S. T. & Webb, W. W. 2003 Imaging coexisting fluid domains in biomembrane models coupling curvature and line tension. *Nature* **425**, 821–824.

Beattie, M. E., Veatch, S. L., Stottrup, B. L. & Keller, S. L. 2005 Sterol structure determines miscibility versus melting transitions in lipid vesicles. *Biophys. J.* **89**, 1760–1768.

Berne, B. J. & Precora, R. 2000 *Dynamic Light Scattering with Applications to Chemistry, Biology and Physics*. Dover.

Brown, D. A. & London, E. 1998 Functions of lipid rafts in biological membranes. *Annu. Rev. Cell Devel. Biol.* **14**, 111–136.

Cicuta, P., Keller, S. L. & Veatch, S. L. 2007 Diffusion of liquid domains in lipid bilayer membranes. *J. Phys. Chem.* B **111**, 3328–3331.

Daniels, D. R. & Turner, M. S. 2002 Diffusion on membrane tubes: a highly discriminatory test of the Saffman–Delbrück theory. *Langmuir* **23**, 6667–6670.

Danov, K., Dimova, R. & Pouligny, B. 2000 Viscous drag of a solid sphere straddling a spherical or flat surface. *Phys. Fluids* **12**, 2711–2722.

De Koker, R. 1996 Domain structures and hydrodynamics in lipid monolayers. PhD dissertation, Stanford University.

Dimova, R., Dietrich, C., Hadjiisky, A., Danov, K. & Pouligny, B. 1999*a* Falling ball viscosimetry of giant vesicle membranes: finite-size effects. *Eur. Phys. J.* B **12**, 589–598.

Dimova, R., Dietrich, C. & Pouligny, B. 1999*b* Motion of particles attached to giant vesicles: falling ball viscosimetry and elasticity measurements on lipid membranes. In *Giant Vesicles* (ed. P. Walde & P. Luisi), chap. 15, p. 221. John Willey & Sons.

Edwards, D. A., Brenner, H. & Wasan, D. T. 1991 Interfacial transport and rheology. *Butterworth–Heinemann Ser. Chem. Engng Boston*, pp. 104–111.

Engelman, D. M. 2005 Membranes are more mosaic than fluid. *Nature* **438**, 578–580.

Fischer, Th. M. 2003 The drag on needles moving in a Langmuir monolayer. *J. Fluid Mech.* **498**, 123–137.

Fischer, T. M., Dhar, P. & Heinig, P. 2006 The viscous drag of spheres and filaments moving in membranes or monolayers. *J. Fluid. Mech.* **558**, 451–475.

Fischer, T. M. & Lösche, M. 2004 Pattern formation in Langmuir monolayers due to long range electrostatic interactions. In *Lecture Notes in Physics, Molecules in Interaction with Surfaces and Interfaces* (ed. R. Haberlandt, D. Michel, A. Pöppl & R. Stannarius), vol. 634, pp. 383–394. Springer.

Filippov, A., Orädd, G. & Lindblom, G. 2004 Lipid lateral diffusion in ordered and disordered phases in raft mixtures. *Biophys. J.* **86**, 891–896.

Gaus, K., Gratton, E., Kable, E. P. W., Jones, A. S., Gelissen, I., Kritharides, L. & Jessup, W. 2003 Visualizing lipid structure and raft domains in living cells with two-photon microscopy. *Proc. Nat. Acad. Sci.* **100**, 15554–15559.

Heinig, P., Wurlitzer, S., John, t. & Fischer, Th. M. 2002 Stability criterion for three phase intersection points in monolayers. *J. Phys. Chem.* B **106**, 11951–11960.

Honerkamp-Smith, A. R., Cicuta, P., Collins, M. D., Veatch, S. L., den Nijs, M., Schick, M. & Keller, S. L. 2008 Line tensions, correlation lengths and critical exponents in lipid membranes near critical points. *Biophys. J.* **95**, 236–246.

Hughes, B. D., Pailthorpe, B. A. & White, L. R. 1981 The translational and rotational drag on a cylinder moving in a membrane. *J. Fluid Mech.* **110**, 349–372.

Kahya, N. & Schwille, P. 2006 How phospholipid-cholesterol interactions modulate lipid lateral diffusion, as revealed by fluorescence correlation spectroscopy. *J. Fluoresc.* **16**, 671–678.

Khattari, Z., Heinig, P., Wurlitzer, S., Steffen, P., Lösche, M. & Fischer, Th. M. 2002 Wetting in asymmetric quasi-2d-systems. *Langmuir* **18**, 2273–2279.

Klingler, J. F. & McConnell, H. 1993 Brownian-motion and fluid-mechanis of lipid monolayer domains. *J. Phys. Chem.* **97**, 6096–6100.

Korlach, J., Schwille, P., Webb, W. W. & Feigenson, G. W. 1999 Characterization of lipid bilayer phases by confocal microscopy and fluorescence correlation spectroscopy. *Proc. Nat. Acad. Sci.* **96**, 8461–8466.

Kubo, R. 1957 Statistical-mechanical theory of irreversible processes 1. General theory and simple applications to magnetic and conduction problems. *J. Phys. Soc. Japan* **12**, 570–586.

Levine, A. J. & MacKintosh, F. C. 2002 Dynamics of viscoelastic membranes. *Phys. Rev.* E **66**, 061606.

Misner, C. W., Thorne, K. P. & Wheeler, J. A. 1973 *Gravitation.* W. H. Freeman and Company.

Mukherjee, S. & Maxfield, F. R. 2000 Role of membrane organization and membrane domains in endocytic lipid trafficking. *Traffic* **1**, 203–211.

Naji, A., Levine, A. J. & Pincus, P. A. 2007 Corrections to the Saffman–Delbrück mobility for membrane bound proteins. *Biophys. J.* **93**, L49–L51.

Peters, R. & Cherry, R. J. 1982 Lateral and rotational diffusion of bacteriorhodopsin in lipid bilayers: experimental test of Saffman–Delbrck equations. *Proc. Nat. Acad. Sci. USA* **79**, 4317–4321.

Petrov, E. P. & Schwille, P. 2008 Translational diffusion in lipid membranes beyond the Saffman–Delbrück approximation. *Biophys. J.* **94**, L41–L43.

Prasad, V., Koehler, S. A. & Weeks, E. R. 2006 Two-particle microrheology of quasi-2D viscous systems. *Phys. Rev. Lett.* **97**, 176001–176004.

Radhakrishnan, H. A. & McConnell, H. M. 1999 Cholesterol-phospholipid complexes in membranes. *J. Am. Chem. Soc.* **121**, 486–487.

Reichl, L. E. 1980 *A Modern Course in Statistical Physics.* Edward Arnold, pp. 545–595.

Riess, J. G. 2002 Fluorous micro- and nanophases with a biomedical perspective. *Tetrahedron* **58**, 4113–4131.

Russel, W. B., Saville, D. A. & Schowalter, W. R. 1989 Colloidal dispersions. In *Cambridge Monographs on Mechanics and Applied Mathematics* (ed. G. K. Batchelor), pp. 31–35. Cambridge University Press.

Saffman, P. G. & Delbrück, M. 1975 Brownian-motion in biological-membranes. *Proc. Nat. Acad. Sci. (USA)* **72**, 3111–3113.

Sickert, M., Rondelez, F. & Stone, H. A. 2007 Single-particle Brownian dynamics for characterizing the rheology of fluid Langmuir monolayers. *Eur. Phys. Lett.* **79**, 66005–66010.

Simons, K. & Ikonen, E. 1997 Functional rafts in cell membranes. *Science* **387**, 569–572.

Singer, S. J. & Nicholson, G. L. 1972 The fluid mosaic model of the structure of cell membranes. *Science* **175**, 720–731.

Trabelsi, S., Zhang, S., Lee, T. R. & Schwartz, D. K. 2006 Linactants: surfactant analogues in two dimensions. *Phys. Rev. Lett* **18**, 037802.

Veatch, S. L., Gawrisch, K. & Keller, S. L. 2006 Closed-loop miscibility gap and quantitative tie-lines in ternary membranes containing diphytanoyl PC. *Biophys. J.* **90**, 4428–4436.

Veatch, S. L. & Keller, S. L. 2002 Organization in lipid membranes containing cholesterol. *Phys. Rev. Lett.* **89**, 268101–268104.

Veatch, S. L. & Keller, S. L. 2003 Separation of liquid phases in giant vesicles of ternary mixtures of phospholipids and cholesterol. *Biophys. J.* **85**, 3074–3083.

Chapter 4

Dynamics of self-assembly of flower-shaped magnetic colloidal clusters

A. Ray, S. Aliaskarisohi, and T. M. Fischer,
Phys. Rev. E **82**, 031406 (2010)

Copyright by The American Physical Society 2010
DOI: 10.1140/epje/i2008-10421-5

Dynamics of self-assembly of flower-shaped magnetic colloidal clusters

A. Ray, S. Aliaskarisohi, and T. M. Fischer*
Institute of Physics, Universität Bayreuth, Bayreuth 95440, Germany
(Received 11 May 2010; published 24 September 2010)

In a static magnetic field paramagnetic and nonmagnetic colloids immersed in a ferrofluid self-assemble into fluctuating colloidal flowers. Adsorption and desorption of nonmagnetic petals to larger paramagnetic cores and changes in the petal conformation around the paramagnetic core induce a fluctuating dynamics. We track the motion of colloidal petals on the paramagnetic core. Adsorption and desorption of petals occur on a larger time scale than the rotational diffusion of the petals. Magnetic dipole interactions split the motion of the petals into different modes of rotational diffusion. Modes of rotational diffusion that change the petal conformation are suppressed compared to the conformation invariant rotational diffusion of all petals. The suppression of higher modes of rotational diffusion results in a subdiffusive dynamics of the individual petals.

DOI: 10.1103/PhysRevE.82.031406 PACS number(s): 82.70.Dd

I. INTRODUCTION

Colloidal assemblies are mesoscopic systems in thermodynamic equilibrium. Understanding the complex structures of these assemblies, the soft interactions between the individual particles, and the resultant dynamics in real space is of current interest; because colloidal assemblies are being used as models for atomic crystals [1] for glasses [2], for van der Waals crystals [3], and as systems for the study of dynamic self-assembly [4,5]. The softness of the interactions gives rise to fluctuations around the equilibrium that allows observing directly the transport processes [6–8] which lead to the dynamic self-assembly of the system. Diffusion is considered as one of these basic passive means for irreversible transport into equilibrium. It arises from fluctuations of the particle velocity due to stochastic forces. These forces act on the diffusing particles due to collisions with other particles from a reservoir at a certain temperature. In the presence of stochastic and deterministic microscopic forces, macroscopic diffusion can be expressed as the zeroth moment of the particle velocity autocorrelation and/or cross-correlation functions [9]. Kubo [9] extended a generalized concept of diffusion that allows defining and measuring the diffusion of interacting particles. It has been shown by Erb *et al.* [5] that paramagnetic and nonmagnetic colloidal particles immersed in a ferrofluid can self-assemble into colloidal flowers in a static magnetic field. The colloidal flowers result from the effective dipolar attraction of the paramagnetic colloids in which nonmagnetic particles behave as magnetic holes in the ferrofluidic background. The dipole interaction is a tensorial traceless interaction that depends on the angle between the magnetic moments and the particle separation. For holes sitting at the pole positions above or below the paramagnetic bead the dipole interaction with the paramagnetic bead is repulsive. In the equatorial plane on the other hand it is attractive. The dipole interaction between two magnetic holes on the other hand is repulsive in the plane normal to the magnetic moments and attractive along the direction of the magnetic moments. The planar structure of the colloidal flowers is a result of the complex angular dependency of the dipolar interactions.

Here, an attempt has been made to measure the normal modes of diffusion, as well as the adsorption and desorption kinetics of the petals in colloidal flowers using the concept proposed by Kubo [9]. Kubo generalized the concept of diffusions for situations where the particle kinetics is a superposition of random motion and directed interactions that force the particles into deterministic directions. The interactions correlate the motion of the particles that would otherwise show a degenerate individual diffusion. The correlations split the individual diffusion into statistically independent normal modes of diffusion. It is demonstrated that the adsorption and desorption kinetics as well as the mode dependence of the normal modes of petal diffusion can be understood by the competition of dipolar forces with the fluctuating forces from the viscous carrier fluid.

II. EXPERIMENT

We study the superparamagnetic Dynabeads M-270 carboxylic acid, 2.8 μm in diameter (Cat. No. 143.05 D) obtained from Invitrogen Dynal (Oslo, Norway), and Fluro-Max red fluorescent polymer microsphere beads with 1.0 μm diameter (Cat. No. R0100) obtained from Duke Scientific (Palo Alto, CA). The particles from Dynal are supplied in concentrations of approximately 2×10^9 beads ml^{-1} (10–30 mg ml^{-1}) and from Fluro-Max supplied with concentration of approximately 1% volume fraction suspended in water and respective surfactant. Paramagnetic particles are mixed with nonmagnetic particles and diluted ferrofluid EMG 705 FerroTec Ferrosound (FerroTec GmbH, Germany) with controlled proportions depending on the experiment. Electric current of 0.43 A was supplied to the water-cooled coils to produce a magnetic field of 10.0 mT, machined at University of Bayreuth. The mixture of the beads with ferrofluids was taken on a precleaned glass slide with a cover slip to reduce the air drift. Static magnetic field from the z direction was applied to the sample and was observed under the LEICA DM4000B (Leica Microsystems Wetzlar GmbH, Germany) fluorescence microscope through 63× polarization lens in reflecting mode. Videos were cap-

*thomas.fischer@uni-bayreuth.de

 ©2010 The American Physical Society

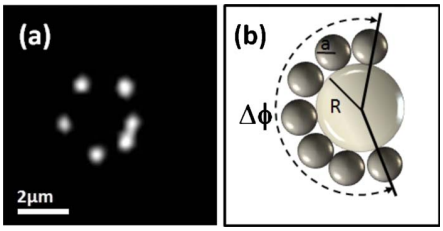

FIG. 1. (Color online) (a) Fluorescence microscope image of a six-petaled colloidal flower and (b) scheme of a colloidal flower. The paramagnetic core particle is nonfluorescent and hence not visible in the fluorescence image. The nonmagnetic fluorescence petal particles are visualized as bright spots in the fluorescence microscope image.

tured using a color charge-coupled device Basler camera (Basler A311fc) high frame rate from Basler AG, Germany.

III. ADSORPTION AND DESORPTION

Nonmagnetic beads of radius $a=0.5$ μm in a diluted aqueous ferrofluid (EMG 705 Ferrotec Ferrosound/water $=1:4$) adsorb at and desorb from the paramagnetic beads of radius $R=1.4$ μm. When they adsorb they form a colloidal flower with one paramagnetic bead at the core of the flower surrounded by several nonmagnetic beads forming the petals. A typical colloidal flower is depicted in Fig. 1. The assembly is a dynamic structure and the number of petals $N(t)$ fluctuates as a function of time because nonmagnetic beads adsorb at and desorb from the paramagnetic core. If we assume a Boltzmann distribution for the number of petals we may extract the potential energy of adsorption of N beads $U(N)$ as

$$U(N) - U(N_{\mathrm{ref}}) = -k_B T \ln\left(\frac{t(N)}{t(N_{\mathrm{ref}})}\right), \tag{1}$$

where $t(N)$ denotes the total time when one finds the colloidal flower with N petals, N_{ref} denotes a reference number of petals, and T is the temperature. In Fig. 2 we plot the adsorption potential as a function of the number of petals obtained via Eq. (1) by measuring $N(t)$ over a time duration of 4000 video frames. The adsorption potential shows a pronounced minimum near six petals. Assuming the potential to arise via dipolar attraction of the nonmagnetic beads to the paramagnetic core and due to dipolar repulsion between the equally spaced nonmagnetic petals, we predict a potential of

$$U(N) = \frac{4\pi\mu_0\chi_F^2 H^2 a^3}{9(R/a+1)^3} N\left[-\left(\frac{\chi_p}{\chi_F}-1\right)\frac{R^3}{a^3} + \frac{1}{2}\sum_{j=1}^{N-1}\frac{1}{8\,\sin^3(j\pi/N)}\right]. \tag{2}$$

In Eq. (2) μ_0 denotes the vacuum permeability, χ_F and χ_p are the effective susceptibilities of the ferrofluid and of the paramagnetic particle, and H is the external magnetic field. The potential has a minimum for an equilibrium number of particles given approximately by

$$N_{eq} = \frac{2\pi}{\sqrt{3}}\sqrt{\frac{\chi_p}{\chi_F}-1}\frac{R^{3/2}}{a^{3/2}}. \tag{3}$$

The dashed line in Fig. 2 shows a fit of the experimental data (solid line) obtained from Eq. (1) to the theoretical prediction in Eq. (2) using $\chi_P=0.082$ and $\chi_F=0.063$. Note that the theoretical fit exhibits a minimum around $N=7$ instead of the value $N=6$ in the experiment.

The $2N$-dimensional conformational space of the petals is spanned by the positions $(r_j, \varphi_j, j=1,\ldots,N)$ of the petals. In an N-fold colloidal flower the equilibrium configuration is determined by the conformation $r_j=R+a$ and $\varphi_j=2\pi j/N$ $(j=1,\ldots,N)$. A transition to a $(N-1)$-fold flower happens when, for example, the Nth petal separates from the flower $(r_N\to\infty)$ and the remaining $N-1$ petals rearrange their angular positions φ_j $(j=1,\ldots,N-1)$. We describe the reaction pathway of such a conformational change by the reaction coordinate Δr. The position of the Nth petal is $r_N=R+a+\Delta r_N$, $\varphi_N=0$ and the other beads adapt the positions $r_j=R+a$, $\varphi_j=\alpha(\Delta r_N)+2[\pi-\alpha(\Delta r_N)](j-1)/(N-2)$. The angle $2\alpha(\Delta r_N)$ describes the angle between the first and the $(N-1)$th petals that readjust [from $\alpha=2\pi/N$ to $\alpha=\pi/(N-1)$], while the Nth petal leaves the flower (see top in Fig. 3). We compute the reaction pathway such that the remaining petals $j=1,\ldots,N-1$ adjust their positions to the energy minimum of the dipolar energy of the N petal system while the Nth petal is fixed at the position $r_N=R+a+\Delta r_N$. Usually no significant changes in energy are computed when the separation Δr_N of the leaving petal has exceeded $\Delta r_N>4$ μm. Hence, separations larger than 4 μm can be considered as quasi-infinite separations. In Fig. 3 we plot the dipolar energy versus the reaction coordinates Δr_N $(N=3,\ldots,11)$ for a cascade of transitions from an 11-fold colloidal flower toward a flower with two petals. The cascade from the 11-folded flower to the theoretical minimum flower with seven petals is plotted on the left side. The remaining cascade from the minimum sevenfold flower toward a two-petal flower is plotted at the right. The reaction coordinates alternate between the lower (even N) and upper

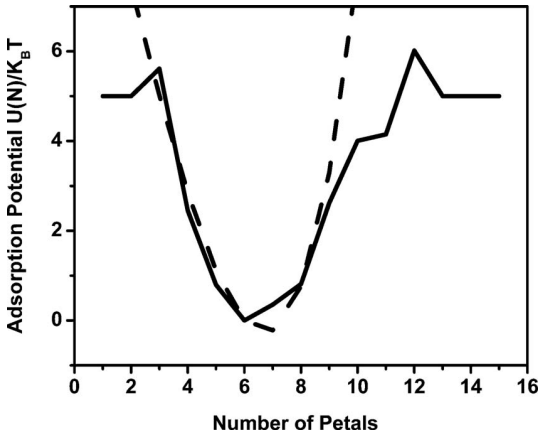

FIG. 2. Adsorption potential of the colloidal petals. The solid line is obtained from the experimental data by using Eq. (1). This potential levels off near $5k_BT$ due to lack of events. The dashed line is a fit according to Eq. (2).

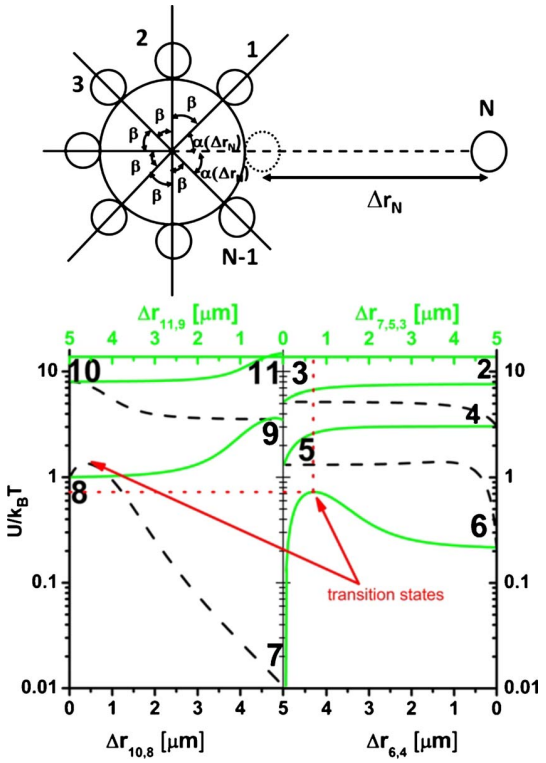

FIG. 3. (Color online) (Top) Scheme of a N-petaled flower losing the Nth petal along the reaction coordinate Δr_N, while the angular positions of the remaining petals adjust. (Bottom) The potential-energy cascade from a 11-petaled flower via the stable VII petal flower (left) toward a two-level flower (right). The flower loses the Nth petal along the reaction coordinate Δr_N; black curves correspond to the desorption of a N=even petal (lower abscissa), and green (gray) curves correspond to the desorption of a N=odd petal (upper abscissa). The energy of a petal separated by Δr_N=5 μm is indistinguishable from an infinitely separated petal and hence equals to the energy of a $(N-1)$-petaled flower. The numbers labeling the ends of the curves correspond to the number of the petals in the flower. The transition state between sixfold and sevenfold petal flowers [red (black) arrow] is at a distance of Δr=0.7 μm from the equilibrium position of the seventh petal and has an activation energy of $E_A=0.7k_BT$.

(odd N) axes. Numbers indicate equilibrium flowers of the corresponding number of petals. The potential thus changes from the N petal flower energy E_N to the $(N-1)$ petal flower energy E_{N-1}. The potential of a N petal flower with the Nth petal at a distance Δr=5 μm is indistinguishable from the potential energy of a $(N-1)$-petaled flower. This confirms that a petal at a distance $\Delta r>5$ μm can be considered as fully separated from the flower. For the desorption of the seventh petal the energy exhibits a maximum E_A along the reaction pathway. This maximum corresponds to a transition state, i.e., a saddle point in conformational space located at a distance $\Delta r_{7,max}\approx 0.7$ μm from the minimum position of the seventh petal with an activation barrier of the desorption of $(E_A-E_7)\approx 0.7k_BT$. The activation energy for the adsorption is $(E_A-E_6)\approx 0.5k_BT$. A qualitatively similar transition state is computed between the seven- and eight-petaled flowers. All other transitions in the number of petals show no transition state. Hence, all flowers with $N<6$ and $N>8$ are unstable. The six- and eight-petaled flowers are metastable $E_6, E_8>0$, and the sevenfold flower is the stable conformation $E_7=0$ for the given parameter set. Assuming an Arrhenius behavior for the rate constant $k_{6\to 7}$ of the adsorption process of the seventh petal one would expect a rate constant of the order

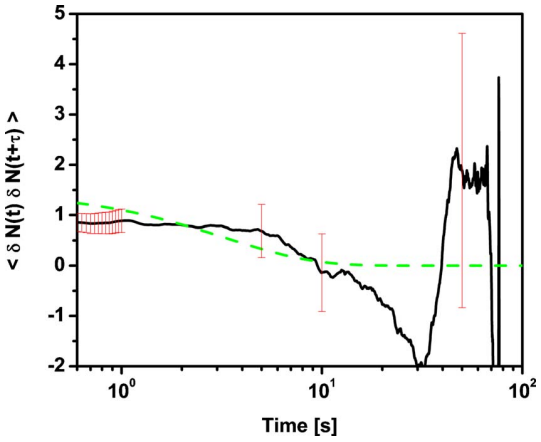

FIG. 4. (Color online) The autocorrelation function $\langle \delta N(t)\delta N(t+\tau)\rangle$ versus time as obtained from the experimental data (solid line). The number of petals changes on a time scale of 3 s. The dashed line corresponds to an exponential decay with rate constant 0.3 s^{-1}. The statistical error (error bars) of the correlation function increases when the time lag τ approaches the time of measurement τ_{meas}=70 s.

$$k_{6\to 7}=\frac{k_BT}{6\pi\eta a}(\Delta r_{max})^{-2}\exp[-(E_A-E_6)/k_BT], \tag{4}$$

where $\eta=10^{-3}$ N s m^{-2} is the ferrofluid viscosity. Inserting the values $\Delta r_{max}\approx 0.7$ μm and $(E_A-E_6)\approx 0.5k_BT$ from Fig. 3 into Eq. (4) we obtain $k_{6\to 7}\approx 0.3$ s^{-1}. In Fig. 4 we plot the autocorrelation function of the petal number,

$$\langle \delta N(t)\delta N(t+\tau)\rangle, \tag{5}$$

where $\delta N(t)=N(t)-N_{eq}$ denotes the petal number fluctuation. The autocorrelation function decays with a typical rate of $k_{ex}\approx 0.3$ s^{-1} in good agreement with the estimate given by Eq. (4). For larger times $\tau>10$ s the experimental autocorrelation function becomes statistically unreliable since the number of events ($\propto \tau_{meas}-\tau$) drops to 1 as the time separation τ approaches the time τ_{meas} of the measurement.

IV. PETAL CONFORMATION AND DYNAMICS

Once the petals adsorb to the paramagnetic core there is some freedom of conformation, and one observes flowers with petals equally spaced around the core as well as conformations where the petals are crowded at one side of the core. We define the one-dimensional density of particles as

$$\rho=N/\Delta\phi, \tag{6}$$

where $\Delta\phi$ denotes the minimum angular range over which the N petals are distributed and $2\pi-\Delta\phi$ is the largest gap

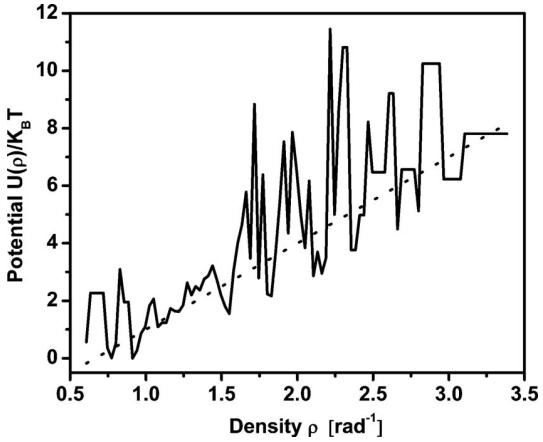

FIG. 5. Effective petal potential as a function of the petal density ρ as obtained from the experimental data via Eq. (7). The dashed line is a linear fit.

between the petals. We compute the potential energy of a conformation $U(\rho)$ as

$$U(\rho) - U(\rho_{ref}) = -k_B T \ln\left(\frac{g(\rho_{ref})\Delta\rho_{ref} t(\rho,\Delta\rho)}{g(\rho)\Delta\rho t(\rho_{ref},\Delta\rho_{ref})}\right), \quad (7)$$

where $t(\rho,\Delta\rho)$ is the total time when the petals in the flower show a density in the interval $[\rho,\rho+\Delta\rho]$ and where

$$g(\rho) \propto \left(\frac{N}{\rho} - \frac{N}{\rho_{hc}}\right)^{N-2} \quad (8)$$

is the leading-order approximation for the configurational space density [10] available for conformations of density ρ, whereas $\rho_{hc}=(R/a+1)/2$ is the maximum (hard-core) packing density of the petals around the core. Figure 5 shows the potential $U(\rho)$ computed via Eq. (7) for flowers consisting of an arbitrary number of petals. The resolution $\Delta\rho$ varies with ρ and is chosen in a way so as to ensure that $t(\rho,\Delta\rho)>0$ for all ρ. Since the data at higher potential are sparse the resolution $1/\Delta\rho$ is best at the minimum and decreases when moving toward higher potential. We find the lowest potential for densities $\rho\approx 1$ corresponding to a hexagonal arrangement of the petals with equal spacing of $\pi/3$ between the petals. The petal conformation results from the simultaneous minimization of the petal number and the minimization of the dipolar repulsion between the petals. The dipolar repulsion between the petals, however, is weak and allows for significant fluctuations around a conformation. We therefore tracked the angular position $\phi_j(t)$ $[j=1,2,3,\ldots,N(t)]$ of the adsorbed petals as a function of time. The accuracy of the tracking of $\phi_j(t)$ was better than 2°. The angular frequency $\omega_j(t)=\dot{\phi}_j(t)$ of each individual petal is a fluctuating function of time. We measure the angular frequency using finite differences of the angular positions of consecutive frames. The frame rate of the camera was 30 frames per second. We define the autocorrelation function of the angular frequency of two petals of a colloidal flower with N petals as

$$C_N(\sigma,\tau) = \langle \omega_j(t)\omega_{j\pm\sigma}(t+\tau)\delta(N(t)-N)\delta(N(t+\tau)-N)\rangle. \quad (9)$$

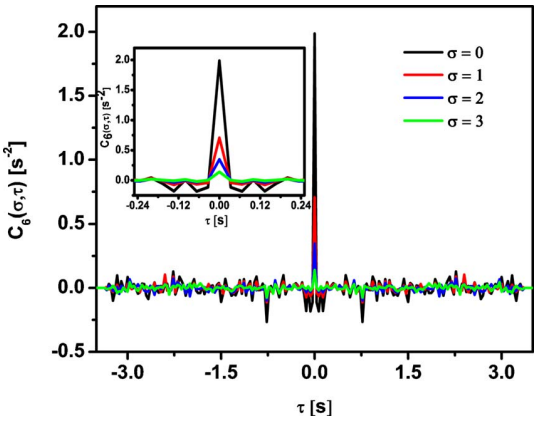

FIG. 6. (Color online) Angular frequency autocorrelation and cross-correlation functions for a colloidal flower with six petals. The black line corresponds to the autocorrelation, while the red, blue, and green lines correspond to cross correlations between nearest ($\sigma=1$), second-nearest ($\sigma=2$), and third-nearest ($\sigma=3$) neighbors, respectively.

Here, σ denotes the neighbor number ($\sigma=0$ is the same particle, $\sigma=1$ is the nearest neighbor, etc.). Both delta functions $\delta(N(t)-N)$ and $\delta(N(t+\tau)-N)$ discard all times where the petal number deviates from the fixed petal number N from the correlation.

In Fig. 6 we plot $C_6(\sigma,\tau)$ versus τ for $\sigma=0,1,2,3$. The angular frequencies are correlated for zero time delay (i.e., $\tau=0$), showing that part of the petal diffusion can be considered as a Markovian process on the time scale $\tau>0.03$ s of the measurement. The most prominent observation is that neighboring petals are not statistically independent. As does the petal autocorrelation function $C_6(0,\tau)$, the petal cross-correlation functions $C_6(\sigma\neq 0,\tau)$ also show the same albeit weaker instantaneous positive correlation. This is a dynamic proof of the deterministic interaction of the petals. Apart from this positive correlation a weak anticorrelated decay is observed for the autocorrelation $C_6(0,\tau)$ and the cross correlation $C_6(\sigma\neq 0,\tau)$ for $\tau>0.05$ s (see the inset in Fig. 6). It is a measure for the retardation of the interaction. In single file diffusion [11–13], where particles interact only via hard-core repulsion, a strong algebraic anticorrelation significantly alters the diffusion of the particles. Neighboring particles in single file diffusion remain uncorrelated at short times and become anticorrelated only at times typical for the individual diffusion time needed to encounter each other. The retardation of such a hard-core interaction is significant. Single file diffusion becomes most prominent in the thermodynamic limit $N\to\infty$, where the time scale of the simultaneous correlated diffusion of the rigid flower separates from the individual diffusion of the petals.

Our system differs from a system exhibiting single file diffusion. It has a small number of petals, and the petals interact instantaneously via the soft dipolar interactions; retardation effects are weak. In no time are the petals allowed to diffuse individually. Hence, the relatively weak delayed anticorrelation follows the instantaneous delta correlation with a relative short delay. The diffusion constant of the petals is given by half the area under the autocorrelation func-

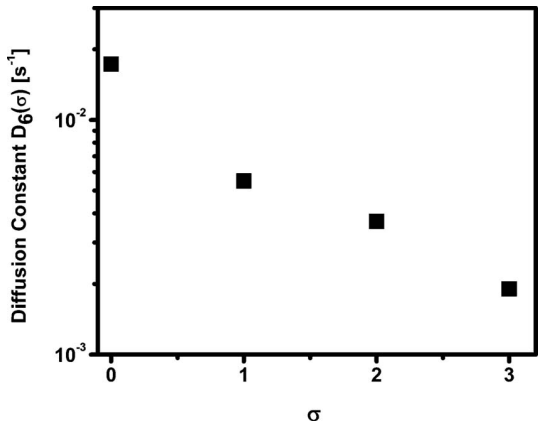

FIG. 7. Diffusion constant $D_6(\sigma)$ versus σ.

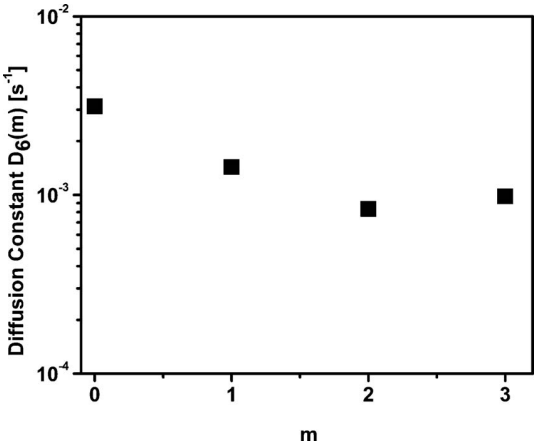

FIG. 8. Normal-mode diffusion constants $D_6(m)$ versus the mode number m.

tion. While the finite frame rate of the camera broadens the experimental correlation function, the area under the correlation function is not affected by the convolution of the data with the time resolution function of the camera. Hence, the diffusion constants have no significant dependence on the frame rate of recording,

$$D_N(\sigma) = \int_0^\infty d\tau C_N(\sigma,\tau). \tag{10}$$

Equation (10) is Kubo's [9] generalization of the concept of diffusion to particles that interact. The interaction of the particles causes the motion of one particle to statistically depend on the motion of another. The statistically dependent motion of the particles can be decomposed into statistically independent normal modes of motion. In Fig. 7 we plot the diffusion constant $D_6(\sigma)$ versus σ. The petals behave like being coupled by soft springs, with petals not diffusing independently, but with neighbors performing a correlated diffusion. The correlation decreases when moving away toward further distant neighbors. We may decompose the correlated motion of the petals into uncorrelated normal modes of diffusion via

$$\phi(m,t) = \frac{1}{\sqrt{N}}\sum_{j=1}^{N} e^{2\pi imj/N}\phi_j(t). \tag{11}$$

The corresponding statistically independent diffusion constants of the normal modes,

$$D_N(m) = \frac{1}{N}\sum_{\sigma=1}^{N} e^{2\pi im\sigma/N}D_N(\sigma), \tag{12}$$

are plotted in Fig. 8. The mode $m=0$ has the highest diffusion constant, and the diffusion constant decreases with the mode number m. The mode $m=0$ corresponds to a rigid rotation of all petals by the same amount. It therefore corresponds to the rotational diffusion of the entire flower that leaves the conformation of the flower unchanged. The higher modes $m>0$ involve relative motion of petals that change the conformation. Such modes are suppressed to diffuse by the dipolar repulsion between the petals. The higher is m, the shorter is the distance $2\pi/m$ between petals that are moving in opposite directions. The most likely conformation is an equilibrium conformation such that an $m\neq 0$ mode usually raises the dipolar energy of the system. This explains why the diffusion of higher modes $|m|>0$ is suppressed by the dipole-dipole interaction.

Contrary to single file diffusion the diffusion mode of the petals arises from mostly instantaneous response of the flower to conformational changes. In single file diffusion the suppression of higher modes arises from a retarded response to conformational changes that only sets in when one petal diffuses to its neighbor and encounters its hard-core repulsion.

In conclusion we have characterized the dynamic fluctuations of magnetic colloidal flowers. These fluctuations can be understood as a result of deterministic forces arising due to dipolar interactions and statistical forces arising from the collisions of the embedding fluid. The soft character of the dipolar interactions places this system between that of a free system and a system interacting via hard-core interactions. The soft confinement of the particles leads to a mode-dependent diffusion that differs from single file diffusion. The desorption and adsorption of the petals can be understood as activated processes. The colloidal flowers are thus a two-dimensional model system for the dynamics of more complex three-dimensional colloidal assemblies such as Pickering emulsions [14] and colloidosomes [15].

[1] A. van Blaaderen, R. Ruel, and P. Wiltzius, Nature (London) **385**, 321 (1997).
[2] E. R. Weeks, J. C. Crocker, A. C. Levitt, A. Schofield, and D. A. Weitz, Science **287**, 627 (2000).
[3] N. Osterman, I. Poberaj, J. Dobnikar, D. Frenkel, P. Ziherl, and D. Babic, Phys. Rev. Lett. **103**, 228301 (2009).
[4] P. Tierno, R. Muruganathan, and Th. M. Fischer, Phys. Rev. Lett. **98**, 028301 (2007).
[5] R. M. Erb, H. S. Son, B. Samanta, V. M. Rotello, and B. B. Yellen, Nature (London) **457**, 999 (2009).
[6] K. Schätzel and B. J. Ackerson, Phys. Rev. E **48**, 3766 (1993).
[7] E. Vignati, R. Piazza, and T. P. Lockhart, Langmuir **19**, 6650 (2003).
[8] Y. Terada and M. Tokuyama, J. Phys. Soc. Jpn. **79**, 034802 (2010).
[9] R. Kubo, J. Phys. Soc. Jpn. **12**, 570 (1957).
[10] The assumption that $2\pi-\Delta\phi$ is the largest gap forbids conformations with density ρ that have a larger gap between the first and Nth petals. Three particle correlations of this kind have been neglected when approximating the conformational space density $g(\rho)$. The systematic error introduced in this way cancels near the potential minimum due to the normalization with $g(\rho_{ref})$.
[11] Q. H. Wei, C. Bechinger, and P. Leiderer, Science **287**, 625 (2000).
[12] J. Kärger, Phys. Rev. A **45**, 4173 (1992).
[13] V. Kukla, J. Kornatowski, D. Demuth, I. Gimus, H. Pfeifer, L. V. C. Rees, S. Schunk, K. K. Unger, and J. Kärger, Science **272**, 702 (1996).
[14] R. Aveyard, B. P. Binks, and J. H. Clint, Adv. Colloid Interface Sci. **100-102**, 503 (2003).
[15] A. D. Dinsmore, M. F. Hsu, M. G. Nikolaides, M. Marquez, A. R. Bausch, and D. A. Weitz, Science **298**, 1006 (2002).

Chapter 5

Using Symmetry Breaking for Directed Transport of Paramagnetic Colloids on Garnet Films

S. Aliaskarisohi, T. H. Johansen, and Th. M. Fischer,
J. Phys. Chem. B , **115**, 2243 (2011)

Copyright by The American Chemical Society 2011
DOI: 10.1021/jp1118

THE JOURNAL OF PHYSICAL CHEMISTRY B

ARTICLE

pubs.acs.org/JPCB

Using Symmetry Breaking for Directed Transport of Paramagnetic Colloids on Garnet Films

S. Aliaskarisohi,[†] T. H. Johansen,[‡] and Th. M. Fischer*,[†]

[†]Institut für Experimentalphysik, Universität Bayreuth, 95440 Bayreuth, Germany

[‡]Department of Physics, University of Oslo, P.O. Box 1048, Blindern, 0316 Oslo, Norway

ABSTRACT: The transport behavior of paramagnetic particles on top of a ferrimagnetic garnet film is investigated in a modulated external magnetic field. Broken symmetries are required to direct the transport of the particles. We provide such symmetry breaking by tilting the external field modulation with respect to the normal direction of the garnet film and by the intrinsic geometrical symmetry breaking of the garnet film magnetic pattern. The interplay of both symmetry breaking mechanisms causes a rich variety in transport behavior and direction. We corroborate our experimental transport directions by comparing experimental with theoretical transport phase diagrams. Directing the transport of paramagnetic colloids will be useful when they are loaded with biomedical cargo on a magnetic lab-on-a-chip device.

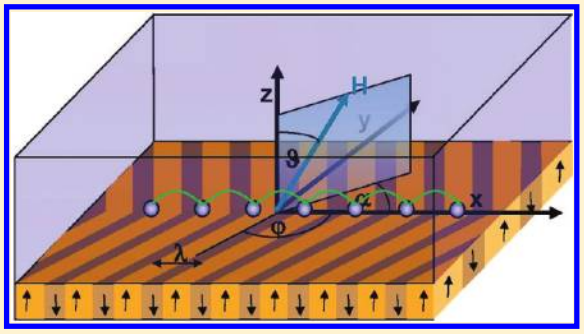

1. INTRODUCTION

Deterministic[1,2] as well as statistical ratchets[3−5] convert the bounded periodic or stochastic dynamics of an external field into the driven unbounded motion of objects coupling to the external force. A wheel exerts a continuous thrust to the ground it moves on. A ratchet in contrast exerts a thrust only during a critical period of time when the moving object experiences instability in the energy landscape generated by the external force. A broken symmetry during this instability is necessary to direct the thrust in the desired direction. The motion of the object is a sequence of hops during the instability and periods where the particle is largely arrested in a local minimum of the energy landscape.

Here we are interested in the transport direction of paramagnetic colloidal particles on a magnetic garnet film[6] when having two competing ways of breaking the symmetry of a magnetic stripe pattern. Either the symmetry is broken by tilting the external magnetic field with respect to the film normal or a wedge geometry of the stripes imposes a preference direction. Both ways to break the symmetry span a 2D parameter space, where different directions of motion are possible. The responses in motion of the particles to the two ways of breaking the symmetry are correlated: When both symmetry breaking mechanisms are used simultaneously, they may lead to a transport directions opposite to either way used individually.

2. EXPERIMENT

We experimentally observe the transport of paramagnetic colloids on a magnetic garnet film when driven with an external magnetic field. A scheme of the experiment is shown in Figure 1.

We studied the hopping of paramagnetic colloids (Dynabeads-M-270 carboxylic acid) with a diameter of $2a = 2.8 \pm 0.1\ \mu$m, effective susceptibility $\chi_{\mathrm{eff}} = 0.17$, and concentration of 2×10^9 beads/mL purchased from Invitrogen. The original particle solution is diluted with pure water (Millipore milli-Q water 18.2 MΩ × cm) to a concentration of 2×10^7 beads/mL and placed on two different 4 μm thick magnetic garnet films of composition $Y_{2.5}Bi_{0.5}Fe_{5-q}Ga_qO_{12}$, which were epitaxially grown on a gadolinium gallium garnet substrate. The resulting ferrimagnetic films have a uniaxial anisotropy with a spontaneous magnetization of $M_s = 8.4$ and 9.2 kA/m. Magnetic stripe domains are magnetized perpendicular to the film and alternate between up and down magnetization with average wavelength of $\lambda = 12$ and 14 μm, respectively. The persistence length of the garnet films used is limited, and the stripes abruptly change direction, creating wedges in the pattern that are characterized by the angle φ between one arm of the stripe pattern and the wedge bisector. The angle φ is one of the symmetry breaking parameters that can induce directed motion. In our films, there is a distribution of wedge angles in the range of $45 < \varphi < 120°$. The garnet films were coated with polysodium 4-styrene sulfonate to prevent adhesion of particles to the surface.

An external time-dependent magnetic field $\mathbf{H}_{\mathrm{ext}}(t) = \mathbf{H}^0_{\mathrm{ext}} e^{i\omega t}$ drives the motion of the particles with a frequency of $\omega/2\pi = 5$ Hz. The orientation of the field $\mathbf{H}^0_{\mathrm{ext}} = H_{\mathrm{ext}}$ (cos α sin ϑ, sinα sinϑ, cosϑ) with respect to the film and the wedge is characterized by the tilt angle $\vartheta = 23°$, which serves as an additional

Received: December 14, 2010
Revised: January 25, 2011
Published: February 22, 2011

ACS Publications © 2011 American Chemical Society

symmetry breaking parameter directing the motion of the particles. It is produced by two solenoids oriented perpendicular and parallel to the film. The orientation α of the wedge bisectors to the magnetic field is randomly distributed allowing the full range $0 < \alpha < 2\pi$ to be probed. The amplitude of the magnetic field was set to $H_{ext} = 0.165 \times 10^4$ A/m.

Polarization microscopy was used to visualize simultaneously the domain pattern and the particle transport. Domains are visible because of the polar Faraday effect. Movies of the particle transport were recorded, digitized using a digital camera (A311 fc BASLER), and stored on a computer for further analysis.

3. TRANSPORT INSTABILITY

The superposition of the heterogeneous magnetic field produced by the garnet film pattern and the homogeneous external time-dependent field results in a magnetic field that varies in both space and time. The normal component of the external field additionally affects the position of the domain walls because the normal field increases the width of the domains having a magnetization parallel to the field and decreases the width of the antiparallel ones. As a result, the positions $x_{\pm}^{m} = \lambda/4[(4m + 1) \pm (1 + H_{ext}/M_s \cos \vartheta \sin(\omega t))]$, $m = 0, 1, 2, ...$, where the domain walls intersect the bisector of the wedge, also oscillate as a function of time. The external magnetic field therefore both superposes to and perturbs the magnetic field of the garnet film. The paramagnetic particles of volume $V = 4\pi a^3/3$ above the garnet film experience the total magnetic field, where they have a magnetic energy of $E = -V\mu_0\chi_{eff}H^2$. Here μ_0 denotes the vacuum permeability. In the absence of an external field, this energy is minimized above the intersection of the domain walls with the wedge bisector, and the particles are localized at those positions. The minimal position may be computed from the condition $\nabla E = 0$. A weak external field slightly perturbs the energy of the particles; however, the energy minima remain stable at all times and move in a bounded region around the zero-external field position. The result is a particle motion that is bounded and locked to the motion of the domain wall position. A sketch of such bounded particle motion is depicted in Figure 2a. The particles return to their original position after one period of the modulation, and no net motion of the particle results from the modulation.

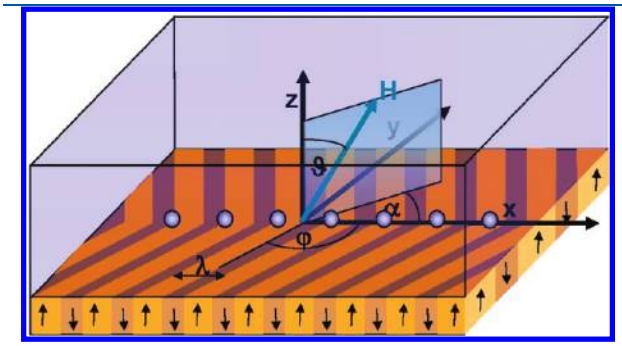

Figure 1. Scheme of a magnetic garnet film with alternating magnetized wedge domains, the paramagnetic particles in aqueous solution placed above the film. The film is modulated with a tilted oscillating external magnetic field. Particles will transport along the wedge bisector of angle φ. The transport direction depends on the angle between wedge bisector and in-plane field, α, and the tilt angle of external field, ϑ.

The situation changes when the external field surmount a critical threshold $H_{ext} > H_c$. At the critical field, the energy minimum converts to a saddle point $(\xi\cdot\nabla)^2 E = 0$, and the particle hops into an adjacent minimum along the unstable direction defined by the vector ξ. If the energy landscape happens to be symmetric, then the particle has the choice to hop in either positive $(+\xi)$ or the negative $(-\xi)$ direction, and the resulting motion is a stochastic hopping resulting in a diffusive dispersion of the particles. A sketch of such stochastic hopping is depicted in Figure 2b. The motion is unbounded, but no net direction of the motion results from this form of modulation.

Directed motion may result when the symmetry is broken, whereas the external field reaches the critical threshold H_c. For that situation, the minimum converts to a true saddle point $(\xi\cdot\nabla)^3 E \neq 0$, and the particle has only one choice of direction to hop to the next minimum. A smart way of external modulation will lead to a consecutive sequence of instabilities where the particle-carrying minimum is converted to a saddle point that directs the particle always in the same direction. Figure 2c shows the directed motion of such a smart modulation.

In the work of Tierno et al.,[78] all three kinds of hopping have been explained for a garnet film with stripe pattern, and paramagnetic particles were placed above it. They showed that tilting

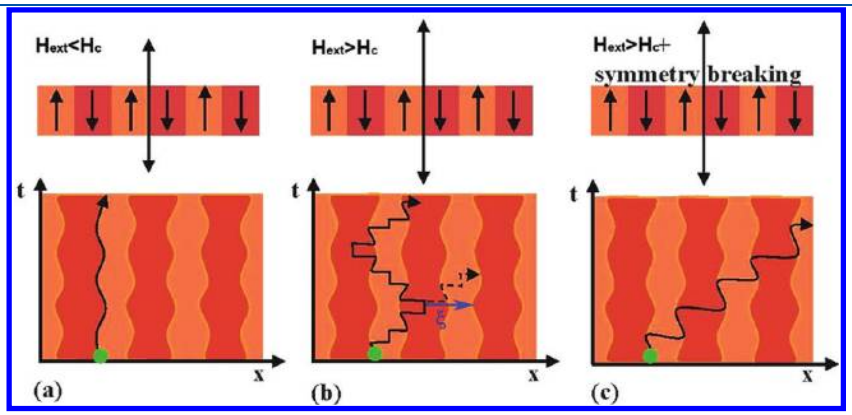

Figure 2. Sketch of the possible forms of motion above the modulated magnetic garnet film pattern. (a) In a weak external field $H_{ext} < H_c$, particles are locked to the motion of the domain walls. (b) In an external field normal ($\vartheta = 0$) to a straight $\varphi = \pi/2$ stripe pattern surmounting the critical field $H_{ext} > H_c$, the domain wall positions become unstable, resulting in a diffusive hopping with no net direction of the transport. (c) Breaking the symmetry by tilting the field ($\vartheta = 0$) or using a wedge $\varphi = \pi/2$ causes a smart sequence of instabilities that let the particles hop always into the same direction as their pervious steps.

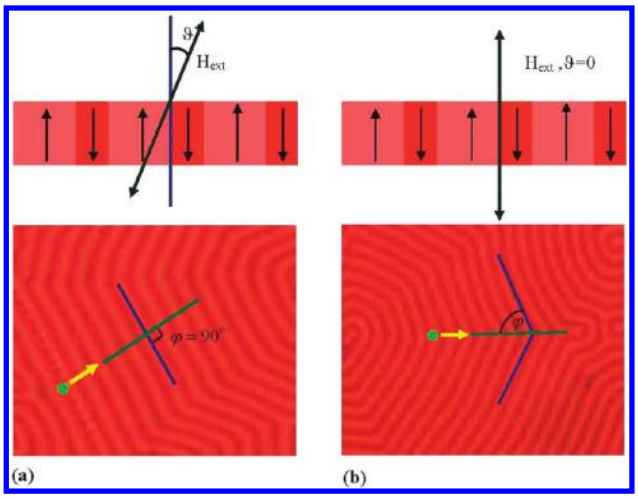

Figure 3. Two ways of breaking the symmetry: (a) By applying the external tilted field, the particles hop perpendicular to the stripes in the direction of the tilt. (b) With a wedge pattern, one forces the particles to hop along the bisector against the direction of the curvature.

the modulated field with respect to the film normal ($\vartheta \neq 0$) represents a smart way to direct the particles into one direction. Another form of smart modulation was discovered by Dhar et al.,[9] who used the stripe curvature to direct ferrofluid-filled mouse macrophages.

The current work aims at experimentally and theoretically studying the effect of combining different ways of smart modulation. Here we break the symmetry by either tilting the field with respect to the film or by using wedge patterns to direct the particles. As will be shown, the resulting motion of the particles is more complex than what one would guess from the results of the individual ways to break the symmetry.

4. EXPERIMENTAL RESULTS

Figure 3 shows the hopping direction for the two different ways to break the symmetry. The particles above a straight stripe pattern hop in the direction of the tilt, whereas the particles above the wedge pattern in an external field normal to the film are directed along the wedge bisector against the direction of the curvature of the wedges.

The situation is much more complex when we apply both ways to break the symmetry. Figure 4 shows the hopping direction of different wedges on the same garnet film when subject to a field that is tilted with respect to the film normal. The wedges have different values of both the wedge angle φ and the bisector orientation α. In contrast with the situation when the external field is oriented normal to the film, hopping directions both against and along the wedge curvature are observed.

Although the behavior is much more complex when both symmetry breaking mechanisms are present, the transport remains smart with a definite direction of the hopping. The direction of the hopping is a result of the magnetic energy landscape at the time of the instability. It depends on the three parameters ϑ, φ, and α. We have experimentally determined the phase diagram of the hopping directions as a function of two of those parameters. Before presenting those results in Section 6, we give a theoretical description of the energy landscape.

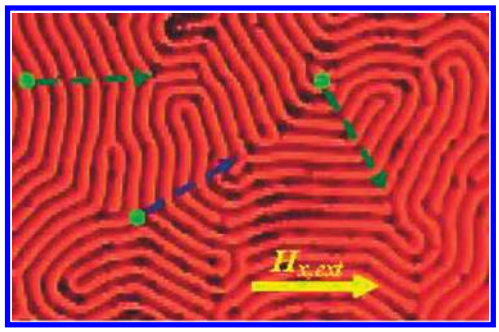

Figure 4. Transport directions above a stripe-patterned film in a tilted magnetic field with wedges. The tilt direction is along the x axis. Particles are transported along the bisectors of the wedges either in direction (blue) or against (green) the direction of the curvature of the wedge.

5. ENERGY LANDSCAPE OF A WEDGE PATTERN

The magnetic field above the garnet film fulfills the magnetostatic form of Maxwell's equations

$$\nabla \cdot \mathbf{H} = 0 \tag{1}$$

and

$$\nabla \times \mathbf{H} = 0 \tag{2}$$

with the boundary conditions

$$H_z(x,y,z = 0^+) = M_z(x,y,z = 0^-) = \pm M_s \tag{3}$$

at the garnet film/water interface and

$$\mathbf{H}(z \rightarrow \infty) = \mathbf{H}_{ext} \tag{4}$$

far from the interface. Equation 2 may be expressed in scalar form using the magnetostatic potential ψ satisfying $\mathbf{H} = \nabla\psi$. The magnetostatic potential fulfills the Laplace equation $\nabla^2\psi = 0$, and its solution[10] subject to the above boundary condition reads

$$\psi = \mathrm{H}_{ext} \cdot x - (M_s + H_{z,ext})(\psi_{N,+} - \psi_{-N,-}) + 2M_s \sum_{n=-N}^{N} (\psi_{n,+} - \psi_{n,-}) \tag{5}$$

where

$$\psi_{n,\pm} = \frac{1}{2\pi}[2z \operatorname{arccot} \frac{x - x_{n,\pm} + r_{n,\pm} \cos\varphi}{z \sin\varphi} + 2y \cos\varphi \operatorname{atanh} \frac{y \sin\varphi}{r_{n,\pm} + (x - x_{n,\pm}) \cos\varphi} - x \sin\varphi \ln((r_{n,\pm}^2 - z^2)\cos^2\varphi + 2r_{n,\pm}(x - x_{n,\pm}) \cos\varphi + r_{n,\pm}^2 - y^2)] \tag{6}$$

where $r_{n,\pm}^2 = (x - x_{n,\pm})^2 + y^2 + z^2$ and where N cuts off the number of stripes at the wedge.

By knowing the field, we can compute the magnetostatic energy landscape of the paramagnetic particles. A contour plot of this landscape at the elevation $z = a = 0.07\lambda$ is shown in Figure 5 along the bisector coordinate x as a function of time t. In this particular example (φ = 60°, α = 45°, ϑ = 23°, and H_{ext} =

dx.doi.org/10.1021/jp1118585 |J. Phys. Chem. B 2011, 115, 2243–2247

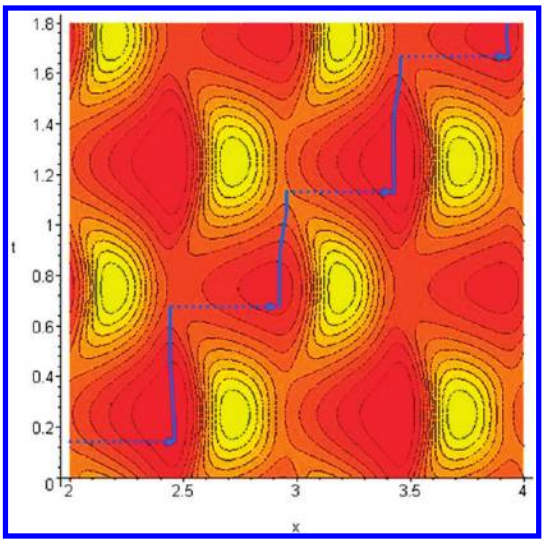

Figure 5. Contour plot of the magnetostatic potential as a function of the bisector coordinate x and the time t. The red regions correspond to the minima, and the yellow regions are maxima of the potential. The trajectory of one particle is depicted in blue.

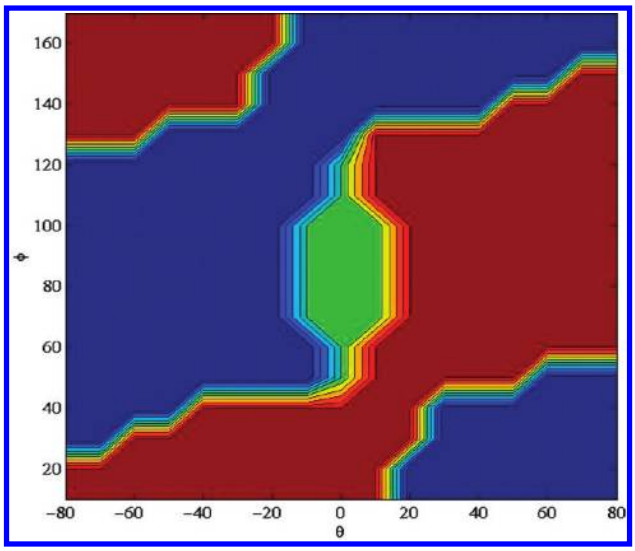

Figure 6. Theoretical phase diagram of the transport behavior of wedges with bisectors oriented into the tilt direction of the magnetic field ($\alpha = 0$) as a function of the tilt angle ϑ and the wedge angle φ. The green region corresponds to a locked phase without particle transport. The red and blue phases are phases where particles hop toward the right and the left, respectively.

$0.25M_s$), the potential minima merge with maxima to the right, creating a saddle point at $x = (0.5 + n)\lambda$ at the time $\omega t = 0.6$ that lets the particle hop to the right. A trajectory of a particle will follow the blue line in Figure 5. Hence, the contour plots allow us to read off the direction of the hopping for a particular set of parameters.

6. TRANSPORT PHASE DIAGRAMS

Shown in Figure 6 is the phase diagram of hopping of the particles in terms of the wedge angle φ and the tilt angle ϑ. The tilt direction of external field for this phase diagram coincides

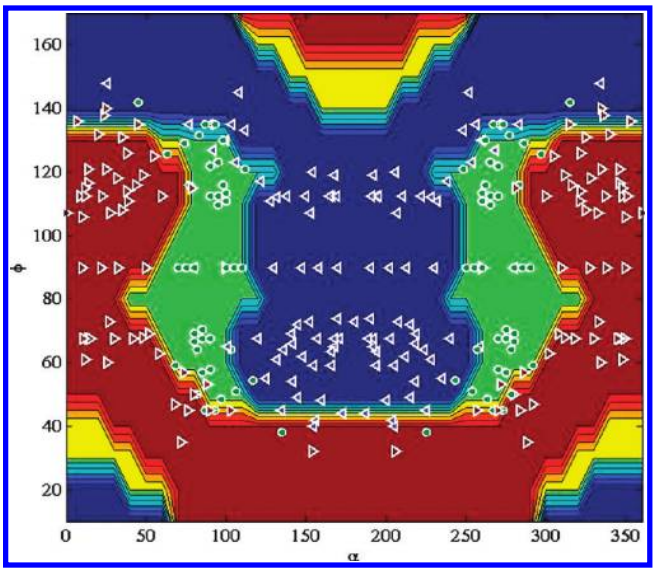

Figure 7. Theoretical and experimental phase diagram of the transport behavior of wedges with a tilt of the field of $\vartheta = 23°$ as a function of the bisector orientation α and the wedge angle φ. The green regions correspond to a locked phase without particle transport. The red and blue phases are phases where particles hop toward the right and the left, respectively. In the yellow phase, the simultaneous symmetry breaking mechanisms do not result in a smart modulation, and particles hop either way. Experimental data points (○, no hopping; left-pointing triangle, hopping toward the left; and right-pointing triangle, hopping toward the right).

with the bisector of the wedge ($\alpha = 0$). We find three different phases marked in red, blue, and green. In the green phase, the tilt and the deviation of the wedge angle from a straight stripe are insufficient to cause directed motion of the particles. It corresponds to a localized phase where the particles are locked to the domain walls. The red and blue phases, in contrast, are phases where the particles are directed toward the right and the left, respectively, and in this phase diagram, the field projection for $\vartheta > 0$ is toward the right, and for $\vartheta < 0$, it is toward the left. For $\varphi = 90°$, the wedge degenerates to a straight stripe pattern, and the hopping direction is determined by the tilt angle. The direction of the hopping remains tilt-dominated for a broad region $\varphi = 90 \pm 35°$ around the straight stripes. Only for sharp wedge angles $\varphi < 45°$ and $\varphi > 125°$ can the angle of the wedge reverse the behavior dictated by the tilt. If we concentrate on these regions and focus on the behavior in the absence of tilt $\vartheta = 0$, then we conclude that the wedge breaks the symmetry in a way so as to support hopping against the direction of the wedge curvature. One would guess that this should be in synergy with the situation encountered when the tilt is also pointing against the curvature of the wedge. In the phase diagram of Figure 6, however, we find the region $\varphi < 45°$ and $\vartheta > 25°$, where the particle hop is in direction of the curvature and opposite to the tilt direction. This shows that a simple superposition principle does not hold for nonlinear processes, and the resulting hopping direction is opposite to what would be expected if one applies both symmetry breaking mechanisms individually.

In the experiments, we kept the tilt angle fixed at $\vartheta = 23°$. The wedge angle φ and the bisector orientation to the external field α, however, varied because of the distribution of wedge angles and bisector orientations on the film. In Figure 7, we plot the transport phase diagram as a function of the latter angles and

incorporate the experimental measurements. We use the same color coding as in Figure 6. The additional color yellow corresponds to a region where the combination of the two symmetry breaking effects does not result in a smart modulation, and one finds particles hopping to the right and to the left simultaneously.

In Figure 7, for wedge angles φ ranging from 45 to 125°, we are in the tilt-dominated regime, and the hopping in this region usually follows the direction dictated by field. Only when $\alpha \approx 90$ or 270° does the component of the tilt along the bisector become too weak to cause directed motion, and the particles fall into the locked localized phase. In the wedge-dominated regime $\varphi < 45°$ and $\varphi > 125°$, the hopping is into the direction against the wedge curvature if the tilt angle also does not point in this direction. When the tilt points against the direction of the wedge curvature (blue regions in the lower corners and red region at the upper boundary of Figure 7), the particles hop in the direction of the curvature and against the tilt direction. This corresponds to the region also found in Figure 6, where the particles hop opposite to the direction encountered when both symmetry breaking mechanisms are applied individually

The experimental data points that are inserted in Figure 7 confirm the theoretical predictions. Most of the data lie in the region $40 < \varphi < 140°$ and agree with the theoretical phase diagram. Data points that disagree with the theory are located in the vicinity of the theoretical phase boundaries. Our data confirm the changes of hopping directions in the tilt-dominated regions $45 < \phi < 120°$ as well as the transition to the wedge-dominated phases. So far we could not prove or disprove the existence of phases where particles are predicted to hop into the opposite direction than with the symmetry breaking mechanisms applied individually. We also could not experimentally confirm the loss of smart modulation in the yellow regions. The experimental access to these regions would require wedges with opening angles $\varphi < 45°$, which were not available in the present samples.

7. CONCLUSIONS

The directed transport of paramagnetic colloidal particles placed above a magnetic garnet film requires a symmetry breaking mechanism. Such symmetry breaking mechanism can be achieved by applying a modulated tilted external magnetic field or by an intrinsic symmetry breaking wedge pattern in the film. When both symmetry breaking mechanisms are applied simultaneously, complex transport behavior results that does not necessarily reflect the transport behavior of the particles when each mechanism is used individually. Theoretically deduced phase diagrams correspond well with the experimentally determined phase diagrams. Our findings might be useful for the transport of biomedical cargo with paramagnetic particles on a lab-on-a-chip device.

AUTHOR INFORMATION

Corresponding Author

*E-mail: thomas.fischer@uni-bayreuth.de.

ACKNOWLEDGMENT

This work has been supported by the German Science Foundation within the Center of Excellence SFB 840 and the Norwegian Research Council.

REFERENCES

(1) Dialynas, T. E.; Lindenberg, K.; Tsironis, G. P. *Phys. Rev. E* **1997**, *56*, 3976.
(2) Mateos, J. L. *Phys. Rev. Lett.* **2000**, *84*, 258.
(3) Lehmann, J.; Reimann, P.; Hänggi, P. *Phys. Rev. Lett.* **2000**, *84*, 1639.
(4) Reimann, P.; Hänggi, P. *Appl. Phys. A: Mater. Sci. Process.* **2002**, *75*, 169.
(5) Hastings, M. B.; Reichhardt, C. J. O.; Reichhardt, C. *Phys. Rev. Lett.* **2003**, *90*, 247004.
(6) Tierno, P.; Sagues, F.; Johansen, T. H.; Fischer, T. M. *Phys. Chem. Chem. Phys.* **2009**, *11*, 9615.
(7) Tierno, P.; Reddy, V. S.; Roper, M. G.; Johansen, T. H.; Fischer, T. M. *Phys. Rev. E* **2007**, *75*, 041404.
(8) Tierno, P.; Reddy, V. S.; Johansen, T. H.; Fischer, T. M. *J. Phys. Chem. B* **2008**, *112*, 3833.
(9) Dhar, P.; Tierno, P.; Johansen, T. H.; Fischer, T. M. *J. Phys. Chem. B* **2007**, *111*, 13097.
(10) Morse, P. M.; Feshbach, H. *Methods of Theoretical Physics Part II*; McGraw Hill: New York, 1953.

Chapter 6

Collapse and yield pressure of solid Langmuir monolayers

S. Aliaskarisohi, Th. M. Fischer, and N. Wilke,

Submitted to J. Phys. Chem

Collapse and yield pressure of solid Langmuir monolayers

May 12, 2011

S. Aliaskarisohi, [1], Th. M. Fischer[1] and N.Wilke [2],

Abstract

In a previous work, Muruganathan and Fischer observed laser-induced local collapse of a methyl stearate monolayer. These experiments opened the possibility of studying the collapse mechanism in a highly controlled manner, since the laser intensity can be easily varied and collapse happens in a definite place (the laser focus). In this paper we extended the work presented by Muruganathan et al. describing all the conditions that should fulfill a monolayer in order to generate a local collapse with a local gradient in temperature. We first corroborated that the laser-induced collapse is a thermocapillary effect and afterwards determined which monolayer property is essential for observing this phenomena. We propose that the flow of material into the focus of the laser is observed after the yield stress of the monolayer is overcome. As higher the yield stress, higher the temperature gradient that is necessary for the monolayer to flow. In order to observe the flow of material inward the focus of the laser and thus, local collapse, the monolayer should present an abnormal negative derivative of surface pressure with temperature at constant surfactant density.

[1]Institut für Experimentalphysik, Universität Bayreuth, 95440 Bayreuth, Germany.

[2]Centro de Investigaciones en Química Biológica de Córdoba (CIQUIBIC-CONICET), Departamento de Química Biológica, Facultad de Ciencias Químicas, Universidad Nacional de Córdoba, Argentina, email: wilke@mail.fcq.unc.edu.ar

1 Introduction

Surfactant monolayers at the air-water interface have been extensively studied as an interesting 2-D system in apparent equilibrium states. These systems present different phase states depending on the temperature, lateral pressure, subphase composition and nature of the monolayer-forming molecule. The monolayer is stable up to a characteristic lateral pressure, called the "collapse pressure". At this point, the molecules are expelled from the interface forming 3-D supramolecular structures. The modes of collapse and the surface tension at which collapse occurs depend on the composition of the monolayer and the subphase and on the temperature[1–4], which determine the morphology and material properties of the monolayer. Depending on the monolayer material properties, collapse of a 2D monolayer may lead to the formation of different 3D aggregates in the subphase, e.g. bilayer folds, vesicles, tubes, micelles, etc. If these aggregates can readily re-spread at the interface upon decrease of the monolayer surface density, then the collapse is reversible; otherwise, it leads to irreversible loss of material from the interface. These monolayer phenomena have been studied extensively using experimental techniques[4–8] and theoretical models[2–4,9–13]. The pathway from a 2D monolayer to a certain 3D structure, however, remains unclear. It is also not clear which properties of the constituting lipid molecule determine the structure of the 3D aggregate and the reversibility of the monolayer collapse.

Muruganathan and Fischer[13] observed laser-induced local collapse of a methyl stearate monolayer. Based on the assumption of a liquid monolayer, they predicted that locally heating a Langmuir monolayer at a surface pressure close to collapse with a focused IR laser induces the local collapse of the monolayer if the collapse pressure of the monolayer decreases more steeply with temperature than the surface tension of the pure water-air interface ($\partial\pi_c/\partial T < \partial\sigma_w/\partial T$). These experiments opened the possibility of studying the collapse mechanism in a highly controlled manner, since the laser intensity can be easily controlled and collapse happens in the laser focus. However, not all forming-monolayer molecules with $\partial\pi_c/\partial T < \partial\sigma_w/\partial T$ show laser-induced local collapse. For instance, we found that no local collapse could be observed in the case of dipalmitoylphosphatidylcholine (DPPC), dioleoylphosphatidylcholine, octadecanol, myristic and pentadecanoic acid monolayers, among others. The present work is a revision of the model presented in reference 13, starting with a detailed study of the methyl stearate laser-induced collapse. The results of this study first demonstrate that the local collapse in insolvable monolayers is a thermocapillary effect and then determined which monolayer property is essential for observing this phenomenon. In contrast to the

assumption of Muruganathan and Fischer, we assumed the monolayer to behave as a solid. Then, the flow of material into the focus of the laser is observed only after the yield stress of the monolayer is overcome. We found that the monolayers that show local collapse also present an abnormal negative derivative of the surface pressure with temperature at constant surfactant density. The threshold temperature gradient for which local collapse is observed in each monolayer is related to their yield pressure.

2 Experimental Methods

2.1 Materials.

The lipids were purchased from Avanti Polar Lipids (Alabaster, AL). All the other surfactants were from Sigma Aldrich. Surfactant solutions were fluorescently labeled with 1 mole of 1,2-dihexadecanoylsn- glycero- 3- phosphoethanolamine, triethylammonium salt (Texas Red DHPE) purchased from Molecular Probes (Eugene, Oregon USA). The surfactants were dissolved in chloroform (about 1 mM) and spread at the air-water interface. The subphase was pure water (Millipore Milli-Q 18 $M\Omega$ cm) or solutions of $CuSO_4.5H_2O$ (Merck).

2.2 Methods.

A Nima and a KSV film balance was used for monolayer investigation. The setup for studying collapse phenomena has been described in detail elsewhere[14]. Briefly, it consists of a home-built Langmuir trough placed on the stage of an inverted fluorescence microscope (Zeiss-Axiovert 135) with a 100 water immersive objective. The temperature of the trough can be controlled precisely. An IR laser beam (λ=1064 nm, P=2mW-2.7W) was used to locally heat the monolayer in the focus of the objective. The light is partially absorbed by the subphase and heats the monolayer locally around the focus.

3 Results

In the previous work[13], it was observed that upon focusing an IR laser on a methyl stearate monolayer in the liquid condensed phase, at a laser power higher than a critical value of about 2W, a radial flow of the surface toward the center sets in, see

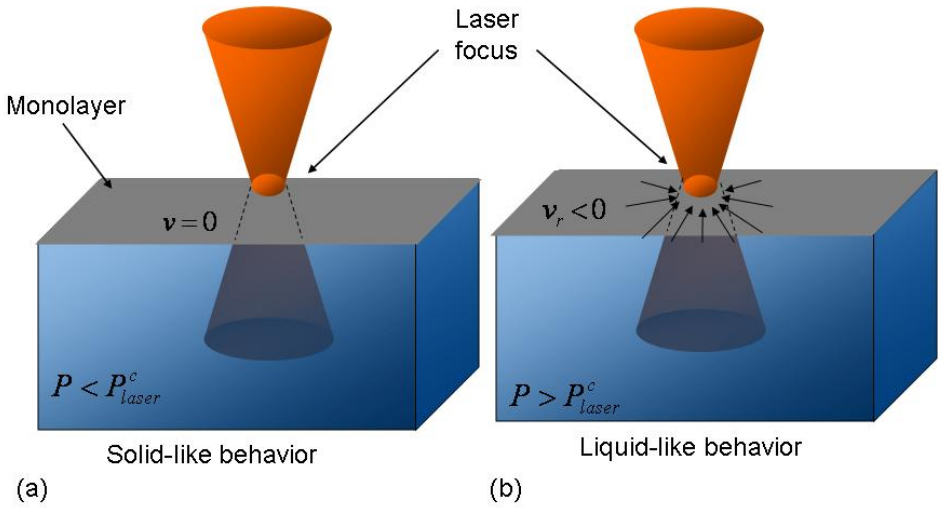

Figure 1: scheme of a monolayer locally heated by a laser. (a)$P < P^c_{laser}$, (b) $P > P^c_{laser}$. v is the flow velocity of monolayer. A movie of the inward flow above $P > P^c_{laser}$ is shown in the Supporting information.

the scheme in figure 1. Muruganthan and Fischer measured the flow quantitatively by following the characteristic texture of the monolayer as a function of time. Surfactant material aggregates into a three-dimensional structure in the hot spot that grows in radius due to a radial inward flow of the monolayer surrounding the aggregate.

The present work first focused on determining the driving force of the laser-induced local collapse. To assure that the phenomena is driven by local heating and not by an optical effect, we performed experiments on subphases that contain $CuSO_4$ at different concentrations. The aqueous complex of Cu (II) absorbs light at 1064 nm according to the Lambert and Beer law, and thus, the subphase absorbance at the laser wavelength of 1064 nm linearly increases with the $CuSO_4$ concentration. Therefore, the absorbed power of the laser beam (P_{Abs}) for a fixed

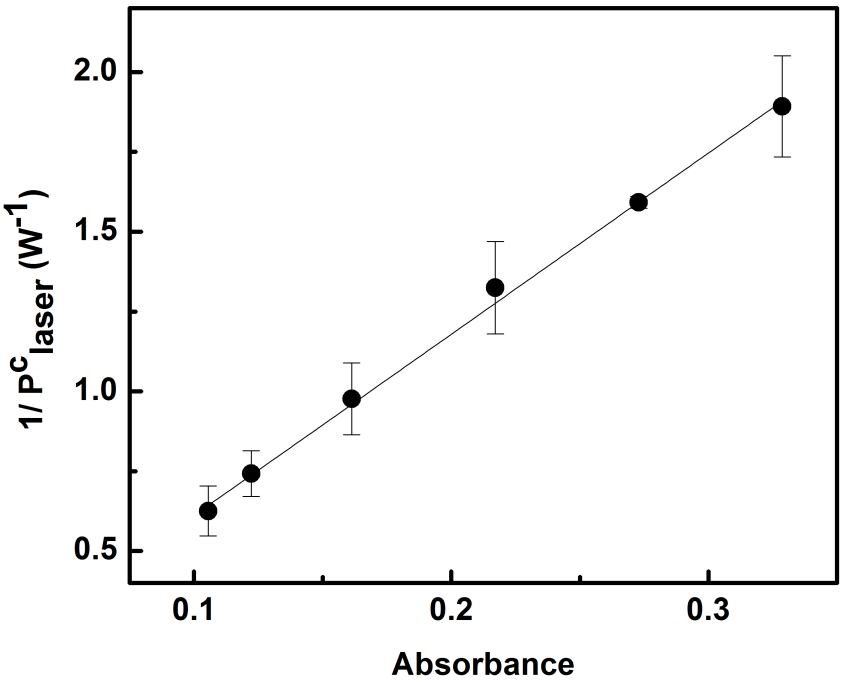

Figure 2: Reciprocal of the critical laser power as a function of the absorbance of the subphase at 1064 nm.

laser power (P_{laser}) will increase linearly with the concentration in the subphase according to the following relation: $P_{Abs} = P_{laser} Abs\ r_w$, where r_w is the focal width of the laser which is about $1\mu m$ and Abs is the absorbance of the subphase at 1064 nm. We determined the minimum laser power that is necessary for observing the flow of molecules into the laser focus (P^c_{laser}). These experiments were performed with methyl stearate monolayers at 20°C and at a surface pressure near the collapse surface pressure using subphases with increasing $CuSO_4$ concentrations. The isotherms of methyl stearate on the $CuSO_4$ solutions are indistinguishable from the isotherm on pure water (data not shown).

Figure 2 displays the critical laser power as a function of the absorbance of the subphase at 1064 nm. The inverse of P^c_{laser} increases directly proportional with the absorbance as it is expected if the process is purely driven by a local heating,

since this means that the flow starts at a fixed absorbed power regardless of the subphase composition.Therefore the critical stress needed to yield the monolayer is a function of the temperature gradient only. In a liquid, a local temperature gradient will generate flow to keep the surface tension constant ($\nabla\sigma \approx \nabla\pi = 0$). On the contrary, for a material in the solid state the density remains roughly constant $\nabla\rho = 0$ upon heating, and a local gradient of temperature will produce a pressure gradient that is proportional to $\nabla\pi = \partial\pi/\partial T)_{\varrho}\nabla T$.We therefore are interested in the change of pressure along an isochore i.e. the pyrobaric coefficient = $\partial\pi/\partial T)_{\varrho}$.

Figure 3a, b shows the pressure versus area compression isotherms for ethyl stearate and DPPC at various temperatures. In DPPC the pressure increases monotonically with increasing temperature at a constant area, like any normal material. For ethyl stearate two different regions exist, at large area *pbc* is positive and at low area it becomes negative. For each temperature we may define a cross over pressure π_{pbc} where the behavior changes from a normal ($pbc > 0$) to an abnormal behavior ($pbc < 0$). The phase diagram in figure 4 displays this abnormal region which lies between collapse pressure and the cross over pressure (filled region). We analyzed the effect of local heating monolayers composed of different molecules and found that, wherever the value of *pbc* is negative at pressures lower than the collapse pressure, local collapse is observed. On the contrary, for $pbc > 0$ this phenomena is not induced by the laser beam. This is summerized in table 1.

4 Discussion.

Based on the assumption that the monolayer behaves as a liquid, Muruganathan and Fischer in their work[13] claimed that only one condition is required for local collapse . They showed that if the collapse pressure decreases with increasing temperature with a slope smaller than the change of the surface tension of the bare air/water interface with temperature ($d\pi_c/dT < d\sigma_w/dT$) then local heating by a laser beam will lead the molecules at the monolayer to acquire a three-dimensional structure.

However, this will not be the case for monolayers that behave as a solid, since they will not flow easily. In order to confirm this idea, we analyzed the effect of locally heating of monolayers prepared with different surfactants; the results are summarized in table 1. As an example, we found that monolayers of DPPC do not show a flow of material inside the laser focus for any laser power either on water or $CuSO_4$ solutions. On the contrary, ethyl stearate shows collapse when it is submitted to a local heating.

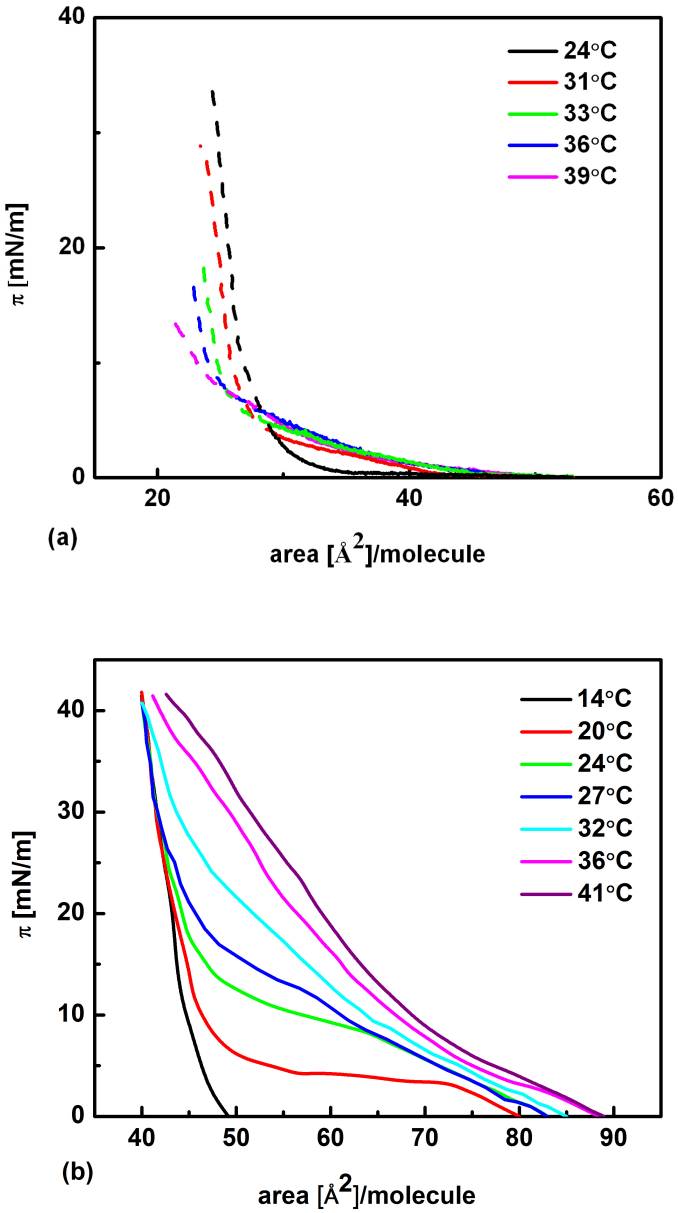

Figure 3: Surface pressure versus average molecular area compression isotherms for (a) ethyl stearate, (b) DPPC for the indicated temperatures at the air/water interface. In (a) the isotherms are shown as dashed lines in the regions where $pbc < 0$. For DPPC $pbc > 0$ everywhere.

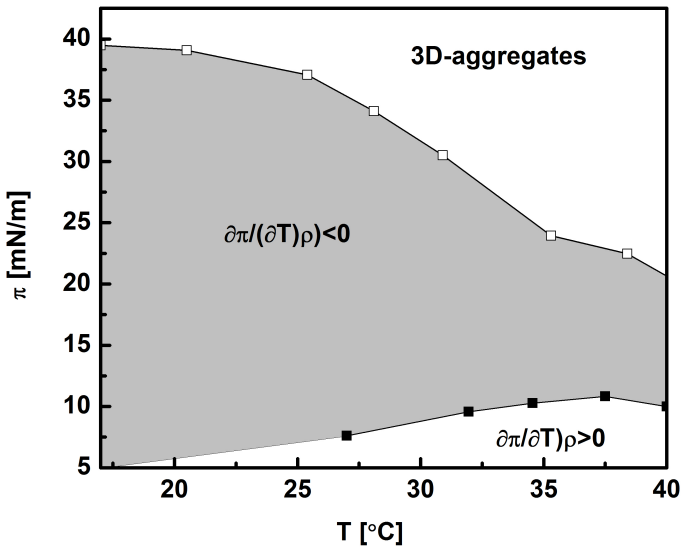

Figure 4: Collapse pressure diagram for ethyl stearate. The gray region indicates the abnormal region in which $\partial\pi/\partial T)_{\varrho} < 0$. □: the collapse pressure, π_c and ■: the cross over pressure, π_{pbc}.

The force density (i.e. the tension gradient) is directed toward the focus or away from it if the tension in the focus is higher or lower than in the cold region, respectively. The former situation supports collapse of the monolayer, while the latter prevents it. The monolayer will hold until a critical pressure gradient is reached in which it will yield and will start to flow. Yielding of the solid monolayer does not depend on the direction of the stress gradient although the monolayer will yield to collapse only in one direction. This will happen when $\nabla\sigma = -\nabla\pi = -\partial\pi/\partial T)_{\varrho}\nabla T$ is directed toward the focus. Since the monolayer is considered to be solid before yielding, the density can be approximated as constant. In that situation, the pressure inside the focus is:

$\pi_{focus} = \pi_{\infty} + \int_{r_{\infty}}^{r_w} dr\partial\pi/\partial T)_{\varrho_s}\nabla T$, where π_{focus} and π_{∞} are the surface pressure at the laser focus and far away from it, respectively. We assume $\partial\pi/\partial T)_{\varrho}$ to be roughly constant. At collapse, π_{∞} is the collapse pressure, π_c, and thus: $\pi_{focus} \approx \pi_c + \partial\pi/\partial T)_{\varrho} \triangle T$

$\partial\pi/\partial T)_{\varrho}\Delta T$ is the excess pressure that pushes the monolayer from outside the laser focus into it or the opposite way. $\partial\pi/\partial T)_{\varrho}\Delta T_{critical}$ is the maximum pressure that the solid can withstand without flowing, and therefore we will define the yield pressure as $\pi_{yield} = -\partial\pi/\partial T)_{\varrho}\Delta T_{critical}$

In table 1 we show the sign of $\partial\pi/\partial T)_{\varrho}$ for each material that we analyzed. As expected, only the monolayers with $\partial\pi/\partial T)_{\varrho} < 0$ ($\pi_{yield} > 0$) show inward flow of material to the laser focus. We quantified π_{yield} for these monolayers at 26 °C and at a surface pressure near the collapse point of each of them. The temperature gradient in the illuminated region of the monolayer can be calculated according to $\Delta T = T(r) - T_{\infty} = \alpha P_{laser} r_w / 2\pi\kappa r$.[15]

Here T_{∞} is the temperature far away from the hot spot, $\alpha = 0.1 cm^{-1}$ is the adsorption coefficient of water at the wavelength of the IR laser, $\kappa = 0.6 W/mK$ is the heat conductivity of water. The slope $\partial\pi/\partial T)_{\varrho}$ is approximated as $(\pi(T_1) - \pi(T_2))/(T_1 - T_2)$ and it is computed from the isotherms at different temperatures (T_1 near T_{∞} and T_2 near $T(r)$). Figure 5 shows the yield pressure and the critical laser power for monolayers of ethyl stearate , methyl stearate and hexadecanol at 26 °C and a surface pressure near the collapse of each monolayer.

Table 1. List of the analyzed monolayer-forming molecules with the corresponding sign of the slope of surface pressure with temperature at constant surfactant density, the table also summarizes the effect of the IR laser beam

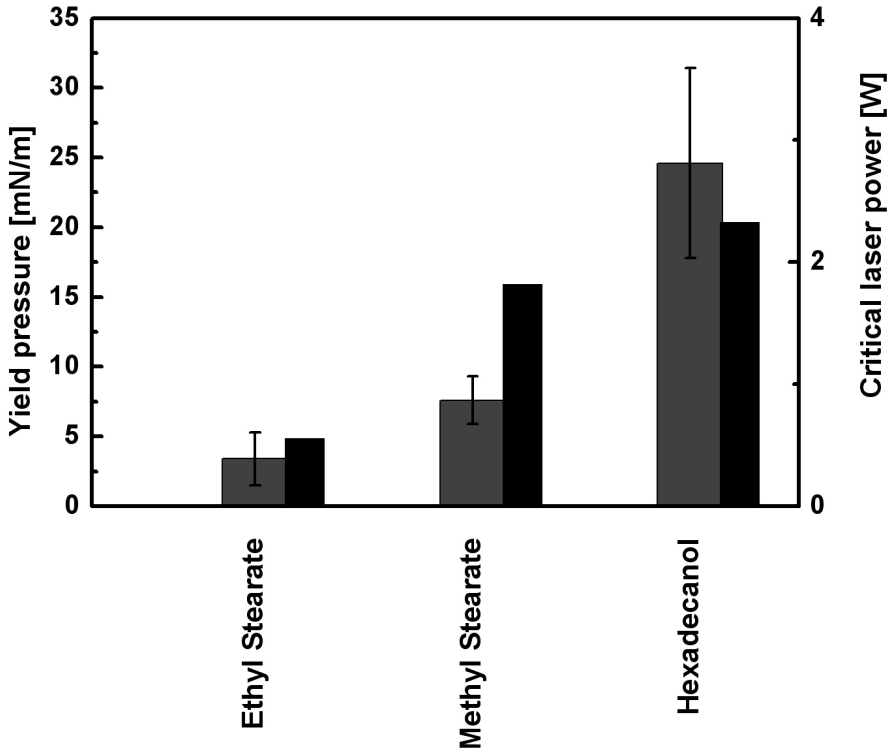

Figure 5: Yield pressure and critical laser power for ethyl stearate, methyl stearate and hexadecanol monolayers at 26 °C on water subphases. Gray bars are the yield pressure and correspond to the left scale while black bars are the critical power and correspond to the right scale.

Surfactant	Laser-induced local collapse	Sign of $d\pi/dT)_{\varrho}$
methyl stearate	Yes	Negative
methyl arachidate acid	No	Positive
ethyl stearate	Yes	Negative
hexadecanol	Yes	Negative
octadecanol	No	Positive
dimiristoylphosphatidylcholine	No	Positive
distearoylphosphatidylcholine	No	Positive
dipalmitoylphosphatidylcholine	No	Positive
dioleoylphosphocholine	No	Positive
dioleoylphosphatidylglycerol	No	Positive
myristic acid	No	Positive
pentadecanoic acid	No	Positive

5 Conclusions

In this paper we extended the work presented by Muruganathan and Fischer[13] describing all the conditions that should fulfill a monolayer in order to generate a local collapse with a local gradient in temperature. From all the systems that we analyzed, only three of them show heat-induced local collapse (see table 1). Through the observation of the thermal behavior of the compression isotherms, we found that these three monolayers present an abnormal behavior in the temperature and surface pressure range in which the local collapse is induced. In these monolayers, the surface pressure decreases as the temperature increases at constant surfactant density. Since we considered the monolayer as a solid, it is necessary to reach a critical surface pressure in order to yield the material and observe the flow of it. At these conditions, the flow is inward the focus of the laser only if the pyrobaric coefficient ($pbc = d\pi/dT)_{\varrho}$) is negative. Therefore, this condition is necessary to produce a local collapse through a local temperature gradient. The threshold temperature gradient necessary for the material flow increases as the yield stress of the monolayer increases.

6 Acknowledgments

N. W. wants to thank the support from Sistema Nacional de Microscopia (SNM), SECyT-UNC and FONCYT (Program BID 1728/OC-AR PICT 0770), Argentina. N.W. is a Career Investigators of CONICET. SA and TMF are supported by the German Science Foundation through grant FI-548-11-1.

7 Supporting Information Available

Movie of the inward flow of material for a monolayer of ethyl stearate at 26 C and 25 mN/m. The real time and the real size for this movie are 14 s (30 frame/s) and $48\times36\mu m^2$, respectively.

References

[1] Gopal, A.; Belyi, VA.; Diamant, H.; Witten, TA.; Lee, KYC. *J. phys. Chem. B* **2006**, *110*, 10220.

[2] Lee, KYC.; *Annu. Rev. Phys. Chem.* **2008**, *59*, 771.

[3] Ybert, C.; Lu, W.; Moller, G.; Knobler, CM. *J. Phys. Chem. B.* **2002** , *106*, 2004.

[4] Ries, HE.; *Nature.* **1979**, *281*, 287.

[5] Gopal, A.; Lee, KYC. *J. Phys. Chem. B.* **2001**, *105*, 10348.

[6] Lipp, MM.; Lee, KYC.; Takamoto, DY.; Zasadzinski, JA.; Waring, A *J. Phys. Rev. Lett.* **1998**, *81*, 1650.

[7] Schief, WR.; Hall, SB.; Vogel, V. *Phys. Rev. E.* **2000**, *62*, 6831.

[8] Hatta, E. *Langmuir* **2004**, *20*, 4059.

[9] Rugonyi, S.; Smith, EC and Hall, SB. *Langmuir* **2004**, *20*, 10100.

[10] Saccani, J.; Castano, S.; beaurain, F.; Laguerre, M.; Desbat, B. *Langmuir* **2004**, *20*, 9190.

[11] Diamant, H.; Witten, TA.; Ege, C.;Gopal, A.; Lee, KYC. *Phys. Rev. E.* **2002**, *63* , 061602.

[12] Lu, WX.; Knobler, CM.; Bruinsma, RF.; Twardos, M.; Dennin, M. *Phys. Rev. Lett.* **2002**, *89*, 146107.

[13] Muruganathan, RM.; Fischer, Th. M. *J. Phys. Chem. B*. **2006**, *110*, 22160.

[14] Wurlitzer, S.; Lautz, C.; Liley, M.; Duschl, C.; Fischer, Th. M. *J. Phys. Chem. B*. **2001**, *105*, 182.

[15] Khattari,Z and Fischer T.M. *J. Phys. Chem. B* **2004**, *108*, 13696.

Table of content

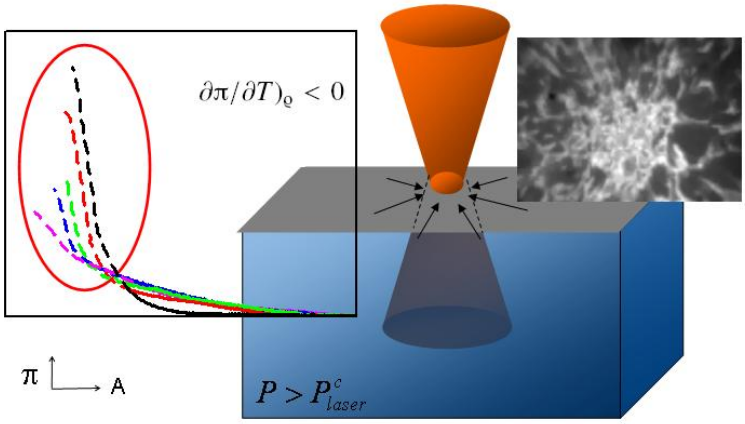

Chapter 7

Summary

In chapter 3 we introduced single-domain rheology and two-domain rheology on a vesicle as two effective methods for measuring the surface shear viscosity of a membrane in a vesicle. We derived the theoretical equations to evaluate the data and performed experiments on domains in vesicles of ternary mixtures of DPPC, DOPC and Cholesterol. The viscous length scale which is the ratio between surface shear viscosity and bulk viscosity determines whether the surface shear viscosity of a vesicle can be measured or not. We showed that the surface viscosity is measurable only if this length scale falls between the domain size, and the vesicle size. To measure the surface shear viscosity through the diffusive motion of the domains, high resolution and high sensitivity to the shear viscosity is needed. We demonstrated that in one-domain rheology, the domain's motion can be always resolved but at high surface viscosity the solid rotational diffusion of the vesicle dominates the motion, leading to a reduced sensitivity to the surface shear viscosity. Two- domain rheology measures the relative diffusion of domains and eliminates the solid rotation experimentally. Therefore it is more sensitive to the surface shear viscosity. At high surface shear viscosity the hydrodynamic interactions between domains become stronger. This slows down the relative motion such that it cannot be resolved before both domains leave the focus of the microscope. We have shown that one-domain rheology is the superior technique to measure the surface shear viscosity as compared to two- or multi domain rheology. Using one-domain rheology in a ternary mixture of DOPC, DPPC and Cholesterol we showed that contrary to what was stated in the literature [19] dissipation is dominated by water because the viscous length scale was smaller than the domain size. In the literature the slow relative motion was misinterpreted as a slow individual diffusion of a domain. In reality it is a collective slowing down due to hydrodynamic interactions.

In chapter 4 nonmagnetic and paramagnetic colloids in a ferrofluid were self assembled into magnetic colloidal flowers. The dynamic fluctuations of the non magnetic colloidal petals of the flower are investigated. The superposition of dipolar interactions and random forces arising from the thermal fluctuations of the embedding fluid cause the colloidal nonmagnetic petals to fluctuate in numbers and conformation.

We have measured correlation functions of the petal number as well as of the angular velocities of the individual petals. Diffusions of colloidal petals are different from *single-file diffusion* because there is only a weak anticorrelated time delayed correlation observed in the motion of the particles. The correlations cen-

ter around zero time delay and at no time petals diffuse individually. We have determined the diffusion constants of normal modes that are waves circulating around the paramagnetic core. Diffusion constants monotonically decrease with the wave number m. The absorption and desorption of petals are controlled by a saddle point in the energy landscape and can thus be understood as an activated process.

In chapter 5 we induced the transport of paramagnetic colloidal particles placed above a magnetic garnet film with a wedge shaped periodic stripe pattern using a tilted external time dependent magnetic field. The direction of transport depends on several symmetry breaking elements: the wedge angle, the tilt angle of the external magnetic field, and the angle between the lateral components of the external field with the bisector of the wedge. Both the external field tilt and the wedge pattern are able to direct the particles in the absence of the other symmetry breaking effect. If both symmetry breaking effects are applied with weak strengths, one of them wins depending on who is stronger. However, if both are strong, the resulting transport direction can be opposite to the direction supported by the individual effects even when the individual effects are directing the transport into the same direction. This underlines the nonlinear behavior of this form of transport. The theoretical phase diagrams are in a good agreement with our experimental results.

In chapter 6 the thermocapillary induced yielding prior to collapse of a variety of chemically different monolayers were studied. Among all materials we analyzed only three of them show laser induced yielding. We determined yielding pressure of the order of $5-25\times10^{-3}\ Nm^{-1}$ for fatty acid esters and some long chain alcoholes. Another subset of surfactants, like lipids, and short chain alcohols do not yield in the laser. We found that a prerequisite for yielding seems to be that the surface pressure at constant density decreases whith increasing temperature. Such abnormal temperature dependence was found in all monolayers that yield and in none of the non yielding materials. The necessity of this abnormal behavior can be understood considering that for yielding and collapse an inward flow toward the laser focus is needed.

In sumnmary a variety of subtle effects in the active and passive transport close to interfaces have been solved with this thesis that might help the further analysis of interfacial transport processes in the future.

Chapter 8

Bibliography

[1] Feng,J., Wong, K.Y., Dyer, K. and Pettitt, B.M., Transport properties of water at functionalized molecular interfaces. *J. Chem. Phys.* 131, 125102 **2009**.

[2] Kastin,A.J., Akerstrom,V. and Pan, W. Activation of urocortin transport into brain by leptin. *Peptides*, 21, 1811-1817, **2000**.

[3] Cukier, R.I., Nocera, D.G., Proton-coupled electron transfer *Annu. Rev. Phys. Chem.* 49, 337-69, **1998.**

[4] Sharma V., Jaishankar, A., Wang, Y.C., McKinley, G.H. , Rheology of globular proteins: apparent yield stress, high shear rate viscosity and interfacial viscoelasticity of bovine serum albumin solutions. *Soft matter*, 7, 5150-5160, **2011**.

[5] Shah, A.B., Jonesand, G.P., and Vasiljevic, T. Sucrose-free chocolate sweetened with Stevia rebaudiana extract and containing different bulking agents effects on physicochemical and sensory properties. *International Journal of Food Science and Technology*, 45, 1426-1435, **2010**.

[6] Dawe, R.A., Enhanced oil recovery. *J.Chem. Tech. Biotechnol*, 51, 361-393, **1991**.

[7] Huang, J. S., and Varadaraj, R. Colloid and interface science in the oil industry *Current Opinion in Colloid and Interface Science* , 1, 535-539, **1996**.

[8] Reimann, P., Brownian motors: noisy transport far from equilibrium. *Phys. Rep.* 361, 57265, **2002**.

[9] Tierno,P. Reddy, S. V., Roper, m.G., Johansen, T. H. and Fischer, T. M., Transport and Separation of Biomolecular Cargo on Paramagnetic Colloidal Particles in a Magnetic Ratchet *J. Phys. Chem. B*, 112, 3833-3837, **2008**.

[10] Lehmann, J.; Reimann, P.; Hänggi, P. *Phys. Rev. Lett.* ,84, 1639, **2000**.

[11] Hastings, M. B.; Reichhardt, C. J. O.; Reichhardt, C. *Phys. Rev.Lett.* 90, 247004, **2003**.

[12] Hahn,K., Karger,J. and V. Kukla, Single-File Diffusion Observation. *Phys. Rev. Lett.*, 76, 2762, **1996**.

[13] Kukla V., Kornatowski J., Demuth D., Gimus I., Pfeifer H., Rees LV.C, Schunk S., Unger KK., Karger J., NMR studies of single-file diffusion in unidimensional channel zeolites. *Science*, 272, 702-704, **1996**.

[14] Ryabov, A. and Chvosta, P., Single-file diffusion of externally driven particles. *Phys. Rev. E*, 83, 020106-1, **2011**.

[15] Herrera-Velarde, S., Zamudio-Ojeda, A. and Castaeda-Priego, R., Ordering and single-file diffusion in colloidal systems. *J.Chem.Phys*, 133, 114902, **2010**.

[16] Chen, Q. Moore, J. D. Liu,Y.C. Roussel,T.J, Wang, Q. Wu, T. and Gubbins, K. E. Transition from single-file to Fickian diffusion for binary mixtures in single-walled carbon nanotubes. *J. Chem. Phys*, 133, 094501, **2010**.

[17] Wei,Q.H, Bechinger,C., Leiderer, P. Single-File Diffusion of Colloids in One-Dimensional Channels. *Science*, 287, 625, **2000**.

[18] Lutz,C.,Kollmann, M. and Bechinger,C. Single-file diffusion of colloids in one-dimensional channels. *Phys. Rev. Lett.* 93, 026001, **2004**.

[19] Cicuta P., Keller S.L., and Veatch S.L. Diffusion of liquid domains in lipid bilayer membranes. *J. Phys. Chem. B* 111, 3328-3331, **2007**.

[20] Saffman, P.G.,and Delbrück, M. Brownian motion in biological membranes. *Proc. Nat. Acad. Sci. (USA)* 72, 3111-3113, **1975**.

[21] George, L. Gaines, JR. *John Wiley and Sons, Inc.*, **1966**.